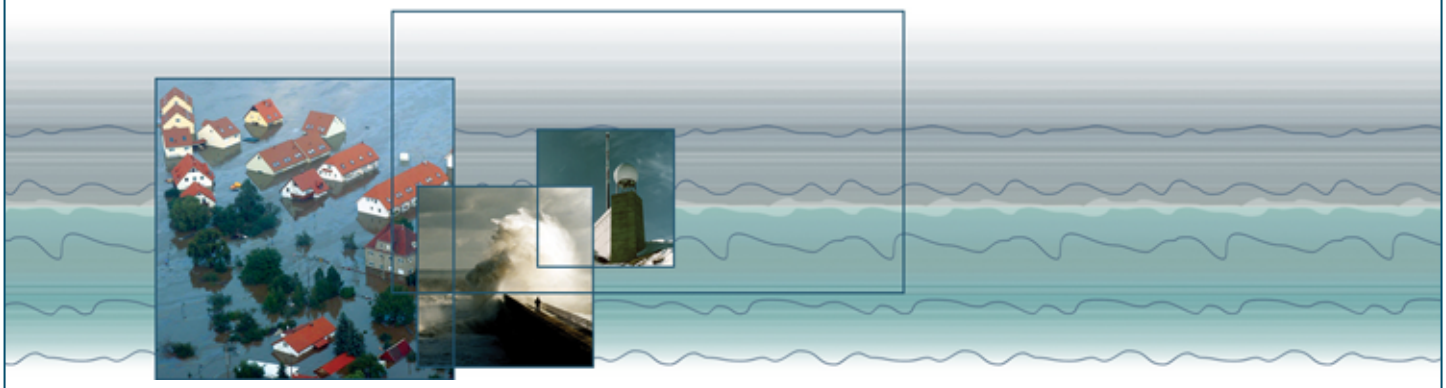
Integrated Flood Risk Analysis
and Management Methodologies

FLOODsite



Observation of storm rainfall for flash-flood forecasting Volume 1

RADAR STRUCTURED ALGORITHM SYSTEM (SAS)

Date	February 2008
Report Number	T15-08-02
Revision Number	1_1_P01
Deliverable Number:	D15.2
Due date for deliverable:	02 08
Actual submission date:	02 08
Task Leader	INPG

FLOODsite is co-funded by the European Community
Sixth Framework Programme for European Research and Technological Development (2002-2006)
FLOODsite is an Integrated Project in the Global Change and Eco-systems Sub-Priority
Start date March 2004, duration 5 Years

Document Dissemination Level

PU	Public	PU
PP	Restricted to other programme participants (including the Commission Services)	
RE	Restricted to a group specified by the consortium (including the Commission Services)	
CO	Confidential, only for members of the consortium (including the Commission Services)	

Co-ordinator: HR Wallingford, UK
Project Contract No: GOCE-CT-2004-505420
Project website: www.floodsite.net

SIXTH FRAMEWORK PROGRAMME

DOCUMENT INFORMATION

Title	**Radar observation of storm rainfall for flash-flood forecasting – Radar structured algorithm system**
Lead Author	**Guy Delrieu**
Contributors	**Alexis Berne, Brice Boudevillain, Marco Borga, Benoît Chapon, Pierre-Emmanuel Kirstetter, John Nicol, Daniele Norbiato, Remko Uijlenhoet**
Distribution	**Public**
Document Reference	**T15-08-02**

DOCUMENT HISTORY

Date	Revision	Prepared by	Organisation	Approved by	Notes
22/02/2008	1_0_P08	G. Delrieu	INPG		
07/04/08	1_1_P01	Paul Samuels	HR Wallingford		Final Formatting, listed as Volume 1, new file name

ACKNOWLEDGEMENT

The work described in this publication was supported by the European Community's Sixth Framework Programme through the grant to the budget of the Integrated Project FLOODsite, Contract GOCE-CT-2004-505420.

DISCLAIMER

This document reflects only the authors' views and not those of the European Community. This work may rely on data from sources external to the FLOODsite project Consortium. Members of the Consortium do not accept liability for loss or damage suffered by any third party as a result of errors or inaccuracies in such data. The information in this document is provided "as is" and no guarantee or warranty is given that the information is fit for any particular purpose. The user thereof uses the information at its sole risk and neither the European Community nor any member of the FLOODsite Consortium is liable for any use that may be made of the information.

© FLOOD*site* **Consortium**

SUMMARY

A radar structured algorithm system (radar SAS) has been set up and assessed by the FLOODsite Task 15 partners. This system is aimed at improving quantitative precipitation estimation of storm rainfall for flash-flood forecasting in mountainous regions.

A number of innovative quantitative pprecipitation estimation (QPE) algorithms aimed at a space-time adaptive radar data processing are developed by LTHE/INPG using the datasets of the Bollène 2002 Experiment. Firstly, a ground clutter identification technique based on the pulse-to-pulse variability of the reflectivity is described and implemented to cope with the severe clutter experienced at S-band in such environment. Secondly, two rain-typing algorithms already proposed in the literature are adapted and coupled with the identification of the vertical profiles of reflectivity (VPR) for convective and stratiform precipitation. Two VPR estimation approaches are adapted to the case of time-varying geographical support: (1) a simple averaging of measured reflectivities close to the radar site and (2) an inversion technique aimed at filtering radar beam sampling effects. Finally, various methods are considered for combining the corrected reflectivity measurements at the various elevation angles for estimating reflectivity at ground level prior to application of rain-typed Z-R relationships. Illustrations of the algorithms behaviour are given with the observations available for two selected time steps. In addition, a stochastic model is proposed by WUR to analyze the influence of the spatial variability of the raindrop size distribution (DSD) on rainfall estimation using weather radar. This model allows simulating range profiles of DSDs and consequently profiles of rainfall intensity, radar reflectivity and specific attenuation. A first application concerning the accuracy of attenuation correction algorithms is presented.

The radar SAS assessment is realized with two complementary approaches in the French and Italian Pilot Sites.

French case study

The radar and raingauge datasets collected during the Bollène-2002 Experiment for a series of intense Mediterranean precipitation events are used for this assessment. Reference rainfall data is derived from a careful geostatistical analysis of the raingauge data. The new ground clutter identification and correction algorithm proves to work satisfactorily. Various time and space-time adaptive strategies are defined and implemented with focus on assessing a convective-stratiform precipitation separation method coupled with the vertical profile of reflectivity inference. The results indicate that good radar quantitative rainfall estimation is feasible within the 100-km radar range in mountainous regions by using well-sited, well-maintained radar systems and sophisticated physically-based radar data processing systems. Determining the radar detection domain, performing an efficient ground clutter processing, “capturing” the vertical structure(s) of reflectivity for the event of interest are the basic ingredients required. The radar performance depends on the rain types with very significant variations here between mesoscale convective systems, frontal and shallow convective events. The Bollène 2002 results indicate that the added value of the space-time adaptive processing is moderate. To be more specific, the radar raingauge scatter quantified by the determination coefficient remains basically unchanged for all the time and space-time adaptive processing strategies considered. A positive trend is observed however in terms of bias since the most refined space-time adaptive strategy presents systematically the lowest mean relative errors. This is attributed to a better estimation of the reflectivity at ground level by means of the typed VPRs. Adapting the separation method for radar network operation and documenting the Z-R relationships conditional on rain types for Mediterranean intense rainfall are the two perspectives of this work.

Italian case study

The parameter values of the radar SAS are often based on limited experimental studies and, more recently, on the implementation of calibration procedures aimed at identifying the optimal parameter set. The work performed by UniPad suggests, however, that there may be many parameter sets within an algorithm structure that are equally acceptable for rainfall estimation at the ground, and that these may come from very different regions in the parameter space. A methodology is proposed to take into account and assess the uncertainty arising from errors in parameter selection. The methodology, which is based on the GLUE (Generalised Likelihood Uncertainty Estimation), reformulates the algorithm calibration problem into the estimation of posterior probabilities of algorithm responses, thereby avoiding the idea that there is an optimum parameter set. The results of the preliminary studies are presented. Through an illustrative case study it is shown that the uncertainty assessment approach is not only practical and relatively simple to implement but can also provide useful information about the strength and limitations of the radar SAS.

CONTENTS

Document Information
Document History
Acknowledgement
Disclaimer
Summary iii
Contents v

Integrated Flood Risk Analysis 1
and Management Methodologies 1
Radar observation of storm rainfall for flash-flood forecasting 1
Volume 1 RADAr structured algorithm system (sas) 1
Date February 2008 1
Report Number 1
T15-08-02 1

1. Introduction 5

2. The radar SAS: innovative algorithms 6
2.1 The Bollène-2002 experiment 6
2.2 Adaptive clutter identification and correction 12
2.3 Rain-type separation 16
2.3.1 Review of two existing algorithms 16
2.3.2 Implementation of the two algorithms 17
2.4 VPR identification conditional on rain types 18
2.4.1 Definition of the vertical profile of reflectivity 18
2.4.2 Probability density functions of the measured reflectivity as function of the altitude 19
2.4.3 Apparent VPR 21
2.4.4 Inverse VPR 23
2.5 Coupled rain separation and VPR identification 25
2.5.1 Preliminary rain typing 25
2.5.2 VPR identification conditional on rain types 25
2.5.3 Refined rain typing 26
2.6 2-D rain product establishment from the 3D reflectivity data 26
2.7 A stochastic model of range profiles of raindrop size distribution: application to the sensitivity analysis of attenuation correction schemes to the DSD variability 27
2.7.1 DSD profile simulator 28
2.7.2 Attenuation correction algorithms 30
2.8 Conclusions 34

3. Implementation and evaluation of the radar SAS in the various pilot sites 35
3.1 Cévennes-Vivarais Pilot Site 35
3.1.1 Introduction 35
3.1.2 Reference rainfall 38
3.1.3 Radar data processing strategies 43
3.1.4 Assessment of various radar processing strategies 48
3.1.5 Conclusions 54
3.2 Adige Pilot Site 55
3.2.1 Introduction 55
3.2.2 Study area and data resources 56
3.2.3 Error sources and the radar rainfall estimation algorithm 57
3.2.4 The Generalized Likelihood Uncertainty Estimation (GLUE) methodology 64

3.2.5 Conclusion 70

4. References 72

Tables

TABLE 2.1. Parameters of the Bollène radar system 8
TABLE 2.2. Volume scanning protocol implemented for the Bollène radar system. 8
TABLE 2.3: Parameterization of the ground clutter identification technique. 14
TABLE 2.4: Detailed results of the Steiner's algorithm for the case of 0200 UTC 9 September 2002 18
TABLE 2.5 Mean and standard deviation of N_t, D_m, $N' = \ln N_t$ and $D' = \ln D_m$. 30
TABLE 3.2: Parameters of the spherical models fitted on the experimental variograms at the event and hourly timescales. 42
TABLE 3.3: Mean value of the reference ground clutter target used to test radar calibration stability. 45
TABLE 3.4 Monte Grande weather radar characteristics. 57
TABLE 3.5 Description of the selected events. 58
TABLE 3.6: Algorithm parameters 62
TABLE 3.7: Optimised parameters for the six events 64
TABLE 3.8: Statistical analysis of rainfall estimation by using unadjusted and adjusted radar observations 64
TABLE 3.9. Parameter value ranges used for GLUE sampling. 66
TABLE 3.10: Results of the sensitivity analysis 69
TABLE 3.11: Results of the sensitivity analysis, including attenuation correction 70

Figures

Figure 2.1: Study area in Southeastern France with the localization of the four new S-Band weather radar systems (with 100 km range markers) deployed by Météo-France. 7
Figure 2.2: Case of the mesoscale convective system observed on 9 September 2002 at 0200 UTC.9
Figure 2.3: Vertical cuts in the volume radar data for the case of 9 September 2002 at 0200 UTC 10
Figure 2.4: Same as Fig. 2.2 for the cold front case of 21 October 2002 at 2030 UTC. 11
Figure 2.5: Same as Fig. 2.3 for the cold front case observed on 21 October 2002 at 2030 UTC. 12
Figure 2.6: Dry weather clutter characteristics for the 0.8° (left) and 3.6 ° (right) PPIs 15
Figure 2.7: Illustration of the 3D-variability of the measured reflectivity within the 60-km range for the 0200 UTC 9 September 2002 case. 20
Figure 2.8: Normalized reflectivity profiles for the 0200 UTC 9 September 2002 case. 22
Figure 2.9: Same as Fig. 2.8 for the 2030 UTC 21 October 2002 case. 23
Figure 2.10. Example of Z and Z_a profiles generated by the DSD model 30
Figure 2.11 Distribution of the RMSE values normalized by the mean value over the profiles. 31
Figure 2-12. RMSE between the exact Z profiles and the Z_c profiles. 32
Figure 2-13. Distribution of the RMSE values calculated between the exact Z profiles and the averaged Z profiles at the 25 m resolution. 33
Figure 3.1: Raingauge networks available in the French pilot site. 36
Figure 3.2: Illustration of the quality-control technique of rain gauge data at the event timestep. 40
Figure 3.3: Maps of the point estimation standard deviation (mm) of the reference rainfall 43
Figure 3.4: Screening factors of the Bollène radar estimated using a digital terrain model. 46
Figure 3.5: Identified VPRs for the 8-9 September 2002, 21 November 2002 and 10-13 December 2002 rainfall events. 47
Figure 3.6: Scattergraphs of the radar-raingauge comparison over the set of 5 rain events selected at the event and hourly time steps for the T-AD1 and ST-AD3 radar processing strategies.48
Figure 3.7: Evolution of the assessment criteria at the event time step as function of the radar processing strategy for the [0-100 km] radar range interval. 50
Figure 3.8: Evolution of the Nash coefficient at the event time step as function of the radar processing strategy for various radar range intervals and the three groups of rain events. 52

Figure 3.9: Rainfall fields at the event time scale over the OHM-CV window for the rain events of 8-9 September 2002, 21 November 2002 and 10-13 December 2002. 53
Figure 3.10:Presentation of the study area: a) Relief map of north-eastern Italy and location of the Monte Grande weather radar; b) Location of the Posina and Alpone basins and the raingauge network. 56
Figure 3.11: Maps of estimated power loss due to beam blockage calculated with a beam propagation model and DEM data at three different beam elevation scans: 0,5°, 1,0° and 1,5°. 59
Figure 3.12: Altitude of the 0°C isotherm and of observed VPR peak for OCT96. 60
Figure 3.13: Scatterplot of radar estimates and raingauge event accumulations for the OCT92 event. 63

1. Introduction

The quantitative interpretation of the weather radar signal in terms of rainfall is complex since it depends (i) on the rainfall variability at all scales (scales of the raindrops, of the radar resolution volume and of the precipitating system itself), (ii) on the radar detection domain, constrained by the surrounding relief and the vertical development of precipitations, and (iii) on the parameters and operating protocol of the radar system(s) employed. A pronounced relief obviously adds complexity to the radar quantitative precipitation estimation (QPE) problem by reducing the visibility and increasing environmental noise. A number of authors have already addressed the specific subject of radar QPE in mountainous regions (e.g., Joss and Walvogel 1990; Westrick et al. 1999; Young et al. 1999; Germann and Joss 2002; Pellarin et al. 2002; Dinku et al. 2002, Germann et al. 2006, to give some examples). However, a great deal of operational and research effort is still required to optimize the observation strategies and data processing techniques. This effort is fully justified by the potentially higher utility of weather radar systems in mountainous regions compared to flatland regions. Mountains induce a wide range of meteorological phenomena at the mesoscale, including generation and intensification of precipitation. Furthermore, mountainous topography increases the streamflow volumes and accelerates their concentration. These two factors put a strong emphasis on the requirement for real-time quantitative precipitation estimation (QPE) in order to mitigate flood and flash-flood hazards in such mountainous areas.

In a first part, a number of innovative radar QPE algorithms developed within FLOODsite are described in section 2. Such developments are partly backed on the Bollène-2002 Experiment realized by the Direction des Systèmes d'Observation (DSO) of Météo-France in cooperation with LTHE/INPG, to start adapting the operation and data processing of the new French radar systems for hydrometeorological applications in mountainous regions (section 2.1). For this purpose, an experimental volume scan protocol was implemented for the Bollène S-Band radar system network during the autumn 2002. A ground clutter identification (GCI) technique based on the pulse-to-pulse variability of the reflectivity is presented in section 2.2. The description and adaptation of two rain-type separation algorithms following Steiner et al. (1995) and Sanchez-Diezma et al. (2000) is proposed in section 2.3. Section 2.4 is devoted to the vertical profile of reflectivity (VPR) estimation conditional on the rain type. Two approaches are considered with (1) establishment of mean "apparent" VPRs, that is the VPRs estimated by averaging measured reflectivities and (2) adaptation of the inverse method proposed by Andrieu and Creutin (1995) and Vignal et al. (1999) to the case of time-varying geographical supports. The algorithm finally proposed for the coupled identification of the rain types and the VPRs is given in section 2.5. In section 2.6, the problem of rainfall estimation at ground level from corrected reflectivities aloft is addressed. In addition, a stochastic model of range profiles of raindrop size distributions has been developed by the Hydrology and Quantitative Water Management Group of the University of Wageningen (section 2.7). This model has been used for testing the sensitivity of attenuation correction schemes to the DSD variability. Such a work nicely complements the earlier contributions of the partners aimed at quantifying and correcting the radar signal for attenuation, a very sensitive effect for X- and C-band radar systems operating in heavy rainfall (e.g., Delrieu et al. 1997; Delrieu et al. 1999).

In a second part the radar SAS is implemented and assessed in the French and Italian pilot sites using two complementary approaches. For the French case study, the establishment of reference rainfall, based on the dense rain gauge networks of the OHMCV is presented in section 3.1.2. Various radar time and space-time adaptive processing strategies are described in section 3.1.3 together with their implementation conditions. Section 3.1.4 is devoted to the performance evaluation of the selected radar processing strategies. The conclusions and perspectives are drawn in section 3.1.5. The Italian case study conducted by University of Padova is aimed at investigating the sensitivity of the radar SAS to parameter uncertainty and to use this knowledge to outline a feasible methodology for radar rainfall uncertainty estimation using the GLUE methodology. In section 3.2.2, the study area and data

resources available are presented. In section 3.2.3, the radar SAS version used for radar rainfall estimation and its application to the study area are described. The methodology for quantification of radar rainfall uncertainty and the example application is presented in section 3.2.4. Section 3.2.5 gives general conclusions and suggestions on future research and development.

2. The radar SAS: innovative algorithms

2.1 The Bollène-2002 experiment

Table 2.1 presents a list of the Bollène radar system parameters and Table 2.2 describes the experimental scanning protocol implemented during the autumn 2002. The 3 PPIs corresponding to the elevation angles of 0.8, 1.2 and 1.8° were realized every 5 min to keep on establishing the ARAMIS operational products in real time during the experiment. They were complemented by two sets of 5 PPIs, alternated every 5 min, allowing a good sampling of the atmosphere at a 10 min sampling interval. The 0.4° elevation angle was introduced to increase the detection capability of the radar system over the Mediterranean Sea in the southern sector. The antenna rotation speed was adapted as function of the elevation angle: 10°/s for the three operational elevation angles in order to allow a correct functioning of the ground clutter identification (GCI) technique and 15°/s for the remaining angles in order to meet the 5 min revisit time constraint. The data available for each 1 x 1 km² Cartesian mesh of each PPI are: (i) the average reflectivity and (ii) the mean absolute reflectivity difference (MAD) averaged over the individual radar polar bins which centres fall within the corresponding Cartesian mesh. The MAD variable reflects the pulse-to-pulse variability of the reflectivity; it is used for the ground clutter identification (section 2.2).

The operation of the Bollène radar system with the experimental volume scan protocol was successful during the September – December 2002 period. This period was particularly rainy, resulting in the sampling of several intense rain events typical of the North-Western Mediterranean climate. This includes the catastrophic rain event of 8-9 September 2002 due to a quasi-stationary mesoscale convective system which resulted in 24 casualties and severe economic damages in the Gard region (Delrieu et al. 2005). A detailed presentation of this dataset is given in section 3. To illustrate the following discussions in this section, we have selected two examples of rain fields among the Bollène 2002 datasets: (1) one taken during the MCS of 9 September 2002 at 0200 UTC (Figs 2.2 and 2.3) and (2) the other one during a cold front passage on 21 October 2002 at 2030 UTC (Figs 2.4 and 2.5). The raw reflectivity data shown for the two cases (see the 0.8° PPIs in Fig. 2.2a and 2.4a) stress the very strong ground clutter contamination in such mountainous regions for the considered wavelength. Such problem needs to be addressed prior any attempt to use radar data for QPE. Figs. 2.2b and 2.4b show the corresponding MAD reflectivity data which seems to offer some potential for this task with low MAD values for ground clutter and higher values in rain. For the two selected examples (Fig. 2.2-5), rainfall exhibits great spatial variations with a clear co-existence of convective and stratiform regions within single rain fields. For the 9 September 2002 case, deep convection occurs on the southern branch of the V-shaped MCS while a stratiform precipitation trail forms northward. In the case of 21 October 2002, there is a thunderstorm in the south-east part of the region; a cold front located in the center of the detection domain is moving eastward; this front is followed by stratiform precipitation. It is the main challenge of the present work to try taking this rainfall spatial heterogeneity into account in the radar data processing.

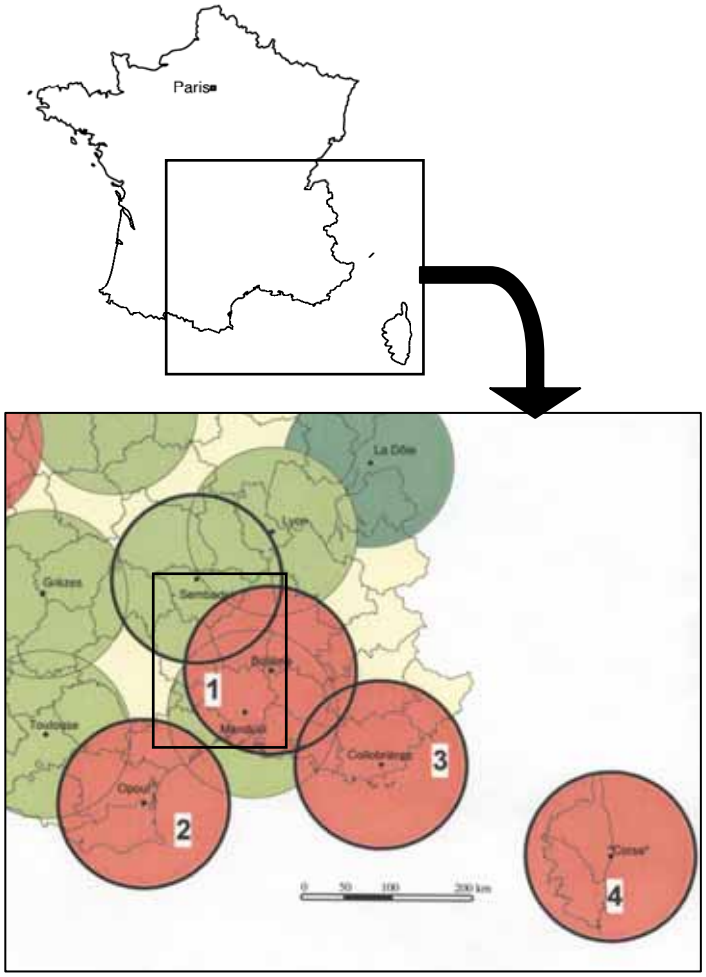


Figure 2.1: Study area in Southeastern France with the localization of the four new S-Band weather radar systems (with 100 km range markers) deployed by Météo-France during the 1999-2004 period to complement the hydrometeorological coverage of the region. The Bollène radar system has number 1. The inner black box delineates the OHM-CV observation window where dense rain gauge networks are available for the evaluation of the radar processing techniques developed during the Bollène-2002 Experiment.

TABLE 2.1. Parameters of the Bollène radar system

Type	MTO2000
Location	
	Bollène
x-coordinate (km, Extended Lambert II)	792.5
y-coordinate (km, Extended Lambert II)	1927.6
Altitude (m ASL)	327.0
Transmitter-receiver	
Peak power (kW)	600
Frequency (GHz)	2.8
PRF (Hz)	250
Pulse width (μs)	2
Minimum detectable signal MDS (dBm)	-113
Dynamic range (dB)	80
Antenna	
Diameter (m)	6.2
Beamwidth at half-power point (°)	1.28
Power gain (dB)	42.5

TABLE 2.2. Volume scanning protocol implemented for the Bollène radar system during autumn 2002. The 3 PPIs in bold character are sampled every 5 min. They served for keeping on establish the real-time products during the Bollène 2002 Experiment.

Cycle 1	Elevation angle (°)	Antenna rotation speed (°/s)	Cycle 2	Elevation angle (°)	Antenna rotation speed (°/s)
1	0.4	15	1	17.0	15
2	14.0	15	2	11.0	15
3	9.0	15	3	7.2	15
4	6.0	15	4	4.8	15
5	3.6	15	5	2.4	15
6	1.8	10	6	1.8	10
7	1.2	10	7	1.2	10
8	0.8	10	8	0.8	10

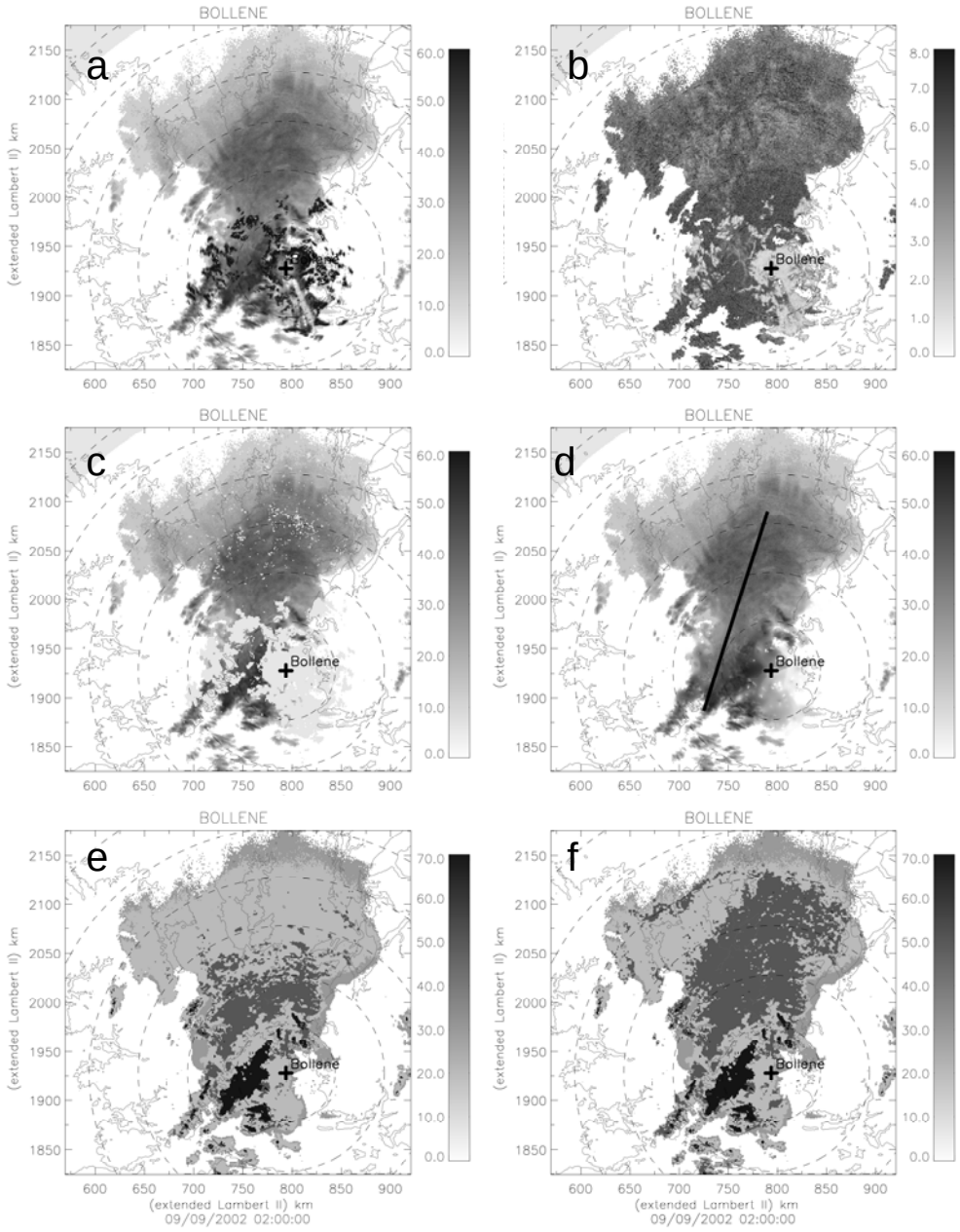


Figure 2.2: Case of the mesoscale convective system observed on 9 September 2002 at 0200 UTC. a- raw mean reflectivity; b- mean absolute difference (MAD) in reflectivity values; c- mean reflectivity after ground clutter identification; d- mean reflectivity after interpolation; e- results of the first step of the rain separation (black: convective rainfall; dark grey: stratiform rainfall; light grey: undetermined); f- results of the final rain separation (same convention as e). Note that a-d correspond to reflectivity and MAD measurements for the 0.8° elevation angle while e-f are maps of rain types determined with the full volume data.

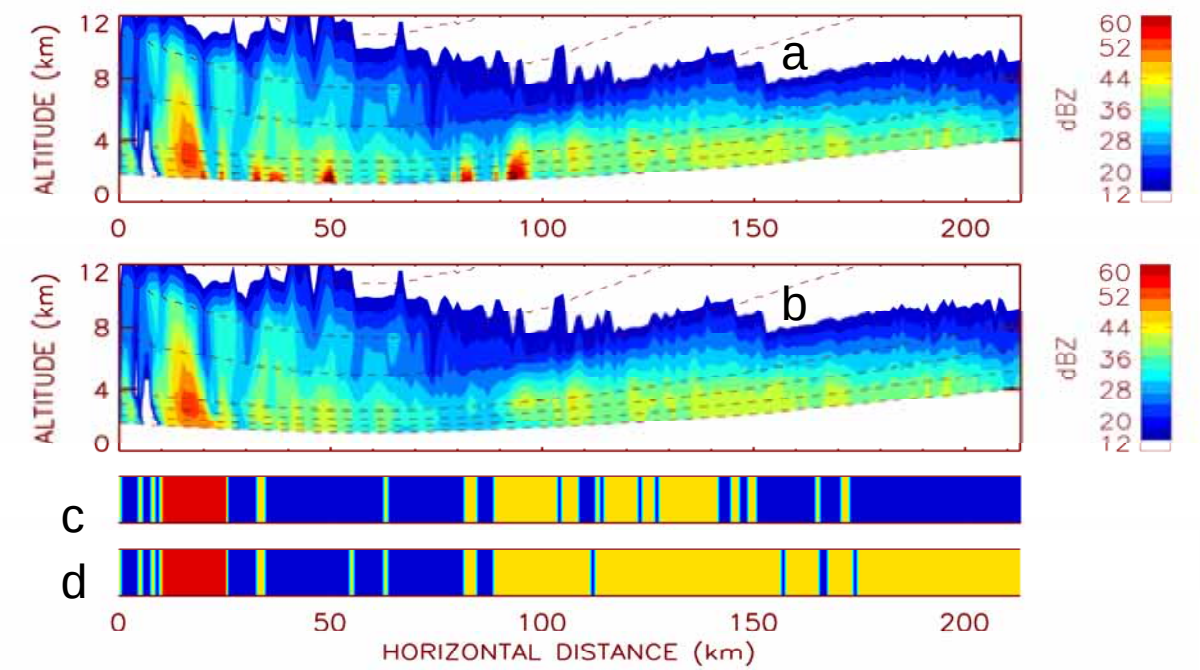


Figure 2.3: Vertical cuts in the volume radar data for the case of 9 September 2002 at 0200 UTC along the line shown in Fig. 2.2d. a- raw mean reflectivity; b- mean reflectivity after GC identification and interpolation; c- coloured bands indicating the results of the first rain type separation (red: convective rainfall; yellow: stratiform rainfall; blue: undetermined); d- coloured band indicating the final rain type separation results.

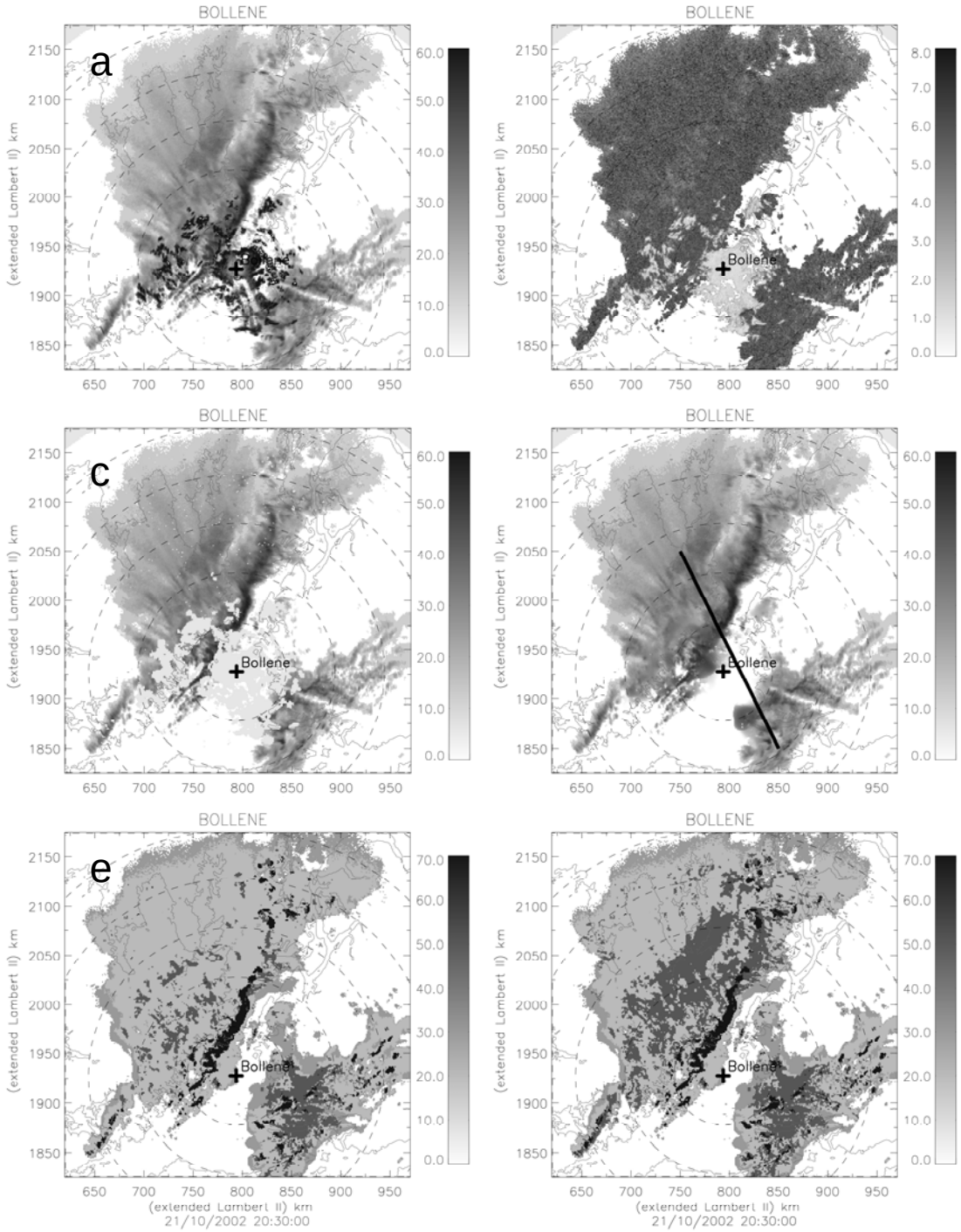


Figure 2.4: Same as Fig. 2.2 for the cold front case of 21 October 2002 at 2030 UTC.

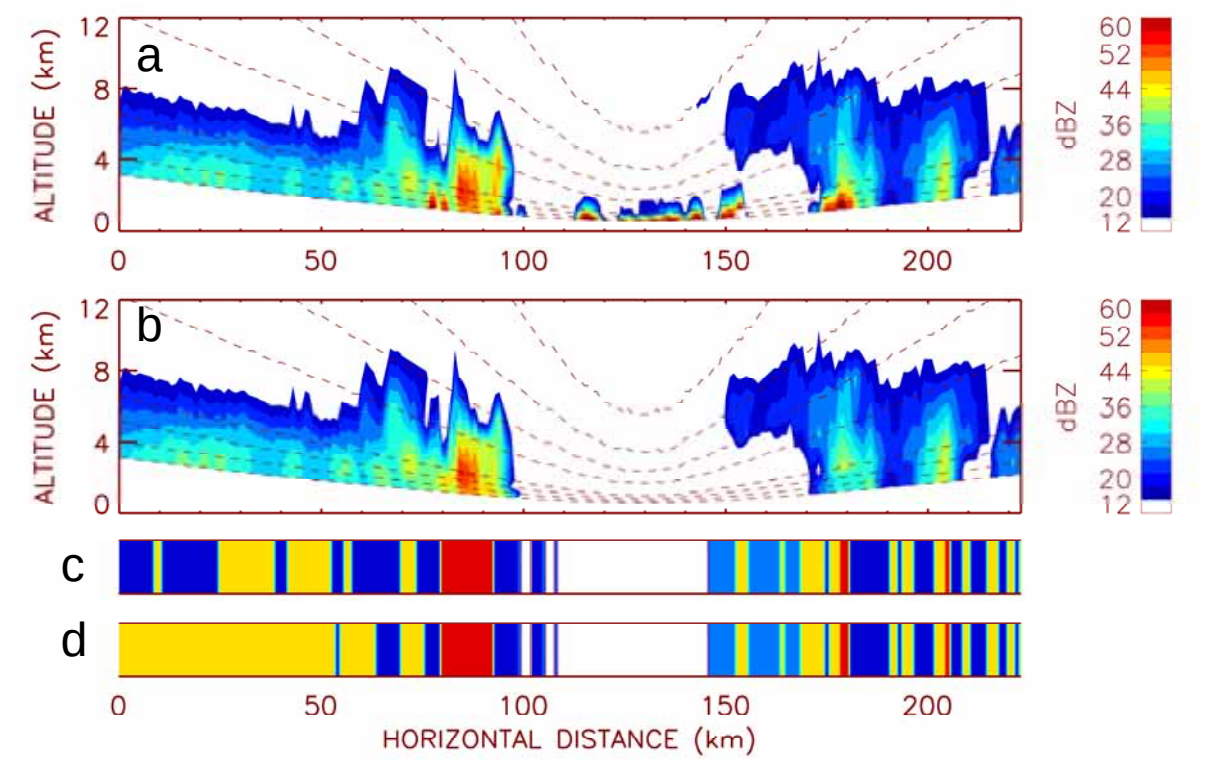


Figure 2.5: Same as Fig. 2.3 for the cold front case observed on 21 October 2002 at 2030 UTC.

2.2 Adaptive clutter identification and correction

Figure 2.6 presents dry-weather ground clutter characteristics of the Bollène radar system for two selected elevation angles (0.8 and 3.6°). The dry-weather reflectivity and mean absolute difference values were processed over a 10-day dry weather data set to evaluate the occurrence ($OCC_{dry}(j)$ where j denotes a given Cartesian pixel), the time-averaged reflectivity ($\overline{Z_{dry}(j)}$) and MAD ($\overline{MAD_{dry}(j)}$) fields. Note that $\overline{Z_{dry}(j)}$) and $\overline{MAD_{dry}(j)}$ are conditional means, that is means calculated for the time series corresponding to reflectivity values exceeding 12 dBZ. The black areas in top graphs of Fig.2.6 correspond to almost permanent clutter. The mean reflectivity map for the 0.8° elevation angle (middle left) indicate that ground clutter is particularly strong in the vicinity of the radar site for the lowest elevation angles as the result of side lobe returns from the numerous anthropic targets (highways, roads, railways, urbanization, electric lines…) present in the Rhône valley. At ranges between 50 and 100 km, the Cévennes mountains west of the Bollène radar also produce intense radar returns due to interception of the main antenna lobe. The intense clutter is clearly associated with low mean MAD values (bottom-left figure in Fig. 2.6). Within the 100-km range and along the Rhône valley, in addition to the intense ground clutter there is a rather uniform pattern of

less intense radar returns associated with high mean MAD values, as the probable result of clear air echoes which are often observed before dawn and after dusk in the region. In the low-occurrence clutter region, both the mean reflectivity and MAD maps evidence additional sources of noise including (1) radials in the south-west direction associated to sunset and (2) the classical signature of interferences between the Bollène and Nîmes radars. Note that both noise sources are associated to high MAD values making their detection difficult. When the elevation increases (left panel in Fig. 2.6), noise associated to the relief is obviously reduced. However contamination by aircraft lines becomes very significant. This detailed inspection of dry-weather clutter characteristics evidences the importance and the complexity of the radar data "cleaning". Determination of the radar detection domain also requires determination of the screening effects associated to the radar beam interception by the relief and other anthropic targets. This has been done here with the geometrical procedure proposed by Delrieu et al. (1995). Illustration of the Cévennes screening effects are given in section 3.

Nicol et al. (2004) developed a method for detecting ground clutter based on the inter-pulse variability of non-Doppler radar returns. A large data set of pulse-to-pulse reflectivity data collected by Météo France with a C-band radar located in Trappes (Paris region) was used to analyse the variability of clutter and weather echoes. The proposed method utilizes two criteria, the mean absolute difference (MAD) which reflects the degree of pulse-to-pulse variability, and the absolute mean difference (AMD) to identify the strong gradients that are often present at the edge of ground-cluttered regions. These two variables are defined as:

$$MAD_{i,n,N} = \frac{1}{N}\sum_{k=i-N/2}^{i+N/2}\left|Z_{k-n/2} - Z_{k+n/2}\right| \quad (2.1)$$

$$AMD_{i,n,N} = \left|\frac{1}{N}\sum_{k=i-N/2}^{i+N/2}\left(Z_{k-n/2} - Z_{k+n/2}\right)\right| \quad (2.2)$$

where Z is the reflectivity value in dBZ, i is the pulse index, n the pulse separation and N the number of consecutive estimates used to calculate the means.

A specific work was dedicated within the Bollène 2002 Experiment to adapt this method to the considered context. Firstly, tests were realized prior to the experiment for selecting the antenna rotation speed, a convenient time separation between the pulses ($t_s = n / PRF$) and the number of pulses (N) to be averaged in the evaluation of the polar *MAD* values. Such polar values are then averaged over 1-km^2 Cartesian meshes. The values of 10°/s, $t_s = 8$ ms ($n = 2$) and $N = 40$ were found to be reasonably suited for the considered case owing to the constraint on the number of PPI (8) to be explored within the 5-min revisit time. Secondly, the parameterization of the adaptive ground clutter identification (GCI) was defined based on the analysis of the clutter characteristics during dry-weather and rain events. The GCI procedure, made of three steps, is summarized in Table 2.3. The first step utilizes a combination of pre-defined clutter maps observed during non-raining days (Fig. 2.6) and the MAD measurements at the time when the identification is to be performed ($MAD(j,t)$ where j denotes a Cartesian pixel location and t the time). Four clutter categories were defined. Three categories correspond to persistent clutter and the last one to sporadic clutter defined with respect to a $OCC_{dry}(j)$ threshold value of 3%. For the sporadic clutter case, the pixels with $MAD(j,t) < 3\ dBZ$ are flagged as clutter. For the persistent clutter cases, a stratification of the $MAD(j,t)$ thresholds as function of the $\overline{MAD_{dry}(j)}$ values proved to be effective in discarding a lesser number of measurements of precipitation when it is dominant over ground clutter. As a second step, all measurements directly adjacent to clutter identified by their *MAD* values are removed if the maximum local gradient ($MaxAMD$) is greater than $6\ dBZ\ km^{-1}$. This is related to the fact that large gradients in the clutter field, due to the antenna movement over non meteorological targets, may lead to increased *MAD* values inhibiting clutter detection. Note that due to the non-availability of the polar pulse-to-pulse reflectivity data in the present configuration, *AMD* values are derived from the

Cartesian mean reflectivity fields and not from (2). A third step was found necessary to remove clutter for screened or isolated (e.g. associated to aircraft or interferences) pixels (Table 2.3).

An interpolation scheme is then applied to fill in the ground-cluttered regions. Due to the large size of such regions in our case study, this point was found to be critical and received special attention. We finally selected the following horizontal interpolation method: (1) reflectivity values are averaged after conversion in rain rates using a given *Z-R* relationship and by considering inverse distance weights; (2) Cartesian neighborhoods of increasing order (e.g., order 1: 8 surrounding pixels; order 2: 24 pixels surrounding pixels, order 3: 48 pixels, etc) are successively screened; (3) for a given order, the interpolated value is calculated only if non-interpolated values are available for more than 50% of the pixels. A maximum order of 4 is considered. A preliminary processing of the screening effects is also realized at this stage: for screening correction factors less than 2 dB, the screened reflectivity value is corrected while for greater correction factors, the screened reflectivity is set to a missing value. To be strict, note that such screening correction factors are actually incorrect since they are based on the hypothesis of a uniform beam filling (which means that VPR effects are neglected); the correction actually used in a final step accounts for both the screening effect and the VPR (section 2.7). It was found relevant to apply such pre-processing for the ground-cluttered and screened regions before the rain type identification (section 2.3) in order to minimize missing data and avoid spurious gradients within the reflectivity fields. Note however that the interpolated pixels are flagged so that they are actually not accounted for in the VPR estimation (section 2.4).

Figures 2.2-a,c,d and 2.4-a,c,d illustrate the rather good functioning of the ground clutter identification and interpolation for the 0.8° PPI data. Comparison of the vertical cuts before and after correction (Figs 2.3a and 2.3b; Figs 2.5a and 2.5b) confirms that the procedure works reasonably well. A detailed assessment in terms of rainfall estimation is given in section 3 with respect to the OHMCV raingauge datasets.

TABLE 2.3: Parameterization of the ground clutter identification technique.

	Pixel flagged as ground clutter (GC) if the following conditions are met:
STEP1: dry-weather and rain MAD values	
Persistent clutter 1: $OCC_{dry}(j) \geq 3\%$	$\overline{MAD_{dry}(j)} < 1.8\ dBZ$ and $MAD(j,t) < 5.5\ dBZ$
Persistent clutter 2: $OCC_{dry}(j) \geq 3\%$	$1.8 \leq \overline{MAD_{dry}(j)} < 2.1\ dBZ$ and $MAD(j,t) < 4.5\ dBZ$
Persistent clutter 3: $OCC_{dry}(j) \geq 3\%$	$2.1\ dBZ \leq \overline{MAD_{dry}(j)}$ and $MAD(j,t) < 3.5\ dBZ$
Sporadic clutter: $OCC_{dry}(j) < 3\%$	$MAD(j,t) < 3.0\ dBZ$
STEP 2: reflectivity gradients	
	for the 8 pixels surrounding a pixel flagged as GC: if $MaxAMD > 6\ dB\ km^{-1}$ the pixel is flagged as GC, as well
STEP 3: additional criteria	
	If a pixel is flagged as GC at a given elevation, all the lowest elevation pixels are flagged as GC Isolated pixels (one single reflectivity value greater or equal to 12 dBZ over the vertical) are flagged as noise

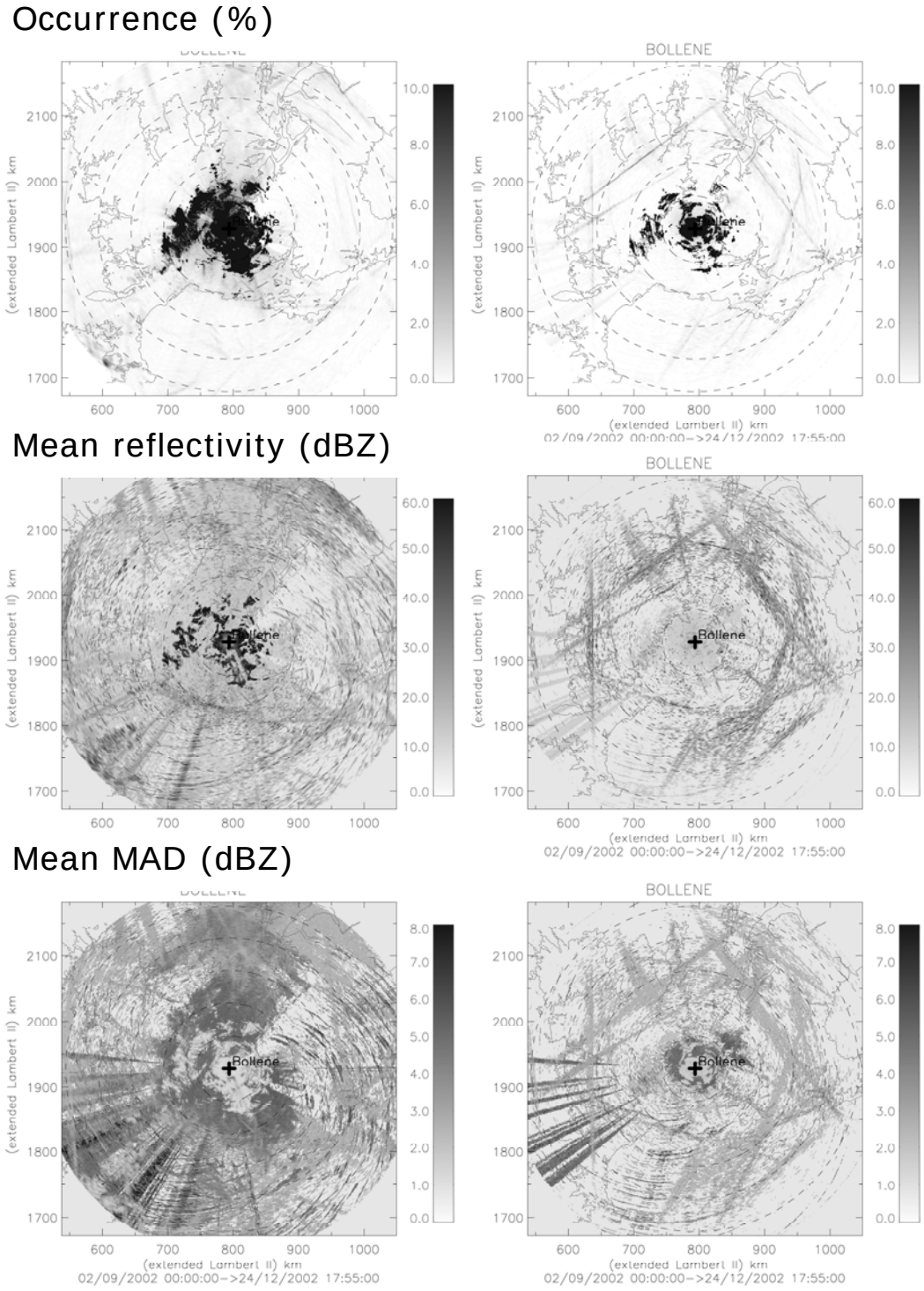


Figure 2.6: Dry weather clutter characteristics for the 0.8° (left) and 3.6 ° (right) PPIs derived from a sample of 10 days during the Bollène 2002 Experiment. Top - clutter occurrence (%); Middle - conditional mean reflectivity (dBZ); Bottom - conditional mean MAD (dBZ)

2.3 Rain-type separation

Figures 2.3b and 2.5b clearly illustrate the variety of rain types that may exist within a single radar image as the consequence of the spatial and temporal variability of the rain physical processes. This fact is certainly worth being accounted for in the radar data processing for example by using VPR functions and Z-R relationships conditional on the rain types. This attempt to regionalize the radar data processing requires in a first step implementation of automatic rain separation techniques. Since vertical velocity data are not available with the non-coherent radar systems employed here, the methods developed use 3D reflectivity data alone. The work described hereafter is mainly backed on the algorithms proposed by Steiner et al. (1995) for the identification of convective cells and by Sanchez-Diezma et al. (2000) for the detection of the bright band, indicative of stratiform rainfall. It should be stressed at this point that the rain-typing concept presents inherent limitations due to the radar sampling characteristics. Two examples, related to time and range sampling can be evoked. Firstly, concerning time sampling issues, it was initially hoped that the rain fields would be stationary enough within the 10-min period to allow use of the full volume data without synchronisation, a rather difficult task for such 3D data. For radar sequences with fast-moving rainfall systems, this assumption was found to be not acceptable: this was evidenced with "sawtooth" - shaped vertical profiles of reflectivity (not shown here for the sake of conciseness). We decided to step back to the 5-min volumes, in spite of the resulting loss in terms of volume resolution. Secondly, there are obvious observation limitations at long ranges (typically 80 km and more) with the volume scanning protocol implemented, e.g. for the bright bands in the right part of Fig. 2.3b and the left part of Fig. 2.5b.

In the following, we briefly present the Steiner et al. (1995) and the Sanchez-Diezma et al. (2000) algorithms and list the main adaptations suggested after their implementation in our case study (a more detailed presentation may be found in Chapon 2006).

2.3.1 Review of two existing algorithms

Steiner et al. (1995) proposed a well-known approach for the identification of convective precipitation using three criteria applied to reflectivity fields. The first two criteria aim at identifying the centres of convective cells. The first one is a reflectivity threshold (e.g., 40 dBZ) over which it is assumed that precipitation can only result from convective processes. The second one is a "contrast" criterion: a pixel is assumed to be a convective centre if the reflectivity value exceeds the conditional mean reflectivity (also termed as the background reflectivity Z_{bg}), evaluated over a surrounding region, from a given reflectivity difference ΔZ (in dBZ). This criterion is parameterized by the size of the surrounding region (circle with a radius of 11 km in the original paper) and by a function expressing the ΔZ threshold as function of the background reflectivity. The function implemented in the present study is defined as:

$$\Delta Z = a \cos\left(\frac{\pi Z_{bg}}{2 b}\right) \tag{2.3}$$

with $a = 8\ dBZ$, $b = 42.5\ dBZ$, the background average reflectivity Z_{bg} being also expressed in dBZ. Note that the cosine formulation was proposed by Yuter and Houze (1997) and that the parameterization corresponds to the function actually used by Steiner et al. (1995).

The third criterion defines a convective circular region associated to each pixel identified as a convective centre by one of the above criteria. The so-called convective radius R_C in km is defined as:

$$R_C = Min\ (5,\ 1 + Int((Z_{bg} - Z_1) / 5)) \tag{2.4}$$

where Min and Int are the "Minimum of" and "Integer part of" functions. The variable Z_1 is a parameter proposed to be set to 15, 20 or 25 dBZ by Steiner et al. (1995) to define large, medium or

small "regions of influence", respectively. The convective radius R_C typically varies between 1 and 5 km depending on the background reflectivity. The range variation associated to such values of the Z_1 parameter is $\pm 1\ km$ with respect to the medium radius. Each Cartesian pixel whose centre belongs to the resulting circle is flagged as convective.

Sanchez-Diezma et al. (2000) proposed a method for identifying the bright band within volume scan radar data, as an indicator of stratiform precipitation. Basically, the method screens the vertical profiles of measured reflectivity for a peak exceeding a given reflectivity difference ΔZ_{BB} with respect to the reflectivity values above and below the peak. Two iterations are performed. The first one seeks for intense peaks ($\Delta Z_{BB} > 5\ dBZ$) over the entire altitude range. The second one refines the determination of the bright band spatial extension by considering a reduced peak ($\Delta Z_{BB} > 2\ dBZ$) over an altitude range around the average bright band altitude determined at the first step (an altitude range of $\pm\ 0.6\ km$ is proposed).

2.3.2 Implementation of the two algorithms

Both algorithms were implemented "as such" on the radar datasets available. As suggested by Steiner et al. (1995), their adjustment/evaluation was done by visual inspection of the identification results both in the horizontal and vertical planes throughout the radar dataset available. After this evaluation phase, several comments can be listed.

About the Steiner's algorithm:
The sensitivity study showed that this algorithm is better to be applied to individual PPIs rather than to 2D composites of the radar volume data such as CAPPIs or vertical projections of the maximum reflectivity. Such composite products clearly mix vertical and horizontal reflectivity gradients and are consequently not appropriate.
Table 2.4 illustrates the operation of the convective algorithm applied to each single PPI for the case of 9 September 2002 at 0200 UTC. The number of convective detections logically decreases with increasing elevation angles. The proportion of detections with criterion 1 is rather constant for the lowest elevation angles, then it drops to 0 for the upper elevation angles. Criterion 2 acts in a complementary way with a detection proportion increasing from about 5 % for the low elevation angles up to 30% for the highest elevation ones. The reflectivity difference function, depending on the background reflectivity value, therefore appears effective to partly account for the decrease of the reflectivity as function of the altitude, a fact not accounted for by criterion 1. The use of criterion 2 alone (not illustrated here) proved to be less satisfactory than the combined use of the first two criteria. Table 2.4 also indicates that the proportion of convective detections by criterion 3 is relatively high and increases with increasing elevation angles.
The algorithm was found to produce in some instances spurious convective detections at the altitude of the bright band in stratiform regions. These spurious detections were made by criterion 1 and the utilization of criterion 3 was found to strongly aggravate the problem. Special procedures were implemented in our final algorithm to cope with this problem (section 2.5).

About the Sanchez-Diezma stratiform algorithm:
the bright band detection capability was found to depend greatly on the scanning protocol (number and values of the elevation angles) and the bright band altitude itself. This capability very significantly decreases with increasing ranges due to both (i) the increase of the radar volume size and altitude above ground and (ii) the reduced number of sampling points in the vertical. We found a benefit in merging the stratiform regions determined at successive time steps with the cycle 1 and cycle 2 protocols (section 2.6).

As already mentioned, both the convective and stratiform algorithms suffer inherent limitations, especially at long ranges, due to the radar sampling properties. These effects are certainly difficult to

account for in the present formulation and parameterization of the algorithms. To overcome these difficulties, we propose in section 2.5 a coupled identification of the rain types and the VPR. Basically, from the rain typing sensitivity study, we derived a decision tree which allows a rather satisfactory rain type separation at close range (e.g., less than 60-80 km) with slightly adapted versions of the Steiner et al. (1995) and Sanchez-Diezma et al. (2000) algorithms. This preliminary partition is used for the identification of vertical profiles of reflectivity conditional on the rain types. In turn, the identified VPR are used to improve the rain separation over the entire detection domain, assuming spatial stationarity of the vertical structures of rainfall. The VPR identification conditional on the rain type is addressed in the next section.

TABLE 2.4: Detailed results of the Steiner's algorithm for the case of 0200 UTC 9 September 2002. For each elevation angle, the total number of convective pixels detected and the proportions of pixels identified by each criterion are given. Note that criterion 2 is applied in complement to criterion 1.

Elevation angle (°)	17	11	7.3	4.8	2.4	1.8	1.2	0.8
Total number of convective pixels	32	597	1730	2769	3373	3417	3387	3327
Criterion 1 (percent)	0	7	16	28	50	52	56	56
Criterion 2 (percent)	31	33	20	11	6	6	5	4
Criterion 3 (percent)	69	60	64	61	44	42	39	40

2.4 VPR identification conditional on rain types

After a clarification of the concept of VPR, we describe hereafter two procedures for its estimation. Firstly, like in the work of Germann and Joss (2002), we may consider the so-called apparent VPR, that is the VPR estimated by averaging measured reflectivity values. This apparent VPR is influenced by radar sampling effects which tend to smooth the true VPR shape; therefore, the apparent VPR should be estimated in regions situated close to the radar site. Secondly, we consider the VPR inversion method proposed by Andrieu and Creutin (1995). This method allows to filtering the radar sampling effects in the VPR estimation. It was adapted by Kirstetter (2008) to the case of time-varying geographical supports. Both approaches (apparent or inverse VPR) can be applied with or without a preliminary rain typing performed with the procedures presented in section 2.3.

2.4.1 Definition of the vertical profile of reflectivity

We define the VPR $\overline{z(h)}$ as the ratio of the expected values of the reflectivity at a given altitude h and at a reference altitude h_0 close to the ground. The expectation is taken over a given space-time domain, with or without rain typing:

$$\overline{z(h)} = \frac{E(Z(h))}{E(Z(h_0))} \tag{2.5}$$

This definition calls for a number of comments:

- The VPR function characterizes the mean heterogeneity of the reflectivity field in the vertical. Obviously, the vertical heterogeneity of rainfall is the result of complex micro-physical processes and the variability around the VPR function is likely to be large.

- One practical problem in the VPR estimation lies in the fact that the measured reflectivity values integrate the VPR over a given altitude range (e.g. 2.1 km at a range of 100 km if one considers a 1.2° 3-dB beamwidth). Averaging measured reflectivities produces VPR functions smoother and smoother as long as the radar range increases (illustrations are given in Vignal et al. 1999).
- We consider for the VPR a normalized reflectivity function. From a practical point of view, it can be seen and used as a "transfer function" allowing both (1) the deconvolution of a radar measured reflectivity at a given altitude and range and (2) its extrapolation at ground level.
- The ratio of the expected values proposed in (2.5) proved to be much less sensitive to extreme (and often spurious) reflectivity values than the expectation of normalized reflectivities (this statement will not be illustrated herein for the sake of conciseness).

2.4.2 Probability density functions of the measured reflectivity as function of the altitude

Figure 2.7 illustrates the 3D-reflectivity variability for the example of 9 September 2002 at 0200 UTC. The graphs display various quantiles of the probability density functions (PDF) of the measured reflectivity as function of the altitude within the 60-km radar range. On the same row, the three graphs correspond to the rainy, stratiform and convective pixels, respectively, while the sampling sizes are displayed on the graph at the right side of the figure. The top row corresponds to the PDF established by grouping the reflectivity data for a period of 10 min and the second row for the period of 1 hour before the given time. To be more specific regarding the PDF calculations, a radar pixel is considered to be rainy if the averaged measured reflectivity value below the altitude of 1 km is greater than 20 dBZ. To establish an unconditional PDF as function of the altitude for the rainy pixels, all the measured reflectivity values falling below the lowest quantization level (12 dBZ here) at altitudes greater than 1 km are artificially set to 0 dBZ. Note that for the convective apparent reflectivity profiles, the analysis is restricted to the pixels determined as convective with the Steiner's criteria 1 and 2. This is done since the apparent reflectivity profiles identified with the third Steiner's criterion were found to be very noisy.

Figure 2.7 shows the large spread of the reflectivity PDFs for the ensemble of rainy pixels (e.g., a 20-80 % inter-quantile range of about 23 dB at an altitude of 2 km for the 10-min PDF). The rain-typing algorithms perform an efficient sorting, leading to reduced inter-quantile intervals (e.g. 20-80% inter-quantile ranges of 8 and 15 dB, for the convective and stratiform PDFs, respectively, at an altitude of 2 km) and distinct median profiles (e.g., median values of 48 and 33 dBZ for the convective and stratiform PDF, respectively, at the same altitude). Note that the 20, 50 and 80 quantiles of the stratiform and convective reflectivity PDFs are very similar for the two time intervals of 10 and 60 minutes. This fact probably depends on the dynamics of the rain systems and should not be generalized without care. However, we will be using this argument of a relative stability in time of the typed-reflectivity PDFs to consider space-time domains extending over the one-hour period before the time of interest, with the obvious objective of stabilizing the rain-typed VPR estimation.

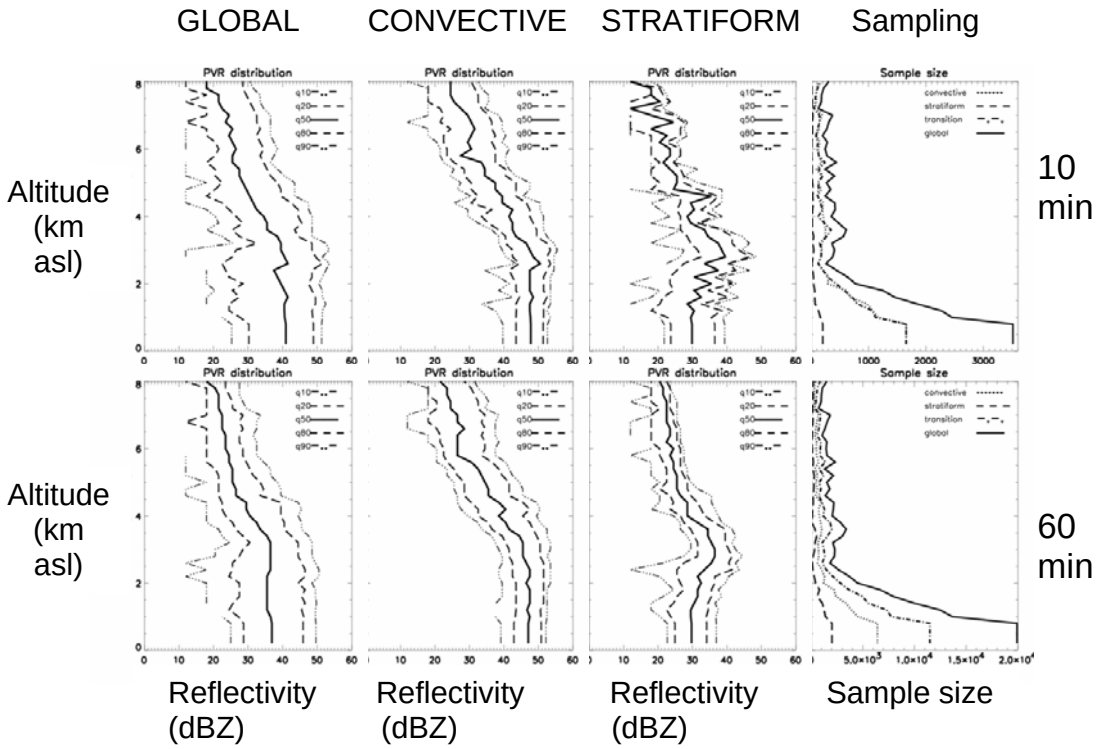


Figure 2.7: Illustration of the 3D-variability of the measured reflectivity within the 60-km range for the 0200 UTC 9 September 2002 case. The figures present the 10, 20, 50, 80 and 90% quantiles of the statistical distribution of the measured reflectivity as function of the altitude considering from left to right (1) all the rainy pixels, (2) the convective pixels and (3) the stratiform pixels; the sample sizes are given on the right graph. The top graphs correspond to observations realized between 0150 and 0200 UTC (10 min) while the bottom graphs correspond to observations realized between 0100 and 0200 UTC (1 hour).

2.4.3 Apparent VPR

The apparent VPR is a first class of estimator for the VPR function (2.5) obtained by averaging measured reflectivities. We have considered here two apparent VPR estimators which can be described by the following single equation:

$$\overline{z_a^*(h_i)} = \frac{\left(\sum_{j=1}^{N(h_i)} w_{ij}(h_1 - h_i)\, Z_{mj}(h_1)\right) \Big/ \left(\sum_{j=1}^{N(h_i)} w_{ij}(h_1 - h_i)\right)}{\left(\sum_{j=1}^{N(h_i)} w_{0j}(h_2 - h_0)\, Z_{mj}(h_2)\right) \Big/ \left(\sum_{j=1}^{N(h_i)} w_{0j}(h_2 - h_0)\right)} \qquad (2.6)$$

The apparent VPR is discretized into a number of altitude classes covering the troposphere (60 classes with a 200 m width here). The term at the denominator of (2.6) allows normalization of the reflectivity profile. It is elaborated with measured reflectivity values observed in the so-called reference altitude range, symbolized by h_0, taken here equal to [0 – 1 km asl]. $Z_{mj}(h_1)$ and $Z_{mj}(h_2)$ (expressed in mm^6m^{-3}) are measurements of the reflectivity at a given moment and location (symbolized by subscript j) observed above and within the reference altitude range, respectively. Note that estimating the normalization term *strictly* with the subset of $N(h_i)$ observations available simultaneously at the two altitude classes h_i and h_0 is an important condition to avoid VPR bias. The two estimators differ on the choice of the weights w_{ij}. For the first one, denoted $\overline{z_{a1}^*(h)}$, we select for the altitude class h_i only the reflectivity measurements for which the altitude of the resolution volume center falls within the considered altitude class; the weight w_{ij} is set to 1. For the second one, denoted $\overline{z_{a2}^*(h)}$, we account for the fact that a radar measurement made at an altitude h results from the integration of the VPR over an altitude range determined roughly by the 3-dB beamwidth and the radar range. The weights are evaluated using the Gaussian approximation for the normalized power gain pattern of the antenna. With this procedure, a reflectivity measurement is actually distributed over a number of altitude classes, depending on the antenna characteristics and range of the measurement. This physically-based averaging procedure allows giving more weight to the radar measurements realized close to the radar site. As such, it accounts for the radar sampling properties but this should not be confused with a VPR inversion technique (see next paragraph) which is aimed at *filtering* the radar sampling properties.

Figures 2.8 and 2.9 display the apparent VPRs that were computed for the example cases with the two variants described above. The normalized median of the reflectivity PDF is also displayed in these graphs. Three points may be outlined:

- The average apparent VPRs depart significantly from the normalized median VPRs, generally towards higher values, as the result of the skewed reflectivity distributions and the influence of high (and sometimes spurious) reflectivity values.
- The $\overline{z_{a1}^*(h)}$ VPR estimator is clearly noisier than the $\overline{z_{a2}^*(h)}$ estimator. The latter will then be preferred in the following. Note however that, apart from the high frequency fluctuations as function of the altitude, both estimators are pretty close to each other while one would have expected significant differences between them. This result is an indication of the relative homogeneity of the VPR and to limited radar sampling effects within the considered geographical domain (radar range less than 60 km) for the considered cases.
- Again, the apparent VPRs estimated at the hourly time step are much stable than the apparent VPRs estimated at the 10-min time step, a confirmation of the need to increase the estimation time-window.

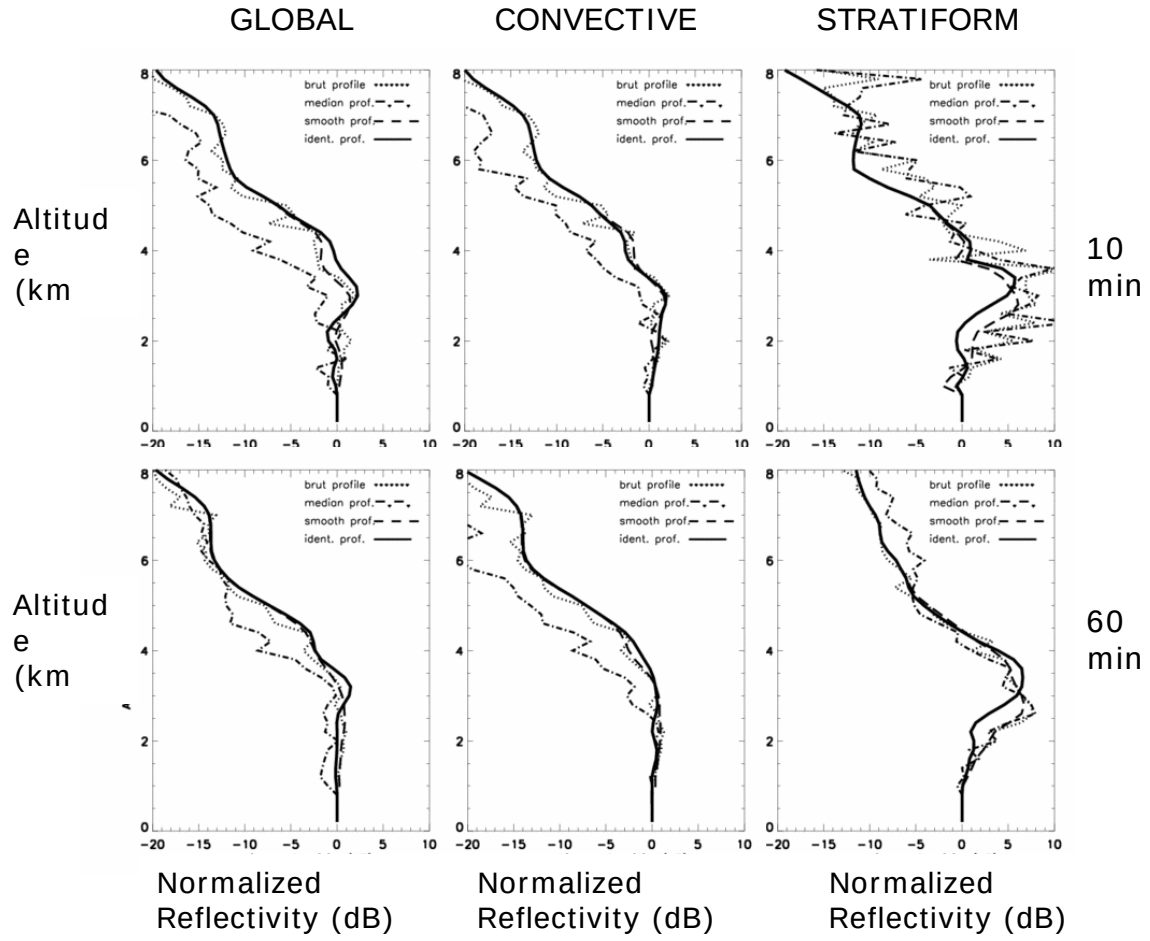


Figure 2.8: Normalized reflectivity profiles (expressed in dB) for the 0200 UTC 9 September 2002 case. Each figure presents (1) the median profile normalized by the average reflectivity value in the first kilometer above sea level (dash-dotted line), (2) the two apparent VPR profiles determined without (dotted line) and with (dashed line) the radar beamwidth weighting function and (3) the inverse VPR (thick continuous line). On a given row, the graphs correspond to the VPR functions estimated globally (left), for the convective region (center) and for the stratiform region (right). The estimation time step is 10-min for the top graphs and 1 hour for the bottom graphs. The median and apparent profiles are established using reflectivity measurements within the 60-km range while the inverse VPR estimation utilizes reflectivity measurements within the 120-km radar range.

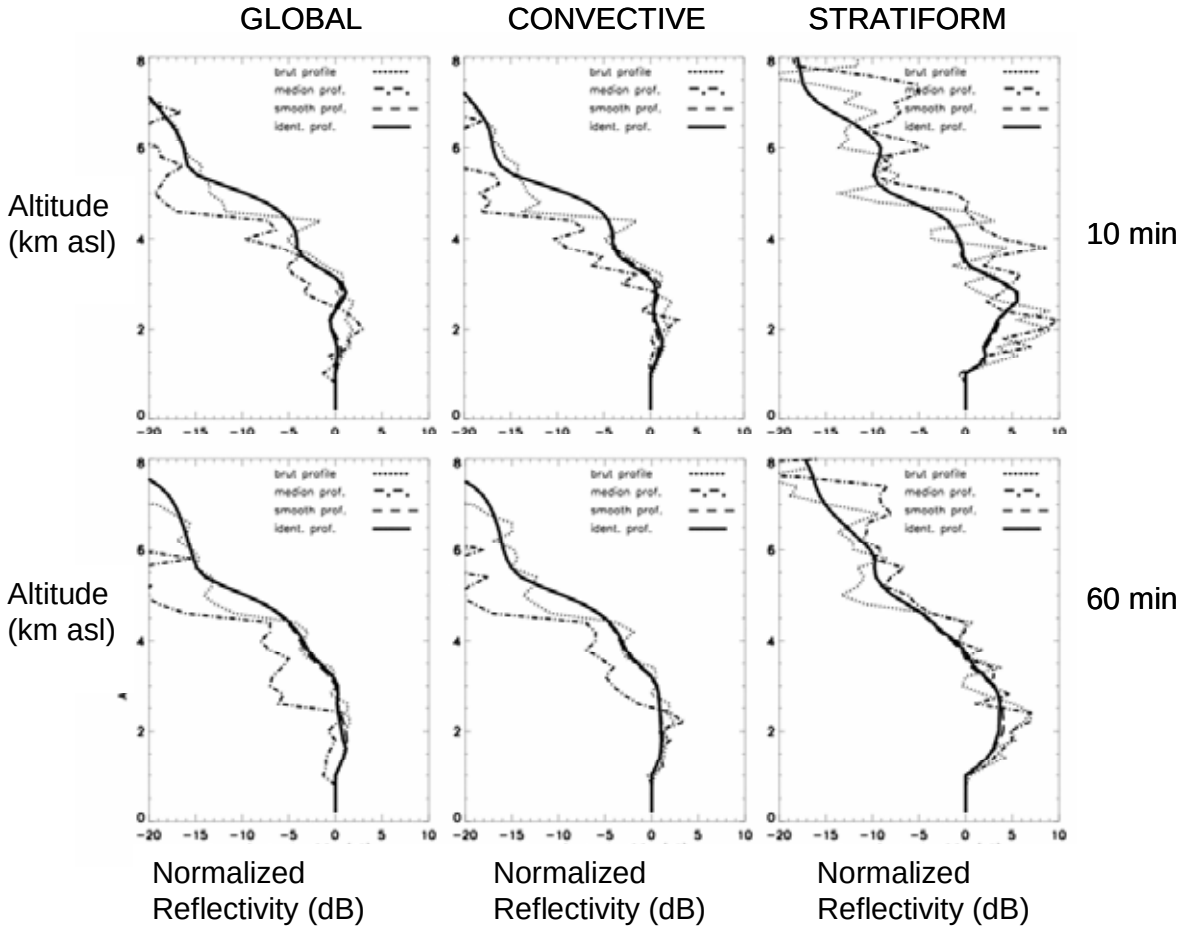


Figure 2.9: Same as Fig. 2.8 for the 2030 UTC 21 October 2002 case.

2.4.4 Inverse VPR

The VPR inversion method, initially proposed by Andrieu and Creutin (1995), Andrieu et al. (1995) and further developed and assessed by Vignal et al. (1999; 2000) and Vignal and Krajewski (2000), was adapted in the present study context to the case of time-varying geographical supports (Kirstetter 2008). We recall here that the method works with the ratios of measured reflectivities. With the hypothesis of a decomposition of the reflectivity into independent horizontal and vertical multiplicative components, such ratios allows to filtering the horizontal variation of the reflectivity. With simplified notations, the radar reflectivity ratio may be written as:

$$q(x,\alpha_i,\alpha_{ref}) = \frac{Z_m(x,\alpha_i)}{Z_m(x,\alpha_{ref})} = \frac{\iiint_{V_i} f^4(\theta,\phi)\,\overline{z(r\cos\theta)}\,dV}{\iiint_{V_{ref}} f^4(\theta,\phi)\,\overline{z(r\cos\theta)}\,dV} \tag{2.7}$$

where Z_m are measured reflectivities at a given point of the radar detection domain symbolised by x for two elevation angles α_i and α_{ref}; (r,θ,ϕ) are the spherical coordinates describing the position of any single hydrometeor (note that α is related to the elevation angle by $\alpha = \frac{\pi}{2} - \theta$). The integration of the VPR over the radar resolution volume V is weighed by the two-way antenna power gain pattern $f^4(\theta,\phi)$. It is assumed in this formulation that there is no interception effect such as rain attenuation or screening between the radar and the two considered resolution volumes. Expression (7) represents a non-linear model, denoted $q = m(z)$, between the data (reflectivity ratios) and the VPR function to be estimated. The VPR function is discretized and inverted by maximizing the following likelihood function:

$$\begin{aligned} &\Phi(z,q) = (z - z_0)^T C_z^{-1}(z - z_0) + (q - q_0)^T C_q^{-1}(q - q_0) \\ &q = m(z) \end{aligned} \tag{2.8}$$

where q_0 is the vector of the observed ratios and z_0 is an *a priori* guess for the VPR function. The terms C_z and C_q are the matrices of covariance of the components of the VPR function and that of the observed ratios, respectively (the exponents *-1* and *T* stand for "inverse" and "transpose", respectively). Their specification allows establishing a balance in terms of confidence between the data and the *a priori* information. The solution therefore varies between the VPR providing the best fit for the observed ratios and the *a priori* VPR. The adaptation of the inversion technique in the case of variable geographical domains proved to be difficult in spite of a better satisfaction of the VPR homogeneity assumption by using a preliminary rain-typing algorithm. Three conditions finally allowed successful inversions: (1) aggregating data from several successive time steps (one hour) (2) a major reconsideration of the definition of the covariance matrices and (3) the implementation of a ratio data censoring approach.

As an illustration, the results obtained for the two examples are displayed in Figs. 2.8 and 2.9. Note that the *a priori* VPR used is the apparent VPR estimated by the second formulation of (2.6), thus the comparison of the two curves allows an appreciation of the inversion technique impact. Although smooth compared to the apparent VPR, the identified VPR at the 10-min time step (top graphs of Fig. 2.8 and 2.9) present spurious oscillations in the vertical that are a signature of the relative instability of the inversion. Working at such short time step would require giving more weight to the *a priori* VPR with the possibility of a negligible utility of the inversion technique. The identified VPRs at the hourly time step are much more satisfactory. As expected the identified convective VPR is close to the apparent ones. The identified stratiform VPR presents a finer and higher bright band for the 9 September 2002 case, a result consistent with simulations of beamwidth smoothing effects. The shape of the stratiform VPR of the 21 October 2002 case is less satisfactory with a large and smooth bright band extending over 2 km: a possible explanation may be that the hypothesis of a unique bright band altitude implicitely made by the Sanchez-Diezma's algorithm is not satisfied here with the melting of pre- and post-frontal stratiform precipitation in the identification dataset. It is also interesting to note that the identified VPRs for the ensemble of rainy pixels (termed as "global" in Figs. 2.8 and 2.9) lies between the convective and stratiform identified VPRs, again with spurious oscillations, an expression of the difficulty of the inversion algorithm faced to heterogeneous and contradictory information.
A measure of a better representation of the VPR with the inverse method compared to the apparent VPR, used as *a priori* information, is obtained by assessing the ability of the two models to reproduce the observed ratios. Although this result is systematically observed, this does not mean that the VPR correction using the inverse VPR will do better than the one using the apparent VPR. Due to the

associated computation costs, it will be important (see section 3) to assess the impact of the VPR estimation method in terms of radar QPE. For now, the purpose is to try using the information gained in terms of knowledge of the VPR functions to improve the rain-typing.

2.5 Coupled rain separation and VPR identification

Due to the considerations developed in the previous two sections, the following procedure is adopted for the coupled identification of the rain types and the corresponding VPRs:

2.5.1 Preliminary rain typing

The 5-min volume radar reflectivity dataset pre-processed for ground clutter and screening effects, as described in section 2.2, are considered. The stratiform algorithm (Sanchez-Diezma et al. 2000) is applied with its original parameterization for the determination of the mean altitude of the bright band and of the geographical domain over which it extends. The convective algorithm (Steiner et al. 1995) is applied to each single PPI separately, regardless the stratiform algorithm results. Compared to the original version, two other modifications are implemented: (i) the reflectivity threshold of criterion 1 is set to 43 dBZ (instead of 40 dBZ) and (ii) criterion 3 is discarded.
A decision tree is then considered for making a decision for each Cartesian pixel, based on the convective algorithm outputs for all the elevation angles, the bright band eventual occurrence at the considered point and the bright band altitude. More precisely:

- If there are at least N_{cd} convective detections (out of the 8 elevation angles) outside an altitude range of $\pm 0{,}5\ km$ around the identified bright band altitude, the pixel is classified as convective. The N_{cd} threshold depends on the operating protocol of the radar; it is empirically related to the number of elevation angles falling outside the bright band region as function of range. Typical values considered for the Bollène-2002 operating protocols (Table 2.2) are 4, 3, 2 and 1 for the range classes of (0-20 km), (20-40 km), (40-150 km) and (> 150 km), respectively.
- If a bright-band detection is performed for a given pixel and if the pixel is not already classified as convective, it is classified as stratiform. Furthermore, regarding the bright-band detection problems evoked in section 2.3, an undetermined pixel at a given timestep for which a bright-band detection is done at previous timestep is also considered as stratiform at the considered timestep. This disposition allows us to take a significant advantage from the two-cycle scanning strategy implemented during the Bollène-2002 Experiment.

2.5.2 VPR identification conditional on rain types

The procedure consists in the following three steps:

- The results of the rain-type separation for all the 5-min timesteps within the hour period preceding (and including) the considered 5-min time step are used to estimate the convective and stratiform VPRs with the inversion VPR algorithm.
- These VPRs are used for estimating the reflectivity correction factors for the various elevation angles, as described in Section 2.6.
- They are also used to generate *apparent* convective and stratiform VPRs as function of range to account for both the discrete sampling in the vertical (8 elevation angles) and for beam integration effects. These apparent convective and stratiform mean VPRs are used to refine the rain separation (next paragraph).

2.5.3 Refined rain typing

For the pixels remaining undetermined, we compare using a correlation criterion the local apparent VPR (averaged over the 9 surrounding pixels) with the range-dependent apparent VPRs generated from the identified VPRs. Several tests were performed and proved the method to be very sensitive due to the small number of comparison points (8 at a maximum). Our best method so far consists in extending detection of the stratiform regions by considering a threshold of 0.95 on the correlation coefficient between the local and identified VPRs. Attempts to extend detection of the convective regions failed, a result consistent with the observation of a very high variability of the VPR for the pixels determined as convective with the third Steiner's criterion.

The rain separation results for the two examples are presented in the horizontal plane in Figs 2.2-e,f and 2.4-e,f and with the coloured bands for the vertical cuts displayed in Figs 2.3 and 2.5. The convective regions corresponding to the MCS and the cold front are well identified within the 100 km range. The stratiform regions for both the MCS and cold front trails are considerably and rather consistently extended using the second step of the rain typing based on the VPR comparisons. Excluding the convective detections in the bright band altitude range proved to be very effective in discarding the false convective detections in stratiform regions due to the bright band. Adapting the number of convective detections (N_{cd}) as function of range was also found to significantly improve the convective algorithm performance at all ranges. However, limitations of the separation algorithms at long ranges are visible on the examples displayed, e.g. (1) for the northern part of the cold front (wrongly classified as stratiform) in Fig. 2.2-f; (2) for the thunderstorm in the right part of Fig. 2.5 with rather inconsistent and highly variable detections. Note also the severe ground clutter effects for the considered radar also probably limit the rain-typing algorithm efficiency by creating large regions for which rainfall data is interpolated at low elevation angles.

2.6 2-D rain product establishment from the 3D reflectivity data

Once the rain types and the VPRs have been identified, the question of the establishment of the 2D rain intensity product from the 3D volume reflectivity data can be addressed. This question covers two aspects: (1) estimation of the reflectivity close to the ground from a given elevation angle measurement or a combination of the available measurements over the vertical and (2) application of a Z-R relationship for converting the reflectivity close to the ground into a rain-rate estimate.

Ground-based DSD measurements have started in the OHM-CV window since the autumn 2004 with the objective of establishing specific Z-R relationships conditional on the rain types. Preliminary results are presented by Chapon et al. (2008) but so far robust typed Z-R relationships are still lacking. Therefore, we will consider in the evaluation (section 3) two widely used Z-R relationships, i.e., $Z=300R^{1.4}$ for convective rainfall and $Z=200R^{1.6}$ for other rain types.

Concerning the estimation of the reflectivity close to the ground, several solutions can be considered. Some of them can be termed as "static" since they are not adaptive in time. This is the case for instance with the CAPPI strategy, for which the reflectivity measurements are representative of a fixed altitude range. We may also consider a procedure aimed at selecting the lowest elevation angle free of ground clutter contamination, determined for instance with respect to dry-weather conditions. An adaptive solution was proposed by Germann and Joss (2002) who corrected the reflectivity for VPR effects for each elevation angle using a VPR estimated in real-time. Then, they determined the rain rate at ground level as an average of the corrected reflectivities exponentially weighted as function of the altitude.

The methods we propose here extend the Germann and Joss's procedure. Basically, for each radar pixel and each elevation angle, we account for the screening effects, the (rain-typed or not) VPR and the characteristics of the radar resolution volume to determine a correction factor for the transformation of the measured reflectivity at the considered altitude to its counterpart at ground level. A simplified expression of the correction factor for a given resolution volume may be written as (Pellarin et al. 2002):

$$CF = K \iint_{\theta,\phi} I(r,\theta,\phi) f^4(\theta,\phi) \, \overline{z(r\cos\theta)} \sin\theta d\theta d\phi \qquad (2.9)$$

where (r,θ,ϕ) are spherical coordinates relative to the radar location, K is a constant depending on the 3-dB beamwidth and $f^4(\theta,\phi)$ the two-way normalized power-gain function of the radar antenna. The function $I(r,\theta,\phi)$ represents the power losses due to the screening effects at the considered range as function of the azimuth and elevation angles. This function is evaluated numerically using the procedure described by Delrieu et al. (1995). The VPR function is derived from one of the estimators proposed in section . The corrected reflectivity (Z_c) is then obtained as function of the measured reflectivity (Z_m) as:

$$Z_c = CF \; Z_m \qquad (2.10)$$

We propose to test in section 3 two methods for estimating the reflectivity close to the ground:
(1) a single corrected reflectivity is used over the vertical by selecting the elevation angle with the correction factor closest to 1 for the subset of elevation angles free of severe ground clutter effects. This subset is determined from the reflectivity coding after ground clutter processing: the pixels for which interpolation is not possible are flagged as missing value. This first method is based on the idea that combination of screening and VPR effects is likely to produce an optimal elevation angle for each point of the radar detection domain. This elevation angle is operating protocol and relief dependent (Pellarin et al. 2002), it may also be weather dependent with the influence of the VPR.
(2) a weighted average of the corrected reflectivities observed over the vertical for the subset of elevation angles free of ground clutter is used. We propose the following formulation for the weights $\{w_i, i = 1, N_e\}$ where N_e is the number of elevation angles available:

$$w_i = \left(1 / Max(CF_i, 1/CF_i)\right)^2 \qquad (2.11)$$

where Max is the function "Maximum value of" and CF_i is the correction factor relative to the ith elevation angle. This formulation gives small weights to elevation angles with correction factors related to high screening and/or VPR effects. It naturally favours elevation angles presenting the best visibility at any location of the radar detection domain. Compared to the previous one, it takes a better advantage of the radar operating protocol in terms of time sampling (several reflectivity measurements may be used instead of a single one for a given 5-min time step).

2.7 A stochastic model of range profiles of raindrop size distribution: application to the sensitivity analysis of attenuation correction schemes to the DSD variability

To obtain robust and accurate rainfall estimates using weather radar, the conversion between the radar reflectivity factor Z (in mm^{6}m^{-3}) and the rainfall intensity R (in mm h^{-1}) is a crucial step. Moreover, in the case of C- or X-band wavelengths, the importance of attenuation affecting the radar signal in rain

has been recognized for a long time (e.g., *Hitschfeld and Bordan*, 1954). The launch of airborne and spaceborne radars, operating at even higher frequencies, stimulated the development of novel methods to correct for the attenuation due to rainfall (e.g., *Marzoug and Amayenc*, 1994). The proposed development of complementary X-band radar networks (e.g. CASA, http://www.casa.umass.edu) is reviving the interest for attenuation correction techniques. Such techniques are based on assumed power-law relations between the integrated radar variables Z, R and k (the one-way specific attenuation, in dB km^{-1}), which are weighted statistical moments of the raindrop size distribution (DSD hereafter). Such power laws have first been empirically established (e.g., *Marshall and Palmer*, 1948). Later they have been cast in a scaling law framework for analyzing DSDs (*Sempere Torres et al.*, 1994). However, all these approaches are based on *deterministic* relations between *stochastic* variables (*Haddad and Rosenfeld*, 1997). To account for the strong variability of rainfall at all scales (e.g., *Jameson and Kostinski*, 2001), the DSD parameters will be considered hereafter as stochastic processes in space.

Adopting a simulation framework allows to produce robust statistics and to perform controlled sensitivity analyses. We present a stochastic model to generate range profiles of DSDs and, as an application, a preliminary investigation of the influence of the stochastic variability of the DSD on the accuracy of attenuation correction techniques. We focus on two aspects: (1) the uncertainty due to the use of deterministic power-law relations between the integral variables Z, R and k; (2) the uncertainty due to rainfall heterogeneity within the radar resolution volume (called non-uniform beam filling or NUBF). The present investigation is focused on incoherent single-frequency non-polarimetric radar systems. However, the simulator also provides a potential test bed for multi-parameter attenuation correction techniques (e.g., *Testud et al.*, 2000).

2.7.1 DSD profile simulator

To simulate DSDs in space with realistic features requires the development of a stochastic DSD model. Once a statistical law has been defined for the DSD, profiles can be produced by means of a stochastic process. To generate realistic profiles, the parameters of the stochastic process are deduced from DSD measurements.

Formulation

To keep the formulation simple and the computation time reasonable, we use an exponential law for the conditional DSD given the parameters N_t (drop concentration) and D_m (mean diameter):

$$N(D|N_t, D_m) = (N_t / D_m)\exp(-D / D_m), \tag{2.12}$$

where D is the diameter, $N(D|N_t, D_m)dD$ represents the number of drops of diameter between D and $D+dD$ per unit volume. Assuming that N_t and D_m follow a bivariate lognormal distribution (*Smith and DeVeaux*, 1994) and defining $N' = \ln N_t$ and $D' = \ln D_m$ yields for the joint probability density function:

$$f(N', D') = N(\mu_{N'}, \mu_{D'}, \sigma_{N'}, \sigma_{D'}, \rho_{N'D'}), \tag{2.13}$$

where N denotes the bivariate normal distribution, $\mu_{N'}$ represents the mean of N', $\sigma_{N'}$ its standard deviation (the same notation is used for D'), and $\rho_{N'D'}$ represents the cross-correlation between N' and D'. We are now able to simulate DSDs at one point. One realization is used as the starting point for generating an entire DSD profile. We assume that the stochastic process governing the DSD

variability along the profile can be modeled as a discrete stationary vector auto-regressive (VAR) process of order 1:

$$X[j+1] = C_1 C_0^{-1} X[j] + E[j+1], \tag{2.14}$$

where

$$X[j] = \begin{bmatrix} N'(j) - \mu_{N'} \\ D'(j) - \mu_{D'} \end{bmatrix}, \qquad E[j+1] = \begin{bmatrix} \varepsilon_{N'}(j+1) \\ \varepsilon_{D'}(j+1) \end{bmatrix},$$

$$C_0 = \begin{bmatrix} \sigma_{N'}^{\ 2} & \sigma_{N'}\sigma_{D'}\rho_{N'D'} \\ \sigma_{N'}\sigma_{D'}\rho_{N'D'} & \sigma_{D'}^{\ 2} \end{bmatrix},$$

$$C_1 = \begin{bmatrix} \sigma_{N'}^{\ 2}\rho_{N'}(1) & \sigma_{N'}\sigma_{D'}\rho_{N'D'}(1) \\ \sigma_{N'}\sigma_{D'}\rho_{N'D'}(1) & \sigma_{D'}^{\ 2}\rho_{D'}(1) \end{bmatrix},$$

j is the distance index, $\rho_{N'}(1)$ represents the auto-correlation at lag 1 (idem for D'), $\rho_{N'D'}(1)$ represents the cross-correlation at lag 1, and $\varepsilon_{N'}$ represents a Gaussian white noise process (idem for D'). Therefore C_0 and C_1 are the covariance matrices at lags 0 and 1. The variances of the white noise processes $\varepsilon_{N'}$ and $\varepsilon_{D'}$ are fixed such that X is a second order stationary process. It must be noted that the auto-correlation function of a first order VAR is exponential:

$$\rho(j\Delta r) = e^{-\alpha j \Delta r}, \tag{2.15}$$

where Δr represents the spatial resolution. Once a DSD profile is generated, the corresponding Z, R and k profiles can be deduced, where it is tacitly assumed that the rainfall field can be regarded as a continuum. The model proposed by Beard (1976) is used to compute the raindrop terminal fall speed and the Mie theory is used to compute the backscattering and extinction cross sections.

Parameterization

The statistical model described above has 9 parameters: 5 for the bivariate lognormal distribution ($\mu_{N'}$, $\sigma_{N'}$, $\mu_{D'}$, $\sigma_{D'}$ and $\rho_{N'D'}$) and 4 more for the VAR process ($\rho_{N'}(1)$, $\rho_{D'}(1)$, $\rho_{N'D'}(1)$, and $\rho_{D'N'}(1)$). Let us first focus on the estimation of the parameters for the lognormal distribution. During the HIRE'98 experiment, DSD measurements have been performed using two optical spectropluviometers, providing DSD time series. As we are interested in the attenuation of the radar signal due to rain, we select a 45-min period during the intense rain event of the 7th of September 1998. Assuming Taylor's hypothesis (*Fabry*, 1996) with a constant velocity of 12.5 m s^{-1} (consistent with the estimate of *Berne et al.* (2004)), we can derive the spatial characteristics of N' and D' we need to parameterize our model. In order to achieve a high resolution of 25 m, the DSD time series has been extracted at a 2 s time step. The parameters N_t and D_m of an exponential law are fitted to the measured diameter spectra, using the third (water content) and sixth (radar reflectivity) order moments of the DSD (*Waldvogel*, 1974). The obtained values are given in Table 2.5. They are assumed to be representative despite the significant sampling error present at such short time steps.

Exponential fits of the auto-correlation functions of N' and D' show that $\rho_{N'}(1) = \rho_{D'}(1)$ is a reasonable assumption. The corresponding scale of fluctuation, defined as (*Vanmarcke*, 1983)

$$\theta = \int_{-\infty}^{+\infty} \rho(r)dr = \frac{2}{\alpha}, \qquad (2.16)$$

is about 4.2 km, a value consistent with the decorrelation distance of R estimated as about 5 km in a previous analysis of the same event (*Berne et al.*, 2004). The cross-correlation between N' and D' appears to be negligible, therefore we assume $\rho_{N'D'} = \rho_{N'D'}(1) = \rho_{D'N'} = \rho_{D'N'}(1) = 0$.

TABLE 2.5 Mean and standard deviation of N_t (m^{-3}), D_m (mm), $N' = \ln N_t$ (-) and $D' = \ln D_m$ (-) deduced from HIRE'98 data at a 2 s time step.

	N_t	D_m	N'	D'
Mean	4025	0.42	8.1	-0.93
Std	2350	0.14	0.41	0.30

As the attenuation effects are more important for X-band wavelengths, we select 3.2 cm as wavelength and the corresponding Mie coefficients have been calculated (at a temperature of 15°C). We simulate DSDs along a range profile of 30 km. As an example of one realization, Fig. 2.10 presents the profiles of the reflectivity factor Z and the corresponding attenuated reflectivity factor Z_a. The mean (over 1000 realizations) of the profile averaged Z, R and k values is 46.5 dBZ, 22.5 mm h^{-1} and 0.46 dB km^{-1}, respectively.

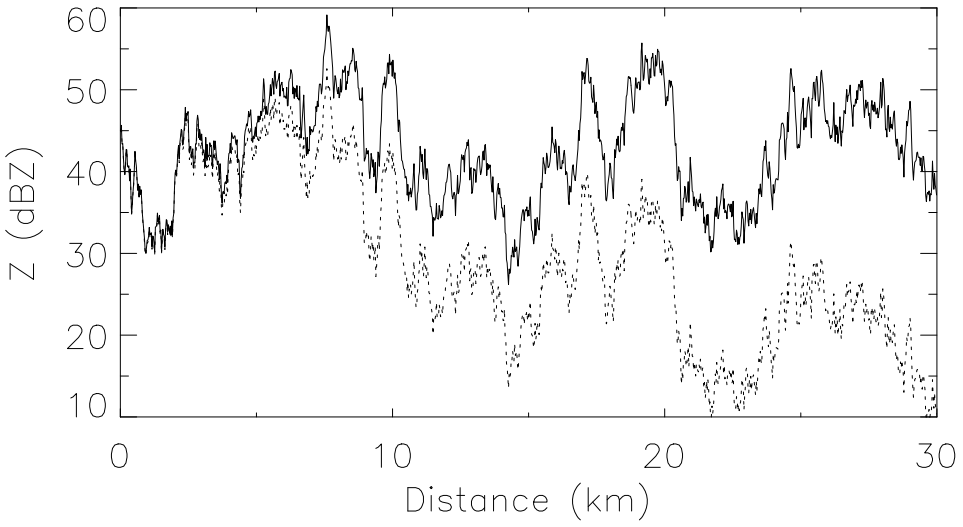


Figure 2.10. Example of Z (solid line) and Z_a (dotted line) profiles generated by the DSD model

2.7.2 Attenuation correction algorithms

The DSD model previously described offers an ideal framework to investigate the uncertainty due to the use of deterministic power-law relations between the integral radar random variables in the attenuation correction. We focus on single frequency non-polarimetric radar systems. We shall use two different types of algorithms to analyze the influence of the variability of the DSD. Assuming $Z = ck^d$, we have

$$A(r) = \frac{Z_a(r)}{Z(r)} = \exp\left[-0.2\ln(10)\int_0^r \left(\frac{Z(s)}{c} \right)^{1/d} ds \right], \tag{2.17}$$

where $A(r)$ is the attenuation factor at the range r ($0 \le A \le 1$). *Hitschfeld and Bordan* (1954) (HB hereafter) proposed an analytical solution to express A as a function of Z_a:

$$Z(r) = \frac{Z_a(r)}{\left[1 - \frac{0.2\ln(10)}{d} \int_0^r (Z_a(s)/c)^{1/d} ds \right]^d}. \tag{2.18}$$

The HB algorithm is a forward algorithm because the integral is between 0 and r. However, the difference in its denominator can be close to 0 and this makes the algorithm highly unstable.

To avoid instability problems, another family of attenuation correction algorithms has been developed. It is based on the knowledge of the PIA at a given range r_0. The reformulation of Eq.(2.18) starting from r_0 and going backward to the radar guarantees the stability of the algorithms. As an example, we use the solution proposed by Marzoug and Amayenc (1994) (MA hereafter):

$$Z(r) = \frac{Z_a(r)}{\left[A(r_0)^{1/d} + \frac{0.2\ln(10)}{d} \int_r^{r_0} (Z_a(s)/c)^{1/d} ds \right]^d}. \tag{2.19}$$

The main drawback of such a backward algorithm is that it requires a reliable estimation of the PIA at a given range.

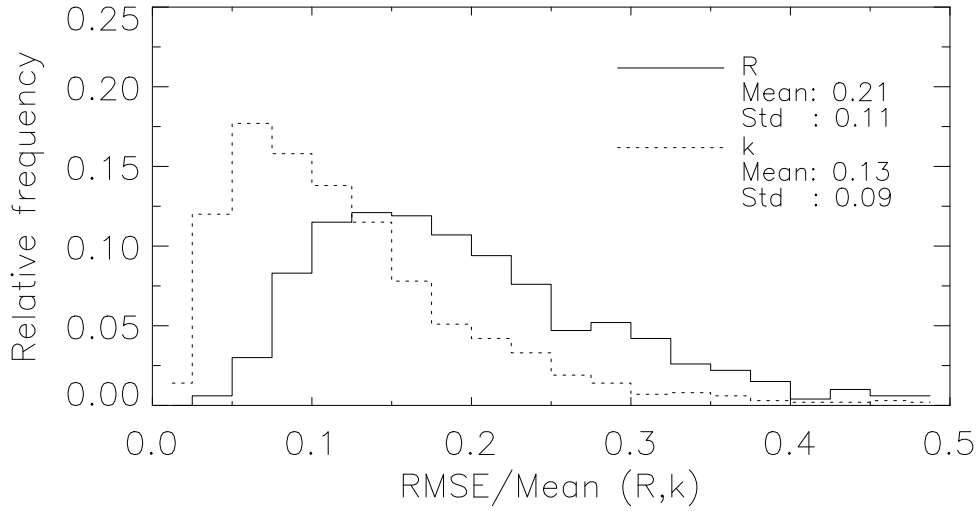


Figure 2.11 Distribution of the RMSE values, normalized by the mean value over the profiles, calculated between the exact R (k respectively) profiles and the R' (k') profiles obtained by converting the exact Z profiles using the fitted Z-R (Z-k) relations.

To study the accuracy of the algorithms, we use a Monte Carlo technique. One thousand profiles of R, Z and k (hence Z_a) are generated. To study the NUBF effect, the high spatial resolution (25 m) profiles are averaged at a lower spatial resolution (250 m), representing the radar sampling resolution. On each

profile a set of power-law relations (*Z-R*, *Z-k*) is fitted separately by means of a non-linear regression technique. It must be noted that they constitute the best possible relations. The exact PIA value is calculated as the difference between the non-attenuated and the attenuated Z profiles. Then the two algorithms are applied using the fitted relations on the 1000 high and low resolution profiles.

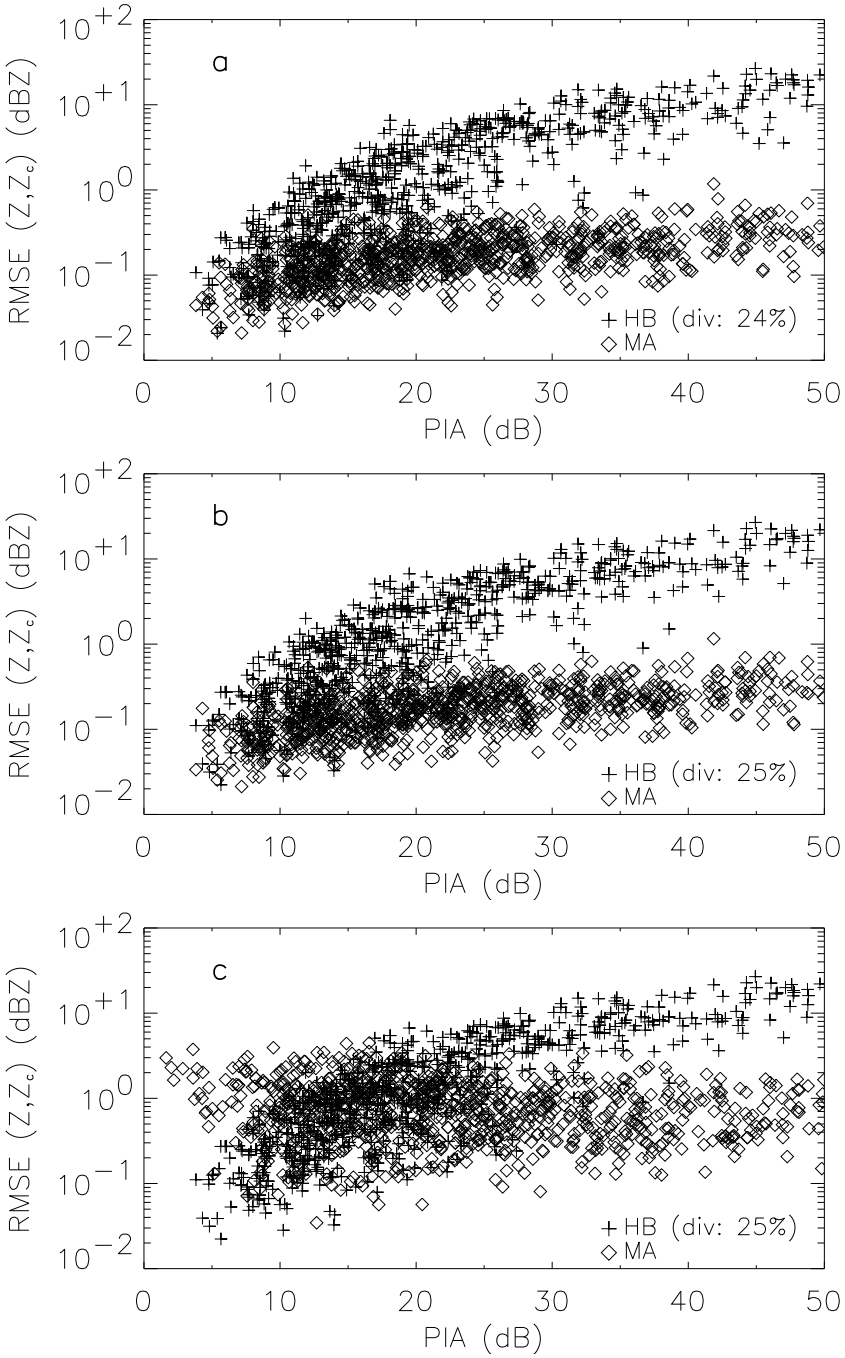


Figure 2-12. RMSE between the exact Z profiles and the Z_c profiles obtained by applying the two attenuation correction algorithms: (a) 25 m resolution, (b) 250 m resolution, and (c) 250 m resolution with uncertain PIA. 'div' indicates the percentage of diverging HB corrections.

The uncertainty due to the use of power-laws for the *Z-R* (*Z-k* respectively) relations, independently of the attenuation effect, is quantified via the RMSE values calculated between the exact *R* (*k*) profiles and the *R'* (*k'*) profiles obtained by transforming the exact *Z* profiles using the fitted *Z-R* (*Z-k*) relations. The distributions of the RMSE values, normalized by the mean value of *R* (*k*), are plotted in Fig. 2.13. It must be noted that the minimum RMSE value, despite the perfect knowledge of *Z* and the use of the best possible power-law relations, is always larger than 0: about 2% of the mean *k* (about 0.01 dB km^{-1}) and about 5% of the mean *R* (about 1 mm h^{-1}). This value provides a lower limit to the uncertainty of radar rainfall estimation due to the *Z-R* conversion.

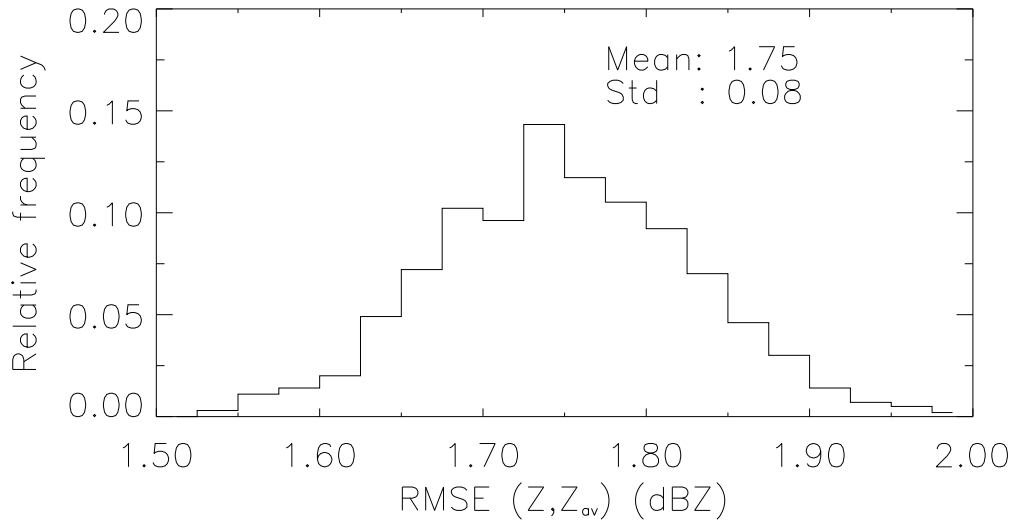


Figure 2-13. Distribution of the RMSE values calculated between the exact Z profiles and the averaged Z profiles at the 25 m resolution.

The influence of the use of a *Z-k* power-law relation on the attenuation correction accuracy is analyzed by means of the RMSE values calculated between the exact *Z* profiles and the Z_c profiles obtained by applying the two attenuation correction algorithms (Fig. 2.12-a). The uncertainty increases when the PIA increases for both algorithms. However, the error remains limited for the MA algorithm ($0.01 \leq$ RMSE ≤ 1 in dBZ) when compared to the error for the HB algorithm ($0.01 \leq$ RMSE ≤ 30 in dBZ, plus diverging profiles in about 1 in 4 cases). It must be noted that none of the algorithms is able to achieve a perfect correction, despite the use of the best power-law relations, the exact high resolution *Z* profiles and the exact PIA in the case of the MA algorithm. This remaining uncertainty is due to the inadequacy of deterministic power-laws to describe the relations between the inherently stochastic DSD weighted moments.

To analyze the impact of NUBF, we first quantify the error due to spatial averaging alone. The averaged *Z* profiles are compared to the high resolution *Z* profiles. Obviously, spatial averaging leads to a significant error, independent of attenuation: the mean RMSE is about 1.75 dBZ (see Fig. 2.13). To quantify the effect of NUBF on the attenuation correction accuracy, the corrected and true *Z* profiles are compared at the low resolution. The RMSE values calculated at the high and low resolutions are found to be similar (see Fig. 2.12-b) for both algorithms. This shows that both attenuation correction schemes do not seem to be sensitive to spatial averaging (from 25 m to 250 m).

To quantify the influence of the possible PIA uncertainty on the performance of the MA algorithm, a Gaussian white noise error (standard deviation of 2.5 dBZ, see *Delrieu et al.*, 1999) has been added to the exact PIA values. The increase of the RMSE values (see Fig. 2.12-c) shows the significant impact of PIA uncertainty on the accuracy of the MA algorithm.

2.8 Conclusions

Several space-time adaptive algorithms were developed in order to improve the radar structured algorithm system (radar SAS) of the Task 15 partners. This radar SAS is dedicated to radar quantitative precipitation estimation with focus on extreme events leading to flash-floods in mountainous regions. The datasets collected during the Bollène 2002 Experiment (French Pilot Site) were used for this purpose.

Firstly, a ground clutter identification technique based on the pulse-to-pulse variability of the reflectivity was adapted in the present configuration. The GC problem is particularly crucial in this case as the result of both (1) the choice of the working wavelength (10 cm) and (2) strong clutter contamination due to the mountainous environment and the presence of many anthropic targets in the Rhône valley, including aircraft lines and interferences with the Nîmes radar. Once identified, ground-cluttered pixels are filled in with a careful horizontal interpolation technique.

Secondly, the question of the automatic separation of rain types within the radar detection domain was addressed. Two rain separation algorithms already proposed in the literature were implemented and tested. The radar sampling properties were found to limit their performance at long ranges. Various methods for estimating the VPR were then reviewed and compared: this includes two variants of the apparent VPR function estimated directly from measured reflectivities and an adaptation of the inverse method of Andrieu and Creutin (1995) to the case of time-varying geographical supports. The latter method is aimed at filtering the radar beam sampling effects in the VPR estimation. In spite of the efficient sorting of the radar pixels subsequent to the rain type separation, the adaptation of the VPR inversion method proved to be difficult as the result of the natural rainfall high variability. Some evidence of over-parameterization (spurious oscillations of the identified VPRs over the vertical) also tends to indicate that the inversion algorithm is not fully appropriate. The concept of coupling the rain partition and the VPR identification was then proposed: basically, implementation of the rain typing algorithms provides a first partition valid at close ranges (typically 60 – 80 km); this preliminary partition is used to identify the convective and stratiform VPRs. In a second step, these identified VPRs are used to improve the rain typing through a similarity criterion between the local VPRs and the identified ones. The full procedure provides acceptable rain typing results as evidenced by visual inspection of the separation results in the horizontal and vertical dimensions. However, a practical limit of validity in range could be estimated at 100 km and the robustness of the algorithm still needs to be improved.

Finally, a method is proposed for calculating the “ground-based” reflectivity prior to the reflectivity-rainfall conversion conditional or not on the rain type. Correction factors accounting for screening and VPR effects are first established for each elevation angle measurements. Then a weighted average of the corrected reflectivity measurements available over the altitude is evaluated, the weights being inversely linked to the correction factors.

In addition, a stochastic model has been developed to simulate realistic spatial profiles of DSDs. It is based on an exponential DSD which two parameters follow a bivariate lognormal distribution. The profiles are produced by means of a first order vector auto-regressive process with given correlation characteristics. Intense rain DSD measurements from the HIRE'98 experiment have been used to parameterize the model. From DSD profiles, it is possible to derive profiles of the variables which are of interest for radar rainfall estimation, i.e. the radar reflectivity factor Z, the rainfall intensity R and the specific one-way attenuation k. Thus a controlled experimental framework has been built to quantify the influence of the stochastic nature of the DSD on the attenuation correction. Focusing on X-band wavelengths, we used a Monte Carlo technique to study the accuracy of two different attenuation correction algorithms. The first (HB algorithm) corresponds to a forward implementation and is known for its instability. The second (MA algorithm) corresponds to a backward implementation and is stable, but requires an additional piece of information which is the PIA at a

certain range from the radar. The PIA uncertainty has a strong influence on the accuracy of the MA algorithm. The non-perfect fit of the power-law relations induces errors, in particular for large PIA, which are small but still significant for the MA algorithm, and which can become huge for the HB algorithm. The results presented correspond to a "best case scenario" and indicate a lower limit for the error remaining after attenuation correction. NUBF, studied by means of spatial averaging, does not seem to have a significant impact on the accuracy of both algorithms. Finally, the proposed model provides a potential test bed to assess the accuracy of recently proposed polarimetric attenuation correction schemes.

3. Implementation and evaluation of the radar SAS in the various pilot sites

3.1 Cévennes-Vivarais Pilot Site

3.1.1 Introduction

The aim of this work is to assess several radar data processing strategies using the datasets collected during the Bollène 2002 Experiment. Assessing the quality of radar QPE is an important subject that received many contributions during the last decades (e.g., the review papers of Wilson and Brandes (1979), Joss and Waldvogel (1990)). Recent contributions (e.g., Ciach and Krajewski 1999; Habib et al. 2004) put emphasis on the rain gauge representativeness problem in such evaluations, especially as far as short integration timesteps are considered. Since our objective is a cross-comparison of several radar data processing strategies, a simple geostatistical approach (Creutin et al. 1988; Delrieu et al. 1988) of the assessment problem is implemented hereafter. The establishment of reference rainfall, based on the dense rain gauge networks of the Cévennes-Vivarais Mediterranean Hydrometeorological Observatory (Fig. 3.1; the French acronym OHMCV will be used hereafter), is presented in section 3.1.2. The various radar processing strategies are described in section 3.1.3 together with their implementation conditions. We basically distinguish two types of radar processing strategies. Firstly, time-adaptive strategies are based on identifications performed over moving time windows (e.g., 5 min for GC identification; one hour for the VPR estimation); the rainfall estimation procedure assumes rainfall homogeneity over the entire radar detection domain with corrections based on a unique VPR and a unique Z-R relationship. Secondly, space-time adaptive strategies additionally involve a regionalization of the processing by means of VPR inference and Z-R relationships conditional on rain types. As a reference approach, the processing strategy operational in the French ARAMIS radar network in 2002 is also considered to evaluate the relative improvement brought by the new concurrent strategies. Section 3.1.4 is devoted to the performance evaluation of the selected radar processing strategies. The conclusions and perspectives are drawn in section 3.1.5.

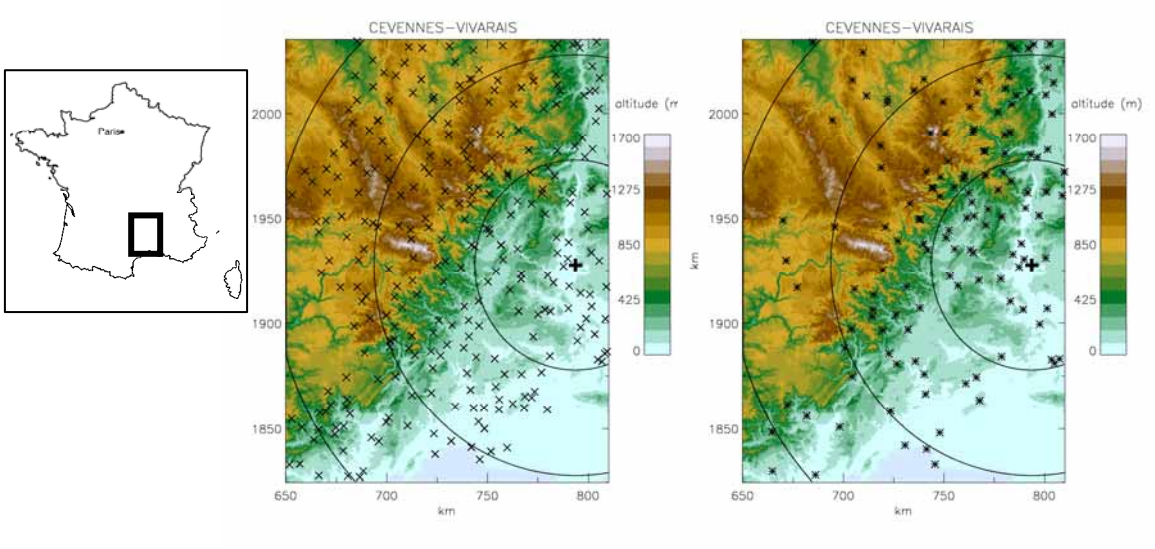


Figure 3.1: Localization of the OHM-CV window in France (top graph); Raingauge networks available at the event timescale (bottom left) and hourly timescale (bottom right) superimposed to the orography of the Cévennes-Vivarais region.

TABLE 3.1: Main characteristics of the selected rain events. The figures given are relative to the rainfall observed at ground level over the OHM-CV observation window, a region of 32000 km^2 where dense rain gauge networks are available.

Date	Localization within the OHMCV window	Spatial extension (surface over which various rain amounts are exceeded)	Maximum rain amount (mm)	Start, end and duration of rain period	Meteorological features
08-09 September 2002	Gard plains	> 200 mm : 5500 km^2 > 400 mm : 1800 km^2	700	1000 UTC 8 September 1400 UTC 9 September 28 hours	Southwestern - southern regime; Stationary V-shaped MCS + Cold front; Flash-floods and catastrophic flooding in the Gard plains
21 October 2002	Ardèche watershed and Rhône valley	> 20mm : 15000 km^2 > 50mm : 1500 km^2	60	1400 UTC 21 October 0000 UTC 22 October 10 hours	Western regime; Cold front with embedded convection
21 November 2002	Ardèche watershed	> 30mm : 10000 km^2 > 50mm : 2000 km^2	100	0000 UTC 21 November 2200 UTC 21 November 22 hours	Western regime; Active cold front with embedded convection
24 November 2002	Cévennes mountains and Ardèche plains	> 50 mm : 12000 km^2 >100 mm : 2000 km^2	150	1000 UTC 23 November 1000 UTC 25 November 48 hours	Southern – southeastern regime ; Widespread rainfall with, at times, rainy bands with varied orientations; Complex dynamics and contrasted vertical development.
10-13 December 2002	Cévennes mountains and Hérault plains	>100 mm : 10000km^2 >200 mm : 1000 km^2	300	0000 UTC 10 December 2000 UTC 12 December 68 hours	Southern regime Stationary rain event with widespread rain of sustained intensities

3.1.2 Reference rainfall

Table 3.1 summarizes the main characteristics of the five rain events selected for this evaluation. These events cover a broad variety of Mediterranean rain systems with a total duration of 176 hours. The 8-9 September 2002 event is particularly exceptional with total rain amounts reaching 700 mm in 28 hours, as the result of a stationary V-shaped mesoscale convective system (MCS) which affected the Gard plains. The 21 October 2002 and 21 November 2002 rain events, with maximum rain accumulations of 60 and 100 mm, respectively, correspond to the passage of cold fronts within westerly meteorological regimes. The 24 November 2002 and 10-13 December 2002 events (maximum rain amounts of 150 and 300 mm, respectively) occurred in southerly meteorological regimes typical of the warm sectors of Mediterranean perturbations; they are characterized by widespread and long lasting rainfall with embedded convection triggered by the orography. The rainfall observation system available for the evaluation of the Bollène-2002 radar datasets is presented in Fig. 3.1. For this region of 200 x 160 km², two networks of about 500 daily rain gauges (Fig. 3.1a; density of about 1 rain gauge per 64 km²) and 160 hourly rain gauges (Fig. 1b; density of about 200 km^{-2}) are available. Note that the raingauge networks are operated by three different weather and hydrological operational services (Météo France, Service de Prévision des Crues du Grand Delta and Electricité de France) with diverse metrological objectives and practices. Therefore an important issue for OHMCV is to gather and critically analyze such datasets. For this purpose, a geostatistical data quality control technique is implemented at the event time scale. This technique is based on the automatic detection of abnormal differences between rain amounts at neighboring rain gauges using the variogram function. Next, the spatial structure of the raingauge amounts is assessed for various integration time steps. The kriging technique is implemented to establish and select reference rainfall values. Since the aim of the present work is a cross-comparison of various radar processing techniques, we keep the following developments to rather simple issues. The critical problem of establishing a reference rainfall and a radar QPE error model is addressed in a dedicated article (Kirstetter et al. 2008).

Rain gauge data quality control.

Let us recall that the variogram function $\gamma(h)$ (Journel and Huigbreghts 1978) is defined as half the expectation of the squared differences between measurements of a given physical process (here, the rain accumulation G over a given time T) as a function of the interdistance h between the points of observation:

$$\gamma_T(h) = \frac{1}{2} E(G(T, \underline{x}) - G(T, \underline{x} + h))^2 \qquad (3.1)$$

where $\underline{x}$ stands for a given location at ground level. If the physical process of interest is 2nd order stationary (constant expectation and variance, homogeneous covariance function), there exist a simple relationship between the variogram and the covariance function $C(h)$, with $\gamma(h) = C(0) - C(h)$. The advantage of the variogram over the covariance function is that the variogram does not require an evaluation of the process expectation. In the single-realization context (e.g., a rainfall field at the event time scale), the practical inference of the variogram function is usually done by sorting the increments $G(T, \underline{x}_i) - G(T, \underline{x}_j)$ into k classes of inter-distances and by fitting an authorized model over the empirical mean variogram, estimated in each class as half the average value of the squared increments :

$$\gamma_T^*(h_k) = \frac{1}{2N_k} \sum_{\substack{over\ the \\ kth\ class}} \left[\left(G(T, \underline{x}_i) - G(T, \underline{x}_j) \right) \right]^2$$
$$with \quad h_k - \frac{\Delta h}{2} \le \left\| \underline{x}_i - \underline{x}_j \right\| < h_k + \frac{\Delta h}{2} \tag{3.2}$$

where N_k is the number of pairs in the kth class and Δh the class interval which may eventually vary as function of h. The OHMCV quality-control technique considers the distribution of the squared increments in each class of distances. For each class, the upper tail of the distribution (e.g. above the 95% quantile) is screened and the corresponding rain gauge stations are sorted according to the number of occurrences in the different classes. This leads to a series of "suspect" stations that are critically analysed in a second step.

Figure 3.2 gives the example of the 8-9 September 2002 rain event. Note that the technique is applied at the event time scale by grouping both the daily and the hourly rain gauge networks. The map displayed in Fig. 3.2a was obtained by kriging the raw rain gauge values with the corresponding variogram function. Fig. 3.2b shows the scattergram of the squared increments, the delimitation of the classes of inter-distances, the mean empirical variogram together with the spherical model fitted. The 95% quantiles of the distributions of the squared increments are also displayed as the horizontal dashed lines for each class. Note that the vertical scale is truncated in order to allow a correct visualisation of the mean variograms. The observed range of squared increment values covers about three times the displayed vertical scale as shown in Figs. 3.2c-e. These figures provide illustrations of the quality-control technique for three "suspect" stations by highlighting their contributions (squares) to the variogram scattergraph. The case of the Sommières rain gauge (Fig. 3.2c) is unambiguous with a rain amount of 20 mm while its neighbours indicate values about 10 times greater (between 200 and 220 mm). The case of the Colognac rain gauge (Fig. 3.2d) is less trivial since a value of 165 mm is observed in a region exhibiting a marked East-West gradient with values comprised between 200 and 695 mm within a range of 15 km around the Colognac station. The rain amounts at the two closest rain gauges (less than 5 km) are 288 and 313 mm. A detailed inspection of the Colognac hyetograph at the hourly time step evidenced a period of missing data in the course of the event which was found to explain the observed underestimation. The case of the Anduze rain gauge station (Fig. 3.2e) is an interesting counter-example: "anomalous" differences are observed between this station and its entire neighbourhood. The maximum reported value during the 8-9 September 2002 event (695 mm in 28 hours) was actually observed there. This value exceeds the amounts observed in the neighbourhood (588, 572, 550 mm…) by about 100 mm but this can hardly be considered as unrealistic. This example shows that the proposed method cannot be automated and that the case of each station identified as suspect needs to be considered with care.

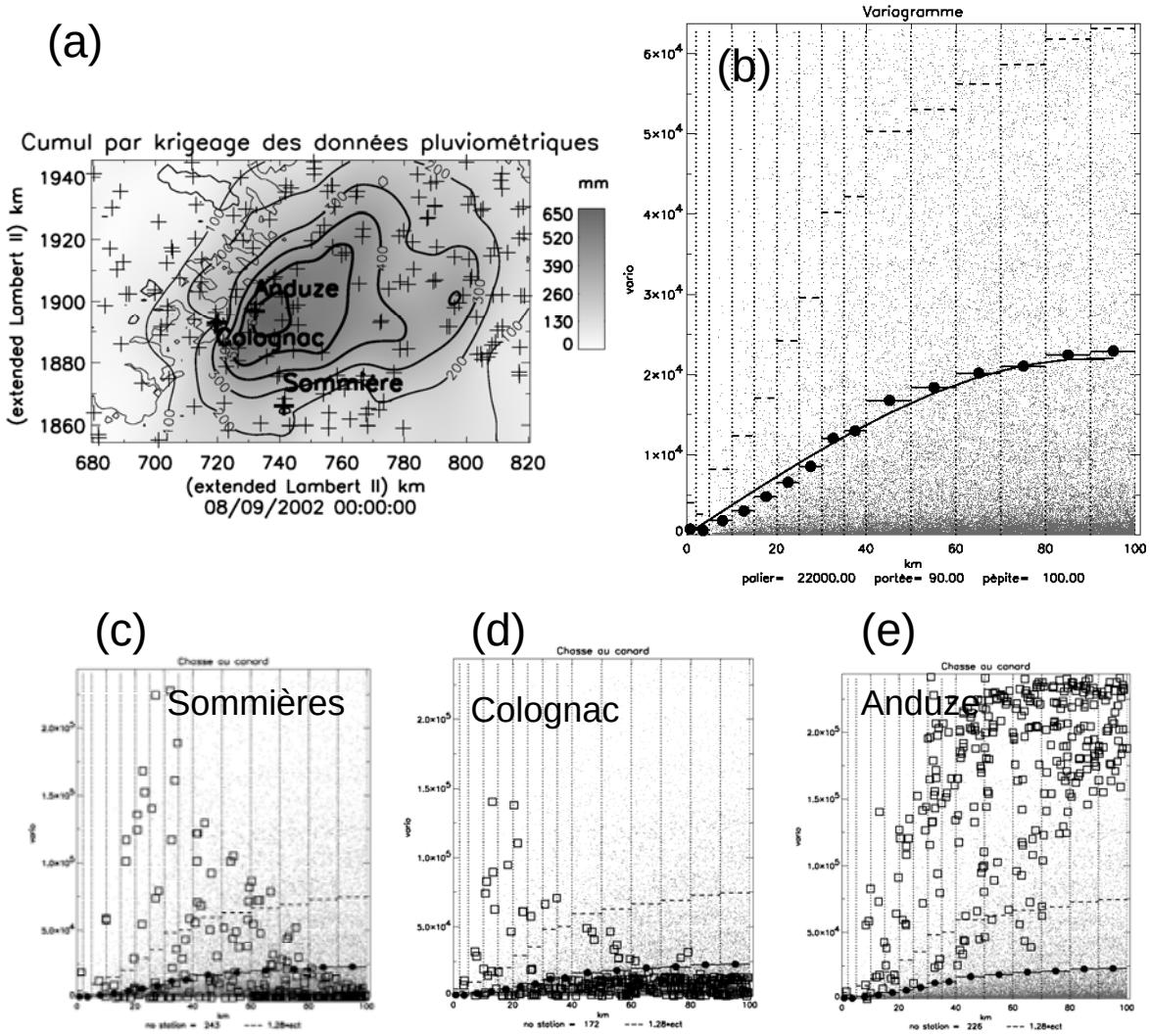


Figure 3.2: Illustration of the quality-control technique of rain gauge data at the event timestep for the rain event of 8-9 September 2002. a – Initial rainfall map obtained over a sub-window centred on the rain event by kriging the raw rain gauge values; b – Scattergraph of the squared differences as function of range (small points) together with the mean variogram (black dots), the spherical model fitted (continuous line) and the 95% quantiles (horizontal dotted lines) of the distribution of the squared increments. c, d, e – Examples of individual contributions (squares) of three "suspect" raingauge stations to the variogram scattergraph (see text for details).

Rainfall spatial structure and mapping using the rain gauge datasets

Table 3.2 lists the parameters of the spherical models that were fitted to the empirical variograms at the event and hourly timescales. Let us recall that the spherical model expression is given by:

$$\begin{aligned} &\gamma(h) = 0 \\ &\gamma(h) = \delta + (\alpha - \delta)\left(\frac{3}{2}\frac{h}{\beta} - \frac{1}{2}\left(\frac{h}{\beta}\right)^3\right) && \text{for } 0 < h \le \beta \\ &\gamma(h) = \alpha && \text{for } h > \beta \end{aligned} \qquad (3.3)$$

where the three parameters are termed as the nugget (δ), the sill (α) and the range (β) values hereafter. The spherical model is suited when the empirical variogram effectively presents a sill, theoretically equal to the field variance, beyond the range value which corresponds to the mean decorrelation distance of the measurements. The nugget value allows description of a possible discontinuity of the variogram at the origin which may be due to (1) the process variability at scales poorly resolved by the observation network and/or to (2) measurement errors.

The variograms at the event timescale were established for the two main directions of anisotropy since elongated rainfall patterns are generally observed for such time steps with a main axis parallel to the Cévennes mountain ridge (roughly 30°-North). Except for the mesoscale convective system of 8-9 September 2002, the orographic influence is clear with range values varying from 90 to 115 km for the main axis and from 35 to 85 km for the secondary axis. The sill values are indicators of the rain field variability which covers 2 orders of magnitude over the five rain events. The nugget values are equal to zero, an indication of (1) the satisfactory sampling of the rain fields by the rain gauge network at the considered time steps and of (2) the efficiency of the quality control procedure.

At the hourly time step, the variograms were inferred by grouping in a single experimental variogram the hourly squared increments observed during the course of the event. These mean variograms are interesting to evidence the relative "power" of the various rain events. Note that for such a multi-realization context, a more rigorous processing should involve a normalization of the squared increments by the variance of each hourly field to derive a normalized variogram (Lebel et al. 1987). This normalization is particularly important if one wants to make accurate evaluations of the kriging estimation variances. Such refinements are detailed in Kirstetter et al. (2008) while more qualitative illustrations are provided hereafter. Hourly rain patterns may present significant anisotropy, however the preferential directions are linked to meteorological features (e.g. fronts) rather than to the relief. They may subsequently significantly vary during the course of individual events. Therefore, isotropic mean variograms were established to characterize the rain field structure at the hourly timestep. Table 3.2 shows that the hourly range values are much shorter (25 - 45 km) than at the event time scale, indicating a reduced spatial representativeness of rain measurements. In terms of variability, it is noticeable that the convective events (e.g. 8-9 September 2002) present much higher sill values at the hourly time step compared to widespread events (e.g. 10-13 December 2002). Note also that some non null nugget values, limited to about 10% of the sill values, are observed for some of the rain events. This tends to show that the overall spatial consistency of the hourly rain amounts is relatively satisfactory, although it is less good than at the event time scale.

Once the spatial rainfall structure is characterized, the estimation of the rain fields can be performed using the kriging method. This method uses a linear estimator for evaluating the rain amount over a given geographical support d_0 which may represent either a point x_0 or a domain D (e.g., a hydrologic watershed):

$$G^*(T, d_0) = \sum_i \lambda^i G(T, \underline{x_j}) \tag{3.4}$$

The kriging estimator is forced to be unbiased and to minimize the estimation variance. The estimation variance is a by-product of the interpolation technique which allows assessment of the estimation quality as function of the spatial structure of the rain field and the relative position of the rain gauge network with respect to the geographical support of interest. Its general expression is:

$$Var(G^*(T, d_0) - G(T, d_0)) = -\sum_{i=0}^{n}\sum_{j=0}^{n} \lambda^i \lambda^j \gamma_{ij} \tag{3.5}$$

where n refers to the number of rain gauges used in the estimation and the subscript 0 refers to the geographical support d_0 of the estimation. In case of estimation at a point $\underline{x_0}$, (3.5) yields:

$$Var(G^*(T, \underline{x_0}) - G(T, \underline{x_0}) = 2\sum_{j=1}^{n} \lambda^j \gamma_{0j} - \sum_{i=1}^{n}\sum_{j=1}^{n} \lambda^i \lambda^j \gamma_{ij} \tag{3.6}$$

As an illustration, Fig. 3.3 presents the maps of the point estimation standard deviation at the centre of the radar Cartesian meshes of 1 km² for the rain event of 8-9 September 2002 for the hourly and event time steps. The quality of the reference rainfall varies a lot over the OHMCV window as a result of the uneven spatial repartition of the raingauges. The western and southern parts of the domain are rather poorly covered especially at the hourly time step. For the purpose of this article, we have chosen to consider the kriging point estimates at the centre of the radar meshes containing a raingauge value as the set of reference values. An alternative to this would be to consider an estimation variance threshold to define such reference domains. This would not add a lot of information due to the spatial correlation of the reference domains thus obtained. The reference values are actually very similar to the point raingauge measurements in case of kriging with a 0-nugget variogram. The reference values would become increasingly smooth with the increase of the nugget effect to reach local or field mean values in case of pure nugget effect. As shown in Table 3.2, in our case the nugget values are null for the event time step and remain limited to a maximum value of about 10 % for the hourly time step.

TABLE 3.2: Parameters of the spherical models fitted on the experimental variograms at the event and hourly timescales. At the event timescale, the variograms are established for the two main directions of anisotropy of the rain field, determined with the radar rainfield at the event timestep (direction 2 is orthogonal to direction 1). At the hourly timescale, a mean variogram is built by grouping all the increments at the various timesteps into a single scattergraph. The nugget value is expressed both in natural units (mm²) and in percentage of the sill value in parenthesis.

	Event timescale				Hourly timescale		
Rain event	Anisotropy	Nugget value (mm^2)	Range value (km)	Sill value (mm^2)	Nugget value (mm^2)	Range value (km)	Sill value (mm^2)
8-9 Sept. 2002	direction 1	0	50	$2.3x10^4$	0 (0)	33	270.0
	direction 2	0	35	$2.3x10^4$			
21 Oct. 2002	direction 1	0	100	$2.5x10^2$	2.0 (8.7)	42	23.0
	direction 2	0	35	$2.5x10^2$			
21 Nov. 2002	direction 1	0	90	$3.7x10^2$	0 (0)	35	16.0
	direction 2	0	60	$4.2x10^2$			
24 Nov. 2002	direction 1	0	100	$9x10^2$	2.0 (12.5)	45	17.0
	direction 2	0	50	$1.6x10^3$			
10-13 Dec. 2002	direction 1	0	100	$4.1x10^3$	0.1 (1.9)	31	5.3
	direction 2	0	40	$4.1x10^3$			

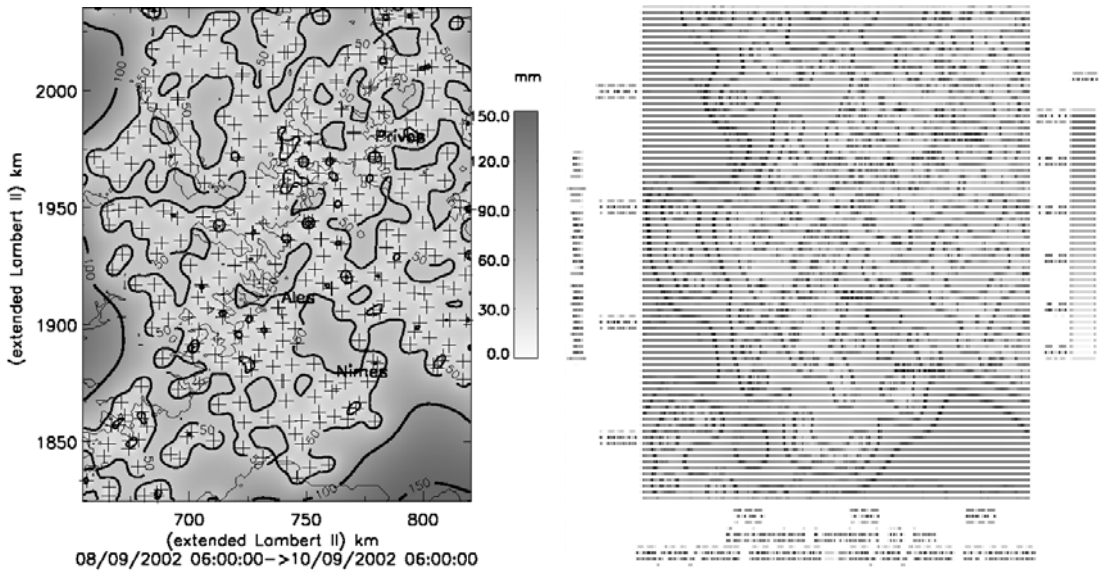


Figure 3.3: Maps of the point estimation standard deviation (mm) of the reference rainfall derived from the OHM-CV raingauge networks for the event of 8-9 September 2002 at the event (left) and hourly (right) time steps.

3.1.3 Radar data processing strategies

In this section, the implemented radar data processing strategies are described. These include the approach that was operational in 2002 (OPER 2002), two time-adaptive strategies (T-AD1, T-AD2) and four space-time adaptive strategies (ST-AD1, ST-AD2, ST-AD3, ST-AD4). These strategies share the following characteristics:

- Except OPER2002, reflectivity correction factors are evaluated for each elevation angle accounting for the screening effects, the VPR function and the radar antenna characteristics using equation ;
- The radar hydrological products (rain-rate fields) are established over Cartesian meshes of 1 km² with a basic time resolution of 5 min;

Rain gauge data are strictly reserved for the evaluation of the radar QPE products (no radar-raingauge merging). The assessment procedure proposed in section 3.1.4 is hence fully objective.

Processing strategy operational in 2002 (OPER2002)

This approach is considered to evaluate the eventual improvements brought by the new concurrent strategies. Its main features are the following. An adaptive ground clutter identification method based on the pulse-to-pulse variability of the reflectivity was already implemented at that time by Météo-France. Compared to the new method proposed in section 2.2, this procedure used an analogic system (rather than a numerical one) and the gradient criterion (*MaxAMD*) used to better process ground clutter edge effects was not employed. In addition, an empirical relationship was used (instead of the interpolation scheme) to "attenuate" the ground-cluttered reflectivity as function of the pulse-to-pulse variability criterion. Screening and VPR corrections were not applied and the compositing procedure to establish the 2D hydrological product from the 3D volume data used the reflectivity measurements at the three elevation angles of 0.8, 1.2 and 1.8° with a fixed range-dependant strategy: the 1.8° measurements were used in the [0, 35 km] range, the 1.2° measurements in the [35, 75 km] range and

the 0.8° measurements for ranges greater than 75 km, regardless the intervening relief. Finally, the $Z = 200R^{1.6}$ relationship was used for the reflectivity – rain rate conversion.

Time-adaptive radar processing strategies

Two variants, rather similar to the radar processing strategies presently operational in the Swiss and French radar networks (Germann et al. 2006; Tabary 2007; Tabary et al. 2007), are proposed:

- T-AD1. The GC identification and correction technique is the one proposed in section 2.2. A single VPR (termed as "global" VPR hereafter) is estimated for the radar detection domain using a moving time window of one hour with a reshuffling period of 5 min. The VPR function is estimated by averaging measured reflectivity values close to the radar site. This apparent VPR is evaluated with the second formulation of (2.6) which accounts for the radar beam weighting function. Regarding rainfall estimation, the reflectivity extrapolated at ground level is a weighted average of the corrected reflectivities over the vertical, the weights depending on the screening and VPR correction factors following (2.11). A unique Z-R relationship ($Z = 200R^{1.6}$) is used for the reflectivity-rain rate conversion over the radar detection domain.
- T-AD2. It differs from T-AD1 by the choice of the Z-R relationship ($Z = 300R^{1.4}$) used in the NEXRAD radar network for convective rainfall.

Space-time adaptive strategies

We consider the following four strategies:

- ST-AD1. Compared to T-AD1, the rain typing algorithm is implemented and the VPR functions for the convective and stratiform regions are derived from the inverse approach. The inverse VPRs are estimated using measurements taken within the 120-km radar range. The global inverse VPR was preferred to the inverse VPR determined specifically for undetermined pixels (see the implementation section below). Like T-AD1, ST-AD1 T-AD1, ST-AD1 utilizes a single Z-R relationship: $Z = 200R^{1.6}$.
- ST-AD2. It differs from ST-AD1 by the choice of the Z-R relationship: $Z = 300R^{1.4}$
- ST-AD3. With respect to ST-AD1 and ST-AD2, we make now a simultaneous use of the two Z-R relationships: (1) $Z = 200R^{1.6}$ for both the stratiform and undetermined pixels; (2) $Z = 300R^{1.4}$ for the convective pixels.
- ST-AD4. We step back in the algorithms' complexity: this strategy is similar to ST-AD3 except that we are considering the apparent VPRs (convective, stratiform and global) derived from the second formulation of (2.6) instead of the inverse VPRs.

Several other algorithm combinations could have been implemented. With the selection proposed above, we focus on the sensitivity of:

- the OPER2002 and new GC processing algorithms
- the method for estimating the reflectivity close to the ground: single value for a fixed elevation angle (OPER2002) *versus* weighted average over the vertical (all the time and space-time adaptive strategies proposed).
- the "partial" regionalisation, including rain typing and VPR corrections: ST-AD1 *versus* T-AD1, ST-AD2 *versus* T-AD2.
- the choice of the Z-R relationship: convective (T-AD2, ST-AD2) *versus* widespread rainfall (T-AD1, ST-AD1) relationships
- the "full" regionalisation, including rain typing, VPR and Z-R relationship conditional on rain types: ST-AD3 versus ST-AD1 and ST-AD2.
- the VPR estimation method: apparent (ST-AD4) *versus* inverse VPRs (ST-AD3). Besides the estimation method itself, this test also addresses the influence of the domain over which the VPRs are evaluated (60 km and 120 km radar range respectively).

Implementation

The Bollène radar parameters and operating protocol are described in section 2.1. We firstly address hereafter the question of the stability of the radar signal, a necessary (though insufficient) condition for radar QPE (Joss and Waldvogel 1990). Note that the electronic radar calibration is established automatically each day by Météo-France for a number of radar parameters (transmitted power, receiver rating curve…). Following Rinehart (1978), Delrieu et al. (1995) and Andrieu et al. (1997), we tested here the simple idea of checking the radar stability with an external target provided by ground clutter. The stability check region was defined using a reflectivity threshold of 45 dBZ, *MAD* values less than 2 dBZ and range between 10 and 50 km. This ensures strong reflections with little variation from pulse to pulse and no saturation of the receiver. The resulting region is composed of about 4000 1-km² pixels taken at several low elevation angles. Table 3.3 shows the mean values of the reference target evaluated for the five selected rain events: they exhibit a range of variation of about 0.5 dB. This suggests a very good level of stability of the transmitter-receiver system during the Bollène-2002 Experiment.

TABLE 3.3: Mean value of the reference ground clutter target used to test radar calibration stability.

Rainfall event	Mean reflectivity value (dBZ)
8-9 September 2002	57.3
21 October 2002	57.0
21 November 2002	57.4
24 November 2002	57.4
10-12 December 2002	57.0

The screening effects (Fig. 3.4) were determined following the geometrical procedure proposed by Delrieu et al. (1995). Let us recall that this procedure uses a digitized terrain model (DTM) with a space resolution of 75 m here. The radar wave propagation in the atmosphere is assumed to be described by the 4/3 Earth radius model (Doviak and Zrnic 1993). The geometrical calculation considers a Gaussian model for the normalized power gain function truncated for an angle value equal to two times the 3 dB beamwidth. This threshold is required to correctly represent ground clutter due to mountain targets. The screening factors are expressed in terms of the correction factor (in dB value) that should be added to the reflectivity in dBZ if the screening effect was the only source of heterogeneity in the radar beam filling (e.g., a half-screened beam would require a 3 dB additive correction). Additive screening factors in the range of 2 to 10 dB are observed over most of the north-east part of the OHM-CV window for the 0.4° elevation angle, while the maximum screening factor is 1.8 dB for the 1.2° elevation angle. The higher elevation angles are free of screening effects.

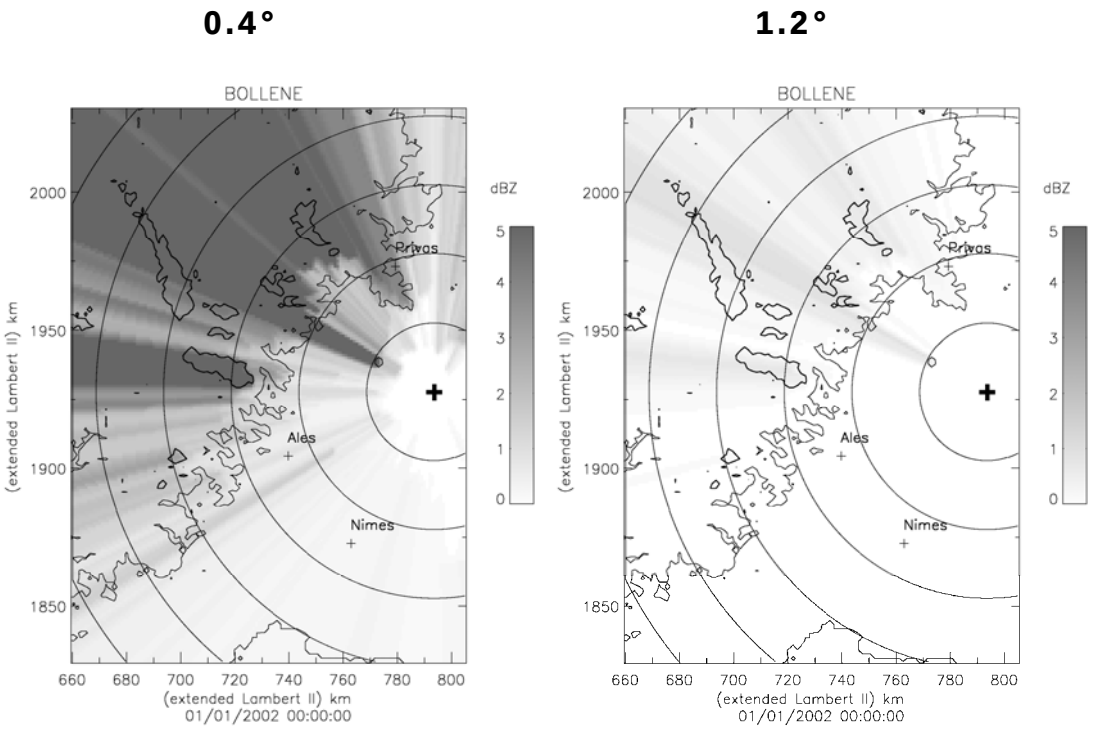


Figure 3.4: Screening factors of the Bollène radar estimated using a digital terrain model for two low elevation angles (0.4 and 1.2°). The factors are expressed in dB to be added to the reflectivity value.

An overview of the variability of the identified vertical profiles of refelectivity for various events of the Bollène experiment is given in Fig. 3.5. Let us recall that the VPRs are estimated using a moving time-window of 60 min with a reshuffling period of 5 min. The vertical extension of the 8-9 September 2002 is remarkable both for the convective and stratiform regions: (1) gradient of -5 dB/km between 3 and 4 km asl and -3 dB/km above 4 km asl for the convective VPR; (2) bright band altitude of 3.2 km and peak of about 5 dB for the stratiform VPR; gradient of -2 dB/km above 4 km asl. The VPRs decrease much faster for the two other examples, e.g., with a gradient of about 10 dB/km for the convective VPRs above 3 km asl. Note also there is rather systematically a slope break 1 km above the bright band: this altitude probably corresponds to the limit between iced and melting hydrometeors. The shapes of the convective and stratiform VPRs are clearly distinct for each single rain event. The global VPR lies between the two; it is sometimes closer to the convective one (e.g. 8-9 September 2002 case, 10-13 December 2002) and sometimes closer to the stratiform one (e.g., 21 November 2002). The VPR estimated for the "undetermined" pixels is close to the global one, however it frequently presents (e.g. 8-9 September 2002) a slight shift just above the reference level ([0, 1 km asl]. This is related to a normalization problem: as long as range increases, there are less reflectivity measurements available in the reference level and expression (2.6) becomes biased. This is why we will be using the global VPR for correcting the undetermined pixels. Two other facts need to be mentioned: (1) the spread of the VPR distributions is rather limited for a given rain event; this means that the time variability of the VPR is relatively low and (2) some erratic VPRs are estimated when insufficient quantity of information is available, especially for the 10-13 December 2002 case. Criteria

are therefore required to appreciate the robustness of a given VPR and define the VPRs that are to be used instead. In the present article, we decided to consider as non robust the VPRs for which at least one point was outside the 10 and 90% quantile intervals of the VPR distributions shown in Fig. 3.5 and to use instead the median typed VPR. This solution is obviously not practicable in real time applications since the VPR time distributions through the entire event are unknown. Other more realistic possibilities could be to use the global VPR when the convective or stratiform VPR are not robust enough, and a climatological VPR when the global VPR is not. However such alternatives tend to "smooth" the impact of the rain separation, our primary interest in this article.

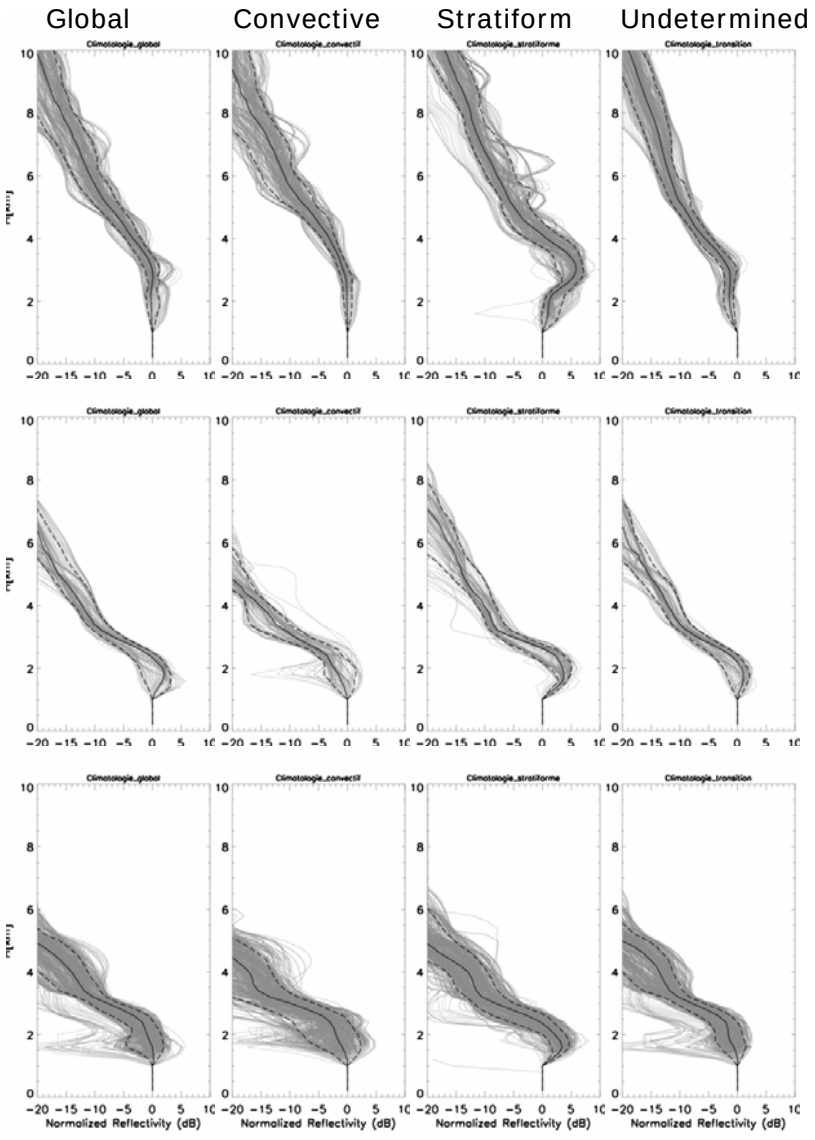


Figure 3.5: Identified VPRs (grey curves) for the 8-9 September 2002 (top graphs), 21 November 2002 (middle graphs) and 10-13 December 2002 rainfall events of the Bollène-2002 Experiment. From left to right: global estimation without rain typing; estimation for the convective, stratiform and undetermined regions. The 10, 50 and 90% quantiles of the distribution are displayed with dotted and continuous black lines.

3.1.4 Assessment of various radar processing strategies

Figure 3.6 presents the radar-raingauge scattergraphs for two methods (T-AD1 and ST-AD3) obtained by grouping the data of all the five rainfall events. We recall that such comparisons are made for the 1-km² radar meshes containing a raingauge station, the reference values being the kriged raingauge rainfall at the center of the mesh. The results displayed correspond to comparison points located within the 100-km radar range. Attention should be focused first on the scattergraph scales with ranges of variation of [0-140 mm h-1] and [0-700 mm] for the hourly and event time steps, respectively. The 8-9 September 2002 rain event has of course a major influence on such scattergraphs and on the criteria that can be estimated to assess the radar-raingauge likeness. We will be using hereafter the mean relative error ($MRE = (\overline{R} - \overline{G}) / \overline{G}$) for the bias assessment and the determination coefficient (square of the linear correlation coefficient) for the scatter assessment. The Nash coefficient ($N = 1 - \overline{(G-R)^2} / \overline{(G-\overline{G})^2}$), classically used in hydrology to assess performance of a given estimator with respect to reference values, will be considered as well for its sensitivity to both bias and scatter. Remember that perfect agreement in terms of bias and scatter (all the points are on the one-to-one line) gives a Nash coefficient of 1 while a value less than 0 is obtained when the estimator provides estimations as poor as the simple average of the reference values.

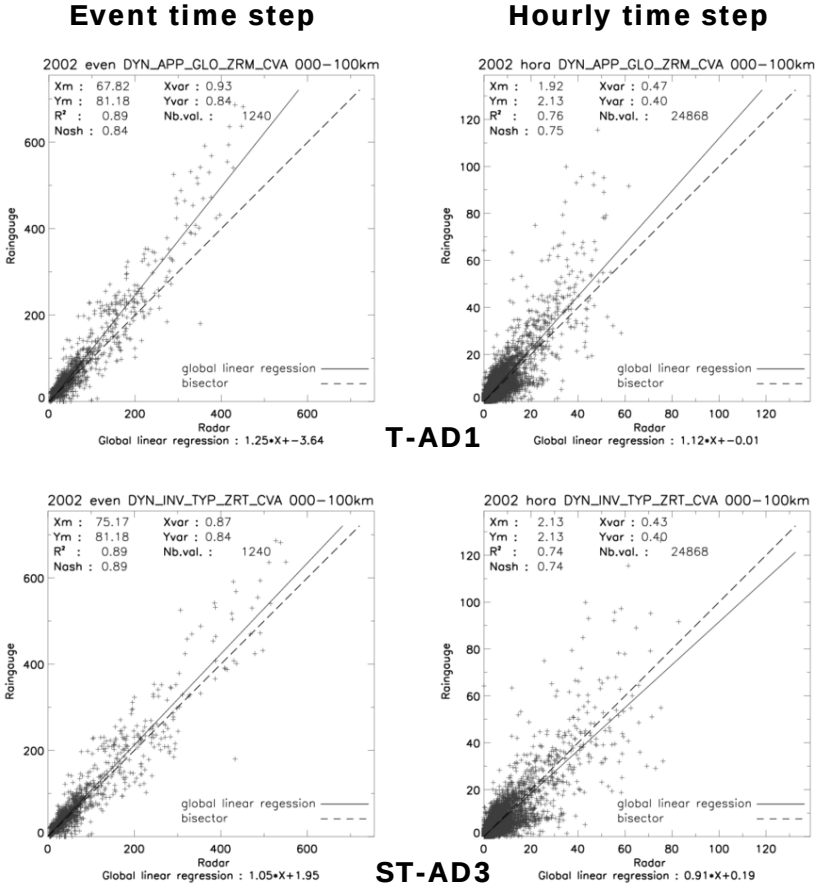


Figure 3.6: Scattergraphs of the radar-raingauge comparison over the set of 5 rain events selected at the event (left) and hourly (right) steps for the T-AD1 and ST-AD3 radar processing strategies.

The overall radar-raingauge agreement shown in Fig. 3.6 is good at the event time scale with Nash coefficient values of 0,84 and 0,89 for the T-AD1 and ST-AD3 strategies respectively. It should be outlined again that the radar estimations are obtained independently from the raingauge measurements (no radar-raingauge merging at any stage of the radar processing) and that the Z-R relationships used are not optimized in any manner with respect to the Mediterranean climatology. The performance of the processing strategy operational in 2002 (OPER2002) was very much affected by residual ground clutter which, by cumulating at the event time scale, led to dramatic over-estimations. The solution of this problem explains a large part of the radar-raingauge scatter reduction between OPER2002 and the new processing strategies: the determination coefficient increases from 0,46 (OPER2002) up to 0,89 (T-AD1 and ST-AD3). Due to the ground clutter influence, the OPER2002 bias (MRE=1.3 % at the event time scale) was actually good for wrong reasons. The bias is increased with MRE values of -16,5% and -7,4% for T-AD1 and ST-AD3 respectively, an indication of a significant radar under-estimation. As expected, the overall radar-raingauge performance drops at the hourly time step with Nash coefficients of 0,75 and 0,74 for the T-AD1 and ST-AD3 strategies, respectively. The scatter is increased (determination coefficients of 0,76 and 0,74) but the bias is less important at the hourly time step with MRE values of -9.8 % and 0 for T-AD1 and ST-AD3 respectively.

A detailed inspection of the assessment criteria for the various processing strategies is proposed below. Besides the results obtained by grouping the five events, we found useful to distinguish the various rain events which correspond to diverse rainfall systems (Table 3.1) typical of the Mediterranean climate. In order to limit the material to be displayed, we made the following groups of events:

- Group 1: 8-9 September 2002 (MCS),
- Group 2: 21 October 2002 and 21 November 2002 (frontal systems),
- Group 3: 24 November 2002 + 10-13 December 2002 (shallow convection triggered by the orography).

The results in terms of *MRE*, determination coefficient and Nash coefficient for the [0-100 km] range are presented in Fig. 3.7 for the event time step. Note that similar trends are observed for the hourly time step; the results for such "hydrological" time steps are discussed in Kirstetter et al. (2008). The most stricking result in the graphs of Fig. 3.7 is that, expect OPER2002, all the tested strategies have quite similar performance in terms of determination coefficient (radar-raingauge scatter). However, the bias criterion exhibits marked variations as function of the processing strategies and the groups of rain events considered. The Nash criterion allows making an interesting synthesis of the radar-raingauge bias and scatter evolution. The following comments can be made:

- Note first that assessment criteria are much better for the 8-9 September 2002 case compared to the events of Groups 2 and 3. This is related to the huge vertical extension of the MCS event and also to the fact it affected principally regions within the 100-km range with a good visibility.
- As already mentioned, OPER2002 is very affected by residual ground clutter effects resulting in low determination coefficients, (comparatively) high positive MRE and negative Nash criterion values. This is particularly true for the events of Groups 2 and 3.
- By implementing the new GC processing strategy, accounting for the global VPR time series for each event and making weighted average combinations of the corrected reflectivities over the vertical, T-AD1 and T-AD2 make clear progress with respect to OPER2002 in terms of determination coefficient and Nash coefficient, especially for the events of Group 2 and 3. However the MRE criterion becomes negative (e.g., -16,6% and -16,7% for T-AD1 and T-AD2, respectively, for the group of 5 events), indicating a significant average radar under-estimation at the event time step (see the comments of Fig. 6 about the evolution of the MRE criterion as function of the time step).
- About the Z-R relationship choice, comparison of the Nash coefficients for the pairs of strategies (T-AD1, T-AD2) and (ST-AD1, ST-AD2) indicates that use of the $Z = 300R^{1.4}$ relationship has a very positive impact for the 8-9 September 2002 case and a very negative one for the events of Groups 2 and 3.

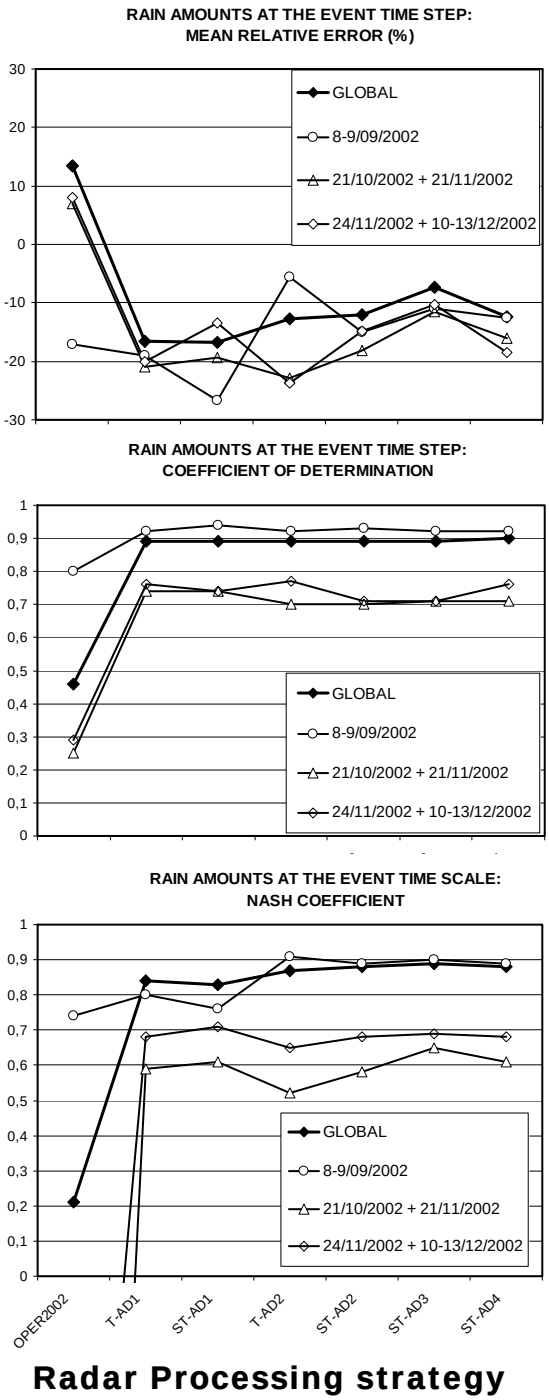


Figure 3.7: Evolution of the assessment criteria at the event time step as function of the radar processing strategy for the [0-100 km] radar range interval: mean relative error (top graph), determination coefficient (middle) and Nash coefficient (bottom).

- About the "partial" regionalisation, comparison of the Nash criterion for (T-AD1, ST-AD1) and for (T-AD2, ST-AD2) indicates a slightly negative impact for the 8-9 September 2002 case and a slightly positive one for the events of Groups 2 and 3
- About the "full" regionalisation, comparison of ST-AD3 with both ST-AD1 and ST-AD2 yields the following comments: the determination coefficient is basically unchanged or even slightly decreased while on the contrary the MRE criterion is very significantly improved (about -7,4 % for the global MRE value). This results in a very slight increase of the global Nash criterion. For each group of events, a positive trend of the regionalisation is observed since the ST-AD3 performance is equivalent to the best one among ST-AD1 and ST-AD2 for Groups 1 and 3. Note even that the ST-AD3 performance overpasses both the ST-AD1 and ST-AD2 ones for Group 2.
- About the VPR estimation method (inverse VPR versus apparent VPR), we note that use of the more sophisticated approach (inverse VPR, ST-AD3) has a slightly detrimental impact in terms of determination coefficient and a positive impact in terms of MRE, which results in a slightly positive impact for the Nash criterion.

An assessment of the spatial performance of the various strategies is proposed hereafter. The various groups of rain events are considered separately since they exhibit specific characteristics in terms of horizontal and vertical variability. Figure 3.8 shows the evolution of the Nash criterion calculated globally for the [0-150 km] range interval and for specific range intervals of [0-50 km], [50-100 km] and [100-150 km]. For the event time step, the corresponding networks (Fig. 3.1) count 356, 74, 175 and 107 raingauges respectively. Note in Fig. 8 that the Nash criteria calculated globally for Groups 1 and 2 are better than those calculate for each class of distances. Such a result may be a surprise for the reader. It is simply related to the spatial variation of the rainfields: an extended spatial domain may lead to an increased rainfall variance and this may impact the assessment criteria (e.g. determination coefficient, Nash criterion) in the way observed. Such an argument does not hold for Group 3 mostly as the result of the more homogeneous spatial distribution of rain amounts. As a complementary support to Fig. 3.8, Fig. 3.9 displays the raingauge and radar maps at the event time step for one event of each group. These figures call for the following comments:

- 8-9 September 2002 case. For this mesoscale convective system, the radar performance is basically good due to its magnitude, vertical extension and localization in a region with good visibility. The Nash criteria are quite similar for both the [0-50 km] and [50-100 km] range intervals. They slightly decrease for ranges greater than 100 km. It is interesting to note that T-AD1 and T-AD2 fail in this region while the space-time adaptive strategies improve performance over OPER2002. Note however that such results are obtained in the margin of the rain event; they may lack of robustness. More importantly, for this event, the factor with major impact is clearly the choice of the Z-R relationship rather than the rain separation and the typed VPR correction. This is consistent with the structure of the event characterized by clusters of very active convective cells remaining almost stationary over the region. The stratiform part of the system (see Fig. 2.2 and 2.4) had probably a lower contribution in terms of rainfall; the high altitude of the bright band (3.2 km) also explains the rather low influence of the stratiform VPR corrections since several elevation angle measurements were available below the bright band over a large part of the affected region.
- Events of Group 2. For these rain events associated to cold front systems (example of the 21 November 2002 in Fig. 3.9), the radar performance is rather good and similar for both the [0-50 km] and [50-100 km] range intervals. It drops very significantly for greater ranges due to the rather limited vertical extension of the rainfall (Fig. 3.5). This is the more convincing case of the interest of space-time adaptive processing in this study with a clear superiority of ST-AD3 over all the concurrent strategies.
- Events of Group 3. For these long-lasting events characterized by shallow convection triggered by the orography, the radar performance is good in the [0-50 km] range interval, rather good in the [50-100 km] range interval and extremely bad at longer ranges. The maps of

the 10-13 December 2002 case (Fig. 3.9) confirm the strong estimation problem we have in the southern part of the OHMCV window for this specific event. This is related to the even lower vertical extension of such rainfall systems compared to Group 2 (Fig. 3.5) and to the fact that they are mostly affecting the mountainous part of the OHMCV window with possible residual GC impact. It is noticeable that ST-AD3 fails close to the radar site while it works quite well at longer ranges while an opposite trend is observed for ST-AD4. This may indicate we are reaching some limits in terms of validity of the rain separation and VPR estimation methods for such rain types with single radar observation.

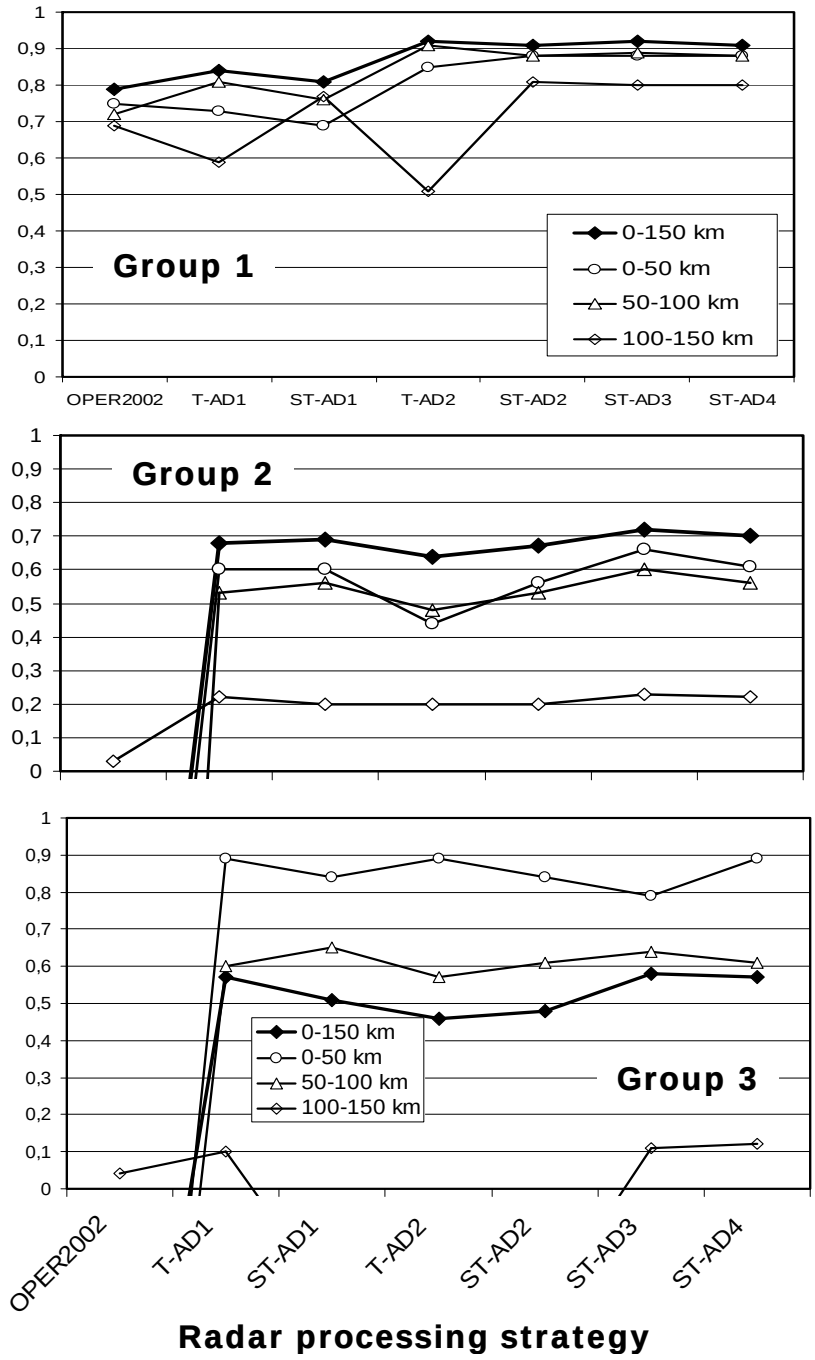


Figure 3.8: Evolution of the Nash coefficient at the event time step as function of the radar processing strategy for various radar range intervals and the three groups of rain events.

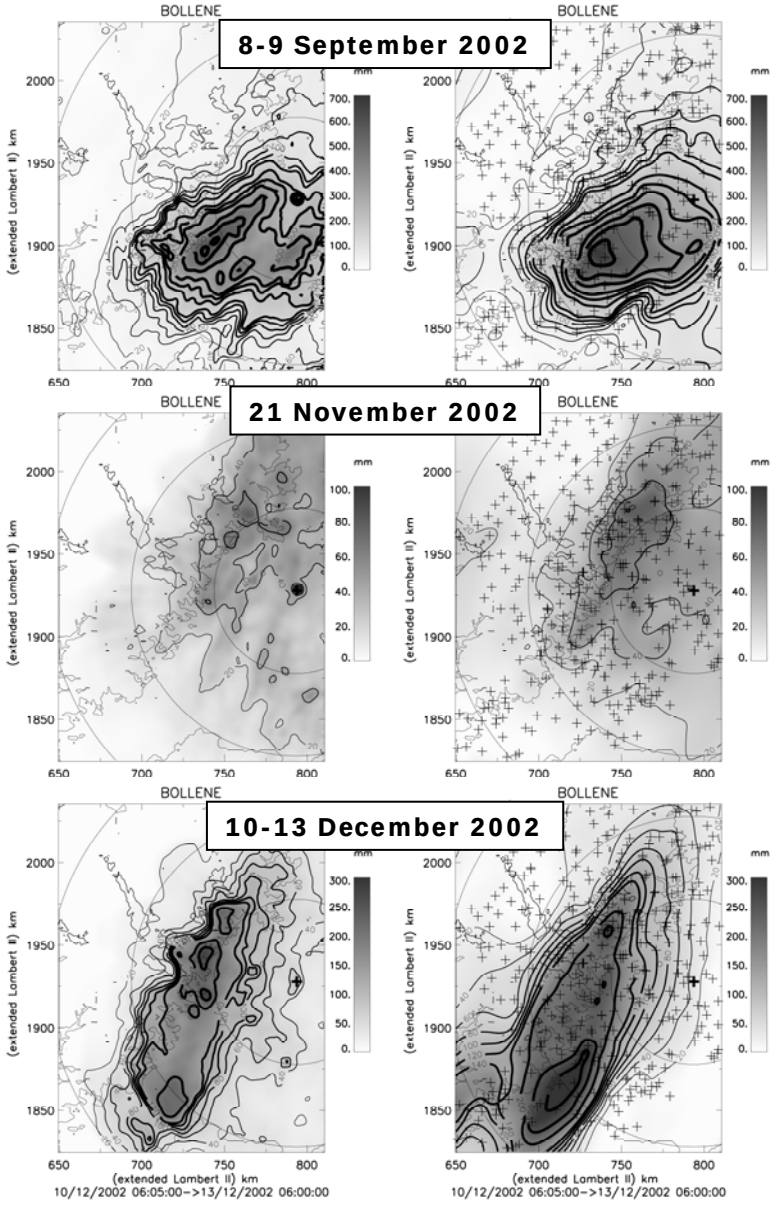


Figure 3.9: Rainfall fields at the event time scale over the OHM-CV window for the rain events of 8-9 September 2002, 21 November 2002 and 10-13 December 2002. The kriging interpolation technique with anisotropic variograms was used to elaborate the raingauge maps (right column). The results of the ST-AD3 radar processing strategy are displayed in the right column with radar range markers of 50 km. Note that the grey scale and the isolines are adapted to the magnitude of each rain event.

3.1.5 Conclusions

This work was aimed at assessing the benefit of space-time adaptive radar processing strategies for quantitative rainfall estimation in mountainous regions. It is based on the Bollène-2002 Experiment which allowed collection of 3D radar data for a series of intense Mediterranean precipitation events. In section 2, several space-time adaptive algorithms were described, including (1) a dynamic ground clutter identification and correction technique based on pulse-to-pulse variability of the reflectivity, (2) a coupled identification of the regions with homogeneous rain types (convective, stratiform) and the corresponding VPRs, (3) a method for estimating rain intensity at ground level from the corrected reflectivities aloft. Several radar processing strategies were defined to assess the new algorithms with respect to reference rainfall data derived from a careful geostatistical analysis of the OHMCV raingauge networks. The basic radar processing strategy was the one operational in 2002: it proved to be dramatically affected by residual ground clutter. Time-adaptive strategies (T-AD1 and T-AD2), similar to the processing strategies presently operational in the French and Swiss radar networks were then considered. They use the new GC processing algorithm, VPR and screening correction based on a single apparent VPR estimated in the vicinity of the radar site, the weighting average of the corrected reflectivities and a single Z-R relationship. In the absence of specific Z-R relationships for the Mediterranean climatology, the two variants T-AD1 and T-AD2 used the classical $Z=200R^{1,6}$ and $Z=300R^{1,4}$ relationships respectively. Several space-time adaptive strategies were also defined: ST-AD1 and ST-AD2 are analogous to T-AD1 and T-AD2 except they use the rain separation algorithm and the corresponding typed VPR estimated using an inverse approach. The two variants utilize a unique Z-R relationship whatever the rain type while ST-AD3, the most complex processing strategy, utilizes $Z=300R^{1,4}$ for conversion in convective rainfall and $Z=200R^{1,6}$ for stratiform and "undetermined" rainfall.

On this basis, examination of the assessment criteria for the Bollène 2002 Experiment shows that:

- the new GC processing algorithm works satisfactorily. This result is important and it was difficult to achieve due to the strong contamination of S-band radar signal in the considered context (mountains, anthropic targets).
- good radar quantitative rainfall estimation is feasible within the 100-km radar range by using well-sited, well-maintained radar systems and sophisticated physically-based radar data processing systems. Performing and checking electronic calibration, determining the radar detection domain, performing an efficient GC processing, "capturing" the vertical structure(s) of reflectivity for the event of interest are the basic ingredients required.
- the Bollène 2002 results show however that the added value of the space-time adaptive processing is not very significant. To be more specific, the radar raingauge scatter quantified by the determination coefficient remains basically unchanged for all the time and space-time adaptive processing strategies. A positive trend is observed however in terms of bias since ST-AD3 presents systematically the best mean relative errors. Since the Z-R relationships are not optimized yet, this result is attributed to an improved processing of the spatial variations of the VPR, mostly for the stratiform pixels. The convective pixels with straight VPRs are probably less sensitive to VPR corrections but, due to the high convective rainrates, they strongly influence the quadratic criteria used (determination coefficient, Nash criterion). The improved performance for the contrasted frontal systems of Group 2 is also encouraging.

Several factors may explain the moderate success of the space-time adaptive strategies and justify future work on this (still new) research subject. Firstly, the limited radar space-time sampling characteristics make the rain type separation and the subsequent VPR inference particularly difficult. The coupled identification approach proposed in section 2.5 is a first trial to accounting for the radar sampling properties. Our next objective is to extend the separation algorithm to the pair of S-band radars available in Bollène and Nîmes: the observation problems evidenced in mountainous regions for the rain events with small vertical extend can only be solved with radar networks. The

generalization of Doppler and polarimetric capabilities in operational networks is also promising for this purpose. Secondly, research effort still needs to be devoted to the critical link between the radar measurables in the atmospheric vertical column and rainfall at ground level. We used here classical Z-R relationships with some success. However, the NEXRAD "convective" Z-R relationship was found to be suited for the deep convection case of the 8-9 September 2002 and not appropriate for the frontal and shallow convective cases. Chapon et al. (2008) started addressing the complex question of the space-time variability of the Z-R relationship in the Cévennes region by using DSD measurements at ground level in conjunction with the 3D radar data. This effort will be amplified with an ambitious experimental program which is being built by the OHMCV research teams within the HyMeX project (http://www.cnrm.meteo.fr/hymex/).

3.2 Adige Pilot Site

3.2.1 Introduction

A different approach to the assessment of radar rainfall estimation uncertainty is proposed in this study. This is based on the direct analysis of the algorithm system used to derive radar rainfall estimates at the ground. Research in the past two decades has pointed out the need to base this estimation problem on the accurate physical understanding of radar measurement processes "by addressing the various sources of error in a painstaking and a meticulous manner" (Zawadzki, 1984; Krajewski and Smith, 2002; Creutin and Borga, 2003; Uijlenhoet et al., 2006). Common to most radar rainfall estimation algorithms is therefore the desire to incorporate more understanding into the algorithmic structure used, as knowledge grows based on experiments, field studies and analysis. The conversion of radar signal into a field of rainfall estimates at the ground therefore results in a complex process consisting of several intermediate steps which require the inclusion of an increasing number of parameters into the algorithm (Fulton et al., 1998; Ciach et al., 1997; Smith et al., 1996; Steiner et al., 1995; Dinku et al., 2002). These parameters may be required to represent the physical or statistical characteristics of the system under study and may have excellent justification. However, it may be difficult to specify a priori the value of some of those parameters. Parameter uncertainty may therefore introduce significant uncertainty into the rainfall estimation at the ground. This uncertainty may be reduced by comparison of radar rainfall estimates with corresponding ground references and identification of 'optimum' parameter sets. However, it is not uncommon that this same parameter set may perform poorly and others may be ranked as optimal for a different set of evaluation data or for a different evaluation period.

The purpose of this work is to investigate the sensitivity of a radar rainfall estimation algorithm to parameter uncertainty and to use this knowledge to outline a feasible methodology for radar rainfall uncertainty estimation. The procedure is based on the Generalized Likelihood Uncertainty Estimation (GLUE) methodology (Beven and Binley, 1992), which transforms the problem of searching for an optimum parameter set into a search for a set of parameter values, which would give reliable rainfall estimates at the ground for a wide range of radar observations. This approach also enables uncertainty limits of the estimated value to be obtained.

These issues will be addressed in the following sections, together with an example evaluation in the Adige Pilot Site. The methodology proposed here is used to analyse the parameter sensitivity for different radar ranges and to derive uncertainty bounds for basin-averaged areal rainfall estimates. The report is organized as follows: in section 3.2.2 we present the study area and data available. In section 3.2.3 we outline the algorithm used for radar rainfall estimation and its application to the study area. In section 3.2.4 we describe the methodology for quantification of radar rainfall uncertainty and the example application. We close in section 3.2.5 with general conclusions and suggestions on future research and development.

3.2.2 Study area and data resources

The data used in this study were collected by the C-band Doppler radar located on the Monte Grande hill in northern Italy, close to Venice and Padua (Figure 3.10). Technical characteristics of the radar are reported in Table 3.4. The region covered by the radar ranges from the plains to high elevation mountains with altitude exceeding 3000 m asl (eastern Italian Alps). The raingauge network includes 105 stations; of these, 32 are placed at ranges below 40 km, 55 stations are installed at ranges intermediate between 40 and 80 km, and 18 stations are comprised between 80 and 120 km from the radar site. These rain gauges are teleconnected with the centre managing the radar, which reduces the possibility of time-synchronisation errors between the different data sources. A standard quality control on rain gauge data is performed by the Meteorological Center of the Regional Agency for Environmental Protection and Prevention of Veneto (ARPAV), which manages both the radar system and the rain gauge network. We further refined the quality control by using daily data from other raingauge networks, which include those operated by Meteotrentino (Provincia Autonoma di Trento) and by Ufficio Idrografico di Bolzano (Provincia Autonoma di Bolzano).

The study area comprises the Alpone river basin at Monteforte (hereafter called Alpone), draining 77 km², and the Posina river basin with outlet at Stancari (hereafter called Posina), draining 116 km² (Figure 3.10). Alpone and Posina are located at 38 km and 60 km basin-to-radar distances, respectively. Hourly air temperature data from twelve stations, located around the basins and at altitudes ranging from 100 to 2500 m a.s.l., were also used in this study to estimate the 0°C isotherm.
The investigation is performed for six storm events, which are summarised in Table 3.5. The selected events are representative of a typical meteorological situation, characterised by cyclogenesis in the Lion Gulf or surrounding regions, which often establishes over the western Mediterranean in autumnal months. Cold fronts generated by this kind of cyclonic circulation bring humid warm air from the South and/or the South-West, developing pre-frontal convective clouds and frontal stratified clouds to impact the northern rugged coastline. Spatial structure of these storms was previously analysed by Bacchi et al. (1996). Five of these storms caused the largest runoff events during the period 1986-1997 over Alpone and Posina. The moderate storm event of SEP94 was selected due to its significant spatial intermittency of hourly rainfall accumulations.

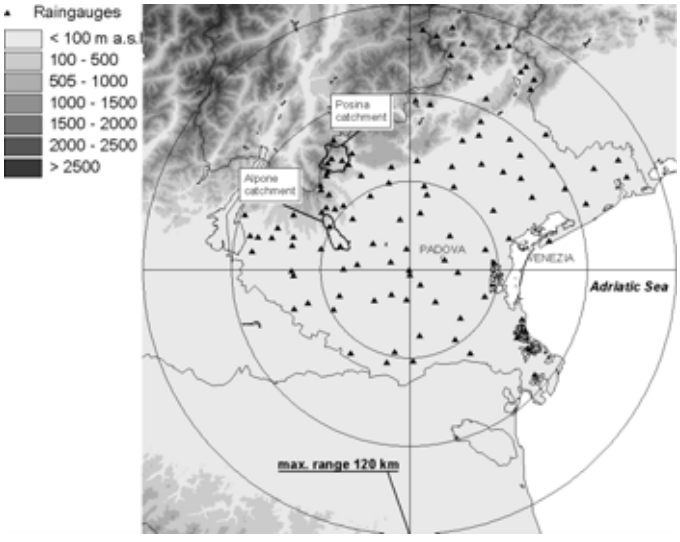


Figure 3.10:Presentation of the study area: a) Relief map of north-eastern Italy and location of the Monte Grande weather radar; b) Location of the Posina and Alpone basins and the raingauge network.

TABLE 3.4 Monte Grande weather radar characteristics.

Parameter	Value
Location	45° 21' 46" N, 11° 40' 25" E, 470 m a.s.l.
Wavelength	5.5 cm
Polarization	linear horizontal
Beamwidth (3dB)	0.9°
Peak Power	250 kW
Quantization	256 levels
Elevations	0°30', 1°, 1°30', 2°30', 3°30', 4°30', 6, 7°30', 10°, 15°
Range	120 km
Update time	15 min

3.2.3 Error sources and the radar rainfall estimation algorithm

Three broad categories of error sources can be identified in the radar estimation of rain intensity at the ground (Creutin et al., 2000): (1) lack of electronic stability and miscalibration of the radar system (Joss and Lee, 1995); (2) issues related to the radar detection environment, including interaction of the radar beam with the orography, beam broadening with distance, clutter and anomalous propagation, and visibility effects; (3) variability of the atmospheric conditions (i.e. issues related to variability in time and space of the vertical profile of reflectivity and issues related to the microphysics of precipitation). The radar rainfall estimation algorithm used in this study is based on a three-stage radar rainfall correction approach (Borga et al., 2000, 2002): (1) the preliminary identification of the radar detection environment, (2) adjustment of range-related errors associated with the vertical profile of reflectivity (VPR), and (3) attenuation correction and reflectivity-to-rain rate conversion. A summary of the adjustment procedures is reported below.

Identification of the radar detection environment

The interaction of electromagnetic waves with relief leads to ground clutter and screening effects. The domain of possible ground-interception and occlusion of the radar beam is examined here for each antenna elevation, by modelling the radar beam propagation in standard atmospheric conditions and using a detailed digital elevation map with 90-m grid size (Andrieu et al., 1997; Borga et al., 2000; Pellarin et al., 2002). These correction factors are only approximations computed under a number of assumptions (Pellarin et al., 2002), and the corrections might not fully reconstruct the exact situation (i.e., without blocking). The higher the level of partial beam blocking is, the less reliable the correction is expected to be. Application of this methodology requires therefore the specification of the minimum threshold of acceptable unblocked energy fraction, up to which blocking correction can be applied with confidence. Ground clutter removal was part of the raw radar data quality control system; hence, it is not included in the preprocessing steps described herein.

Fig. 3.11 denote the beam screening effect, in percentage of the transmitted power, for the scans of 0,5°, 1,0° an 1,5°. Inspection of Fig. 3.11 reveals a problematic region that lies between the 170th and 270th azimuth. The blockage for these azimuths is very severe, with complete blockage at 0,5° for some sectors. The screening starts very close to the radar, at a distance less than 10km. A wider blocked area is observed for the region 285-20, with screening starting at ranges comprised between 40 and 80 km. The two lowest elevation angles at which radar observations over the Alpone and the Posina basins, respectively, are unaffected by ground clutter and beam occlusion are 1.5° and 2.5°,

respectively. The mean radar beam distance from the ground over the Alpone at 1.5° beam elevation is around 800 m, and over the Posina at 2.5° beam elevation is around 1700 m.

Range effects at 1.5° and 2.5° beam elevations are mainly due to interaction of the radar beam with the melting layer, which is controlled by the freezing level. As an example consider Figure 4 in which the estimated altitude of the 0°C isotherm is plotted at hourly time steps together with the altitude of the radar reflectivity peak (if any) for the OCT96 event. The peak was computed by comparing azimuthally averaged reflectivity data from all beam elevations available over a circular ring ranging from 15 to 20 km. Figure 3.12 also shows the elevations of the upper and lower limits of the half-power beam width over the Alpone (with 1.5° beam inclination) and Posina (with 2.5° beam inclination) basins. It is clear that the observed mean bright band heights are in good agreement with the 0°C isotherm altitude estimates. It is noted that the centre of the bright band is typically from about 100 to 400 m below the 0°C isotherm (Battan, 1973). This figure also provides qualitative indications on the expected range-related effects over the selected basins for the considered event. Radar observations over the Alpone at 1.5° are slightly influenced by bright band. At 2.5° elevation over the Posina basin, radar beam is above the freezing level for most of the time and it mostly samples frozen hydrometeors. In that case, application of a Z-R relationship calibrated for rain would results in heavy underestimation of rainfall.

TABLE 3.5 Description of the selected events.

Event	Beginning of the event	Duration (hours)	Cumulated areal rainfall (mm)	
			over the Alpone basin	over the Posina basin
OCT92	2 Oct., 1992	120	237.6	440.3
SEP94	14 Sept. 1994	26	28.4	53.6
NOV94	6 Nov. 1994	72	100.6	149.9
OCT96	14 Oct. 1996	96	127.5	299.8
NOV96	13 Nov. 1996	120	75.7	179.9
DEC97	18 Dec 1997	84	101.1	126.1

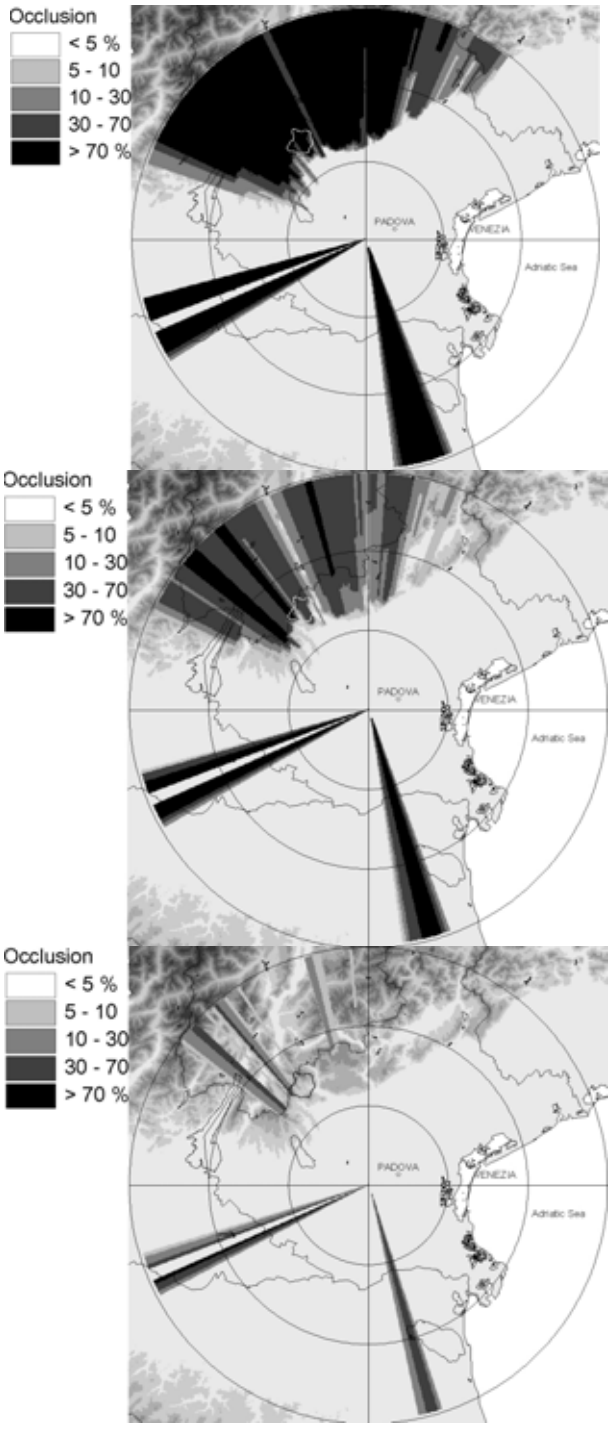


Figure 3.11: Maps of estimated power loss (in percentage) due to beam blockage calculated with a beam propagation model and DEM data at three different beam elevation scans: 0,5°, 1,0° and 1,5°.

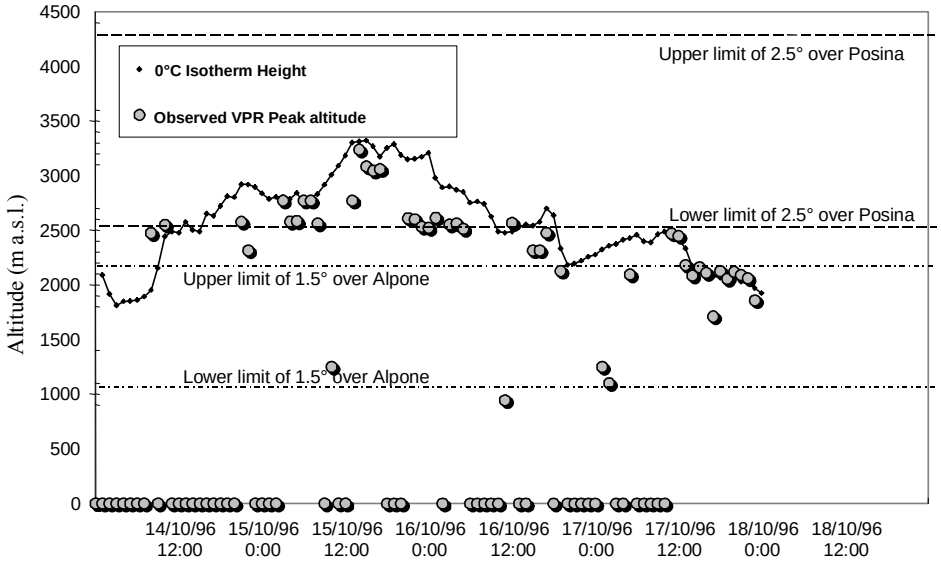


Figure 3.12: Altitude of the 0°C isotherm and of observed VPR peak for OCT96. Upper and lower limit of half-power beam altitude at 1.5° elevation and 2.5° elevation over the Alpone basin and the Posina basin (respectively) are reported.

Adjustment for non-uniform vertical profile of reflectivity

The procedure of Vignal et al. (1999) is used to estimate the vertical reflectivity profile from radar measurements. The approach is a generalisation of the method developed by Andrieu and Creutin (1995). It accounts for spatio-temporal variations in the VPR. It evaluates for discrete sectors and range intervals the average ratio of radar data between each elevation and the lowest scan (called 'ratio curves'). An inverse method is used to retrieve VPR profiles at different radar sectors from these ratio values using a single initial VPR estimate.The method is applied at the hourly time-step to detect fluctuations of the VPR within a storm event. The VPR is identified based on reflectivity data at 1.5° and 2.5° scan elevations. The area chosen for VPR identification covers the entire radar umbrella at ranges between 5 and 70 km. The definition of the initial VPR is inspired from the method proposed by Kitchen et al. (1994). The initial VPR is computed at every hour based on: i) the available surface wet bulb temperature data and a standard lapse rate to derive 0°C heights. ii) a bright band intensity and depth defined equal to 5 dB and 300 m, respectively, the profile above the bright band vanishing at 3 km. In summary, the retrieval of VPRs starts from the physically based approach suggested by Kitchen et al. (1994), which is corrected according to the local observations of VPRs provided by ratio curves.

The implementation of the algorithm requires selection of values for a number of parameters (Andrieu and Creutin, 1995). Important parameters are those characterising both the a priori information, which is formed by the vector of the initial VPR and its associated covariance matrix (with standard deviation, σz [dBZ], and distance decorrelation, Dz [km]), and the data (with coefficient of variation of the measurement error, A [-]). The parameters characterising the a priori information contain the initial knowledge of the parameters to identify (i.e., the VPR) and the level of confidence that can be ascribed to this knowledge. The parameter characterising the data describes the distribution of errors around the observations. Details on the statistical apparatus used in the identification procedure are reported by Andrieu and Creutin (1995) and by Vignal et al. (1999).

Attenuation correction and reflectivity-to-rain rate conversion

The rainfall estimation algorithm includes an attenuation adjustment for the 5-cm radar data. The adjustment is performed using an iterative procedure that is an implementation of the algorithm by Hildebrand (1978). Mathematically, the attenuation correction along the radar beam is formulated as a recursive system of three equations:

$$Z_C(r) = Z_M(r) + 2\Delta r \sum_{x=1}^{r-1} k(x) \tag{3.7}$$

where Z_M is the radar reflectivity factor adjusted for VPR effect, Z_C is the corrected reflectivity factor, K is the specific attenuation, r is the distance from the radar, and Δr is the distance step. The specific attenuation K is defined as the attenuation of the electromagnetic wave passing through the unit distance of a medium, usually expressed in logarithmic scale (dB km^{-1}) (Delrieu et al., 1991).

$$k(r) = \alpha R(r)^{\beta} \tag{3.8}$$

The rain rate R (mm h^{-1}) is estimated from the attenuation-corrected reflectivity based on a Z-R relationship

$$R(r) = \left[\frac{Z_C(r)}{a} \right]^{1/b} \tag{3.9}$$

The correction attenuation is applied up to the range which is affected by bright band, in case a bright band exists and is recognised by the VPR identification algorithm. Attenuation at ranges contaminated by bright band may be hardly described with Eq. (3.8) and is not considered here. The above procedure is repeated until successive iterations do not produce significant changes in the estimated total attenuation.

At this point, the radar volume data are converted to rainfall rates at the ground in the form of a polar coordinate map that has to be transformed into a rectangular grid. For each polar element of the volume, the lowest elevation characterised by a beam power blockage percentage less than a given threshold is selected. An effort to address the radar measurement geometry in the transformation algorithm was made because numerical noise introduced by inadequate spatial interpolation scheme can negatively affect the system performance (Ciach et al., 1997). The transformation algorithm divides a radar sampling volume into 10 discrete subazimuths to pick up the spatial pattern of the radar sampling volumes. Based on this discretization, the average of the rainfall rates from the elementary subdivisions of all the radar sampling volumes that project into a Cartesian 1 km² grid size pixel is computed.

The radar rainfall estimation algorithm is conceptually rather simple to afford adequate investigation of parameter uncertainty. Anyway, it allows taking into account the major error sources arising in radar rainfall estimation in the study area, as recognised during earlier investigations (Borga et al., 2000; Dinku et al., 2002).

Algorithm parameter estimation and examination of the optimal parameter values

The previous sections presented nine parameters (Table 3.6) that control the different components of the radar rainfall processing steps. Among those, the values of five parameters which in previous investigations showed relatively small intra-event variability (Borga et al., 2000, Dinku et al., 2002) are fixed, and the remaining four are obtained from a global optimization scheme. The four parameters are: the two parameters a and b of the Z-R relationship and the two parameter σz and Dz of the VPR

adjustment procedure which control the covariance matrix of the vector of initial VPR. Typical values of the a parameter may range from a few tens to several hundreds, while b is usually limited to 1 <b<3 (Battan, 1973; Smith and Krajewski, 1993). Accordingly with sensitivity analysis of Andrieu and Creutin (1995), typical values of σz range from 0.6 to 1.0, while Dz ranges between 0.1 km to 0.5 km.

TABLE 3.6: Algorithm parameters

Parameter	Description	Value
a	Z-R parameter	Optimised
b	Z-R exponent	Optimised
α	Attenuation correction parameter	0.005
β	Attenuation correction parameter	1.0
B [%]	Minimum threshold of unblocked energy	60%
σ_z [dBZ]	VPR adjustment parameter	Optimised
D_z [km]	VPR adjustment parameter	Optimised
A [-]	VPR adjustment parameter	0.1
D_q [km]	VPR adjustment parameter	1.0 km

The optimization criterion is based on the Fractional Standard Error (FSE) computed between event radar accumulations (Ri) and corresponding gauge storm event accumulations (GRi)

$$FSE = \frac{\left[\frac{1}{n}\sum_{i=1}^{n}\left(R_i - GR_i\right)^2\right]^{0.5}}{GR_{ave}} \qquad (3.10)$$

and on the Mean Relative Error (MRE):

$$MRE = \frac{\sum_{i=1}^{n}(R_i - GR_i)}{GR_{ave}} \qquad (3.11)$$

where i represents the i-th station, n is the number of stations and GR_{ave} is the mean value of the gauge accumulations.

The objective functions are evaluated on the final radar estimates after all error correction procedures have been implemented. This approach is conceptually similar to previous work by Ciach et al. (1997), Anagnostou and Krajewski (1998, 1999) and Dinku et al. (2002). We implement the Shuffled Complex Evolution global optimization scheme proposed by Duan et al. (1993) to determine the optimal parameter values. This scheme, primarily developed for hydrological applications, is robust, effective, and efficient for a broad class of optimization problems. An assumption used here is that single rain gauges can provide sufficiently accurate approximations of the areal rainfall averaged over the Cartesian grid of the radar rainfall estimate. This assumption can be justified because, for the time scales considered here (event accumulations), investigations from Ciach and Krajewski (2006) suggest that the spatial rainfall variability at scales less than 1 km is relatively small.
Storm event accumulations are used for calibration purposes, instead of using accumulations at shorter time step, to mimic typical use of radar observations at space and time where raingauge measurements

are often not available, both for real-time use but also for post event analysis of flood-generating storm analysis. In these cases, the quality of the radar rainfall estimates is often checked at the time scales where raingauge measurements are available, or where the observational uncertainties are reduced.

An assumption here is that the algorithm parameters obtained by comparison with rain gauge data at a certain time accumulation may be used at different time accumulations. Morin et al. (2003) have shown, considering a simple power-law reflectivity-to-rain-rate conversion, that optimal parameter of the Z-R relationship are scale-dependent, because they are shifted in parameter space systematically as the time and space scales change. More specifically, increased time- and space scales resulted in considerable increase of the a parameter and decrease of the b parameter. Therefore, care should be exerted when the radar rainfall algorithm parameters are obtained at a certain space-time scale (by comparison with rain gauge data) and used at different scales. However, Morin et al. (2003) showed that sensitivity to time scale is reduced at accumulations exceeding 50 minutes. Moreover, these researchers showed that most of the sensitivity to scale depends on observation error, which tend to increase with reducing the integration time. It is therefore reasonable to estimate algorithm parameter at the event accumulation scale and to apply the same parameters at hourly time steps.

The four parameters estimated through the calibration procedure and their optimum values are listed in Table 3.7 for the six events. FSE and MRE are reported in Table 3.8 and are computed both at the event time scale and at the hourly time scale to provide an assessment of the quality of the estimates at the two different time scales. Unadjusted radar rainfall estimates considered here are obtained at 1.5° elevation scan, without any correction for the various error sources mentioned above. A radar-raingauge scatter plot is reported, for unadjusted and adjusted radar estimates, in Figure 3.13 for the OCT1992 event.

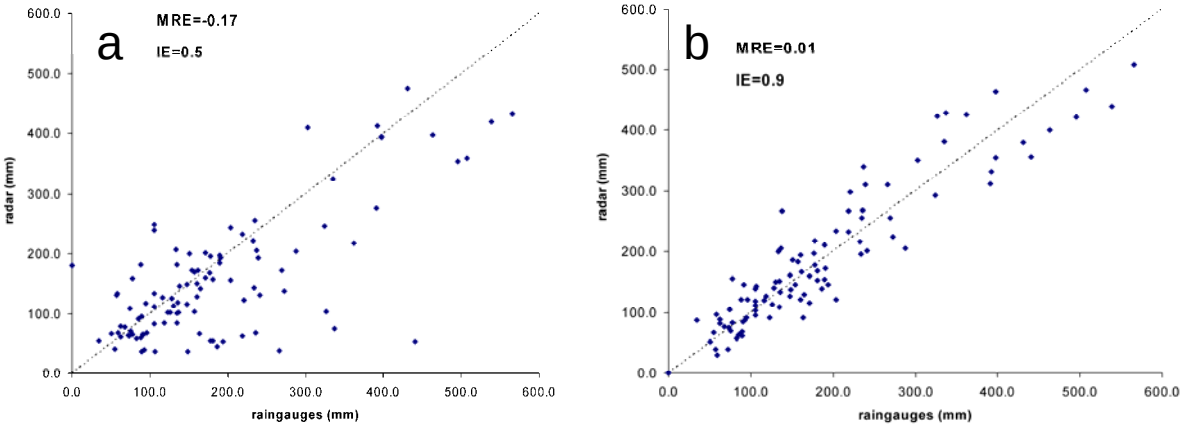


Figure 3.13: Scatterplot of radar estimates and raingauge event accumulations for the OCT92 event: (a) unadjusted radar estimates, (b) adjusted radar estimates

Results from the scatterplot and from the statistics reported in Table 3.8 shows that application of the radar algorithm allows increasing effectively the quality of the radar estimates, at the two time accumulations. Bias is almost completely removed with a considerable increase of the correlation. FSE values at the hourly time steps decreases up to 37% for the events of OCT92 and NOV96.

Inspection of Table 3.7 reveals also that there is a rather wide variability among the optimum parameter sets. It is observed that values of the b parameter are generally rather high. This is likely to be a consequence of using the FSE criterion to drive the optimization procedure with errors resulting from Z measurement, quantification, inadequate sample, size etc (Morin et al., 2003; Jameson and Kostinski, 2002). Values of the parameter a are always less than the value used in the traditional Marshal-Palmer relationship. This is likely to be an effect of the radar calibration error, which were

identified in the radar observations available (Dinku et al., 2002) despite operational frequent use of a built-in calibration of the receiver and solar calibration of the antenna positioning system. Effects of radar calibration error are often indistinguishable from errors in the a parameter of the Z-R relationship.

The variability in the estimated parameters shows that it is hardly possible to find a unique parameter set. Therefore, there may be many sets of parameters which give similar good results during a calibration period, but the quality of the corresponding estimates may differ in other cases. For this reason, it is important to evaluate sensitivity of the radar algorithm to parameter uncertainty, and to use the sensitivity analysis to quantify the impact of parameter uncertainty in the final rainfall estimates.

TABLE 3.7: Optimised parameters for the six events

Event	a	b	σ_z [dBZ]	D_z [km]
OCT92	154.0	1.64	0.64	0.59
SEP94	167.0	1.76	0.87	0.63
NOV94	189.0	1.85	0.55	0.78
OCT96	174.0	1.76	0.96	0.54
NOV96	135.0	1.58	0.82	0.67
DEC97	110.8	1.79	0.64	0.32

TABLE 3.8: Statistical analysis of rainfall estimation by using unadjusted and adjusted radar observations

	Unadjusted radar estimates			*Adjusted radar estimates*		
Event	*FSE (hourly accumulations)*	*FSE (event accumulations)*	*MRE*	*FSE (hourly accumulations)*	*FSE (event accumulations)*	*MRE*
OCT92	1,41	0,46	-0,20	0.90	0.33	0.01
SEP94	0,97	0.69	-0,26	0.79	0.61	-0.03
NOV94	0,85	0,66	-0,43	0.70	0.51	-0.04
OCT96	1,28	0,63	-0,43	0.89	0.42	0.06
NOV96	1,96	0,66	-0,23	1,25	0.55	-0.05
DEC97	1,07	0,70	-0,34	0.85	0.51	0.04

3.2.4 The Generalized Likelihood Uncertainty Estimation (GLUE) methodology

Two methods of uncertainty analysis have emerged in the last decades in environmental modelling: the Generalized Likelihood Uncertainty Estimation or GLUE methodology (Beven and Binley, 1992) and various Bayesian Markov Chain Monte Carlo or MCMC methods (e.g. Kuczera and Parent, 1998; Vrugt et al., 2003). While these approaches tend to be computationally intensive, the GLUE methodology is more easily implemented as there are fewer stringent assumptions and can fully incorporate the algorithm nonlinearity discussed above. Moreover, consider that in our algorithm analysis, performing a Bayesian MCMC analysis would require a very difficult process of deriving a correct description of the residual errors which are correlated in time and space. As reported above, this description could only be advanced with use of radar-raingauge residuals; as a result, knowledge of the residual error structure will be poor exactly in those situations where utility of an evaluation of the radar information is highest, i.e., when there is few information from the raingauge network.

As a result, our study will utilize pseudo-likelihood functions and thus focus comparisons with GLUE and will not investigate other uncertainty analysis methods such as Bayesian MCMC methods that require the definition of a formal likelihood function. For brevity, in the following we keep our description of GLUE to a minimum but refer readers to Beven and Binley (1992), Beven and Freer (2001) or Montanari (2005) for more complete descriptions of GLUE.

GLUE requires that modelers subjectively define a 'likelihood' function that monotonically increases as agreement between model predictions and measured calibration data increases (Beven and Binley, 1992). The GLUE likelihood function can be, but is not required to be and is not typically, a statistically based likelihood function. A large number of GLUE studies utilize the Nash-Suttcliffe coefficient (1970) or some transformation of it to define the likelihood function. In essence, when considering parameter uncertainty, GLUE is focused on identifying multiple acceptable or 'behavioral' parameter sets rather than the optimal parameter set. The idea that multiple parameter sets lead to reasonable or acceptable predictions of calibration data is referred to as the 'equifinality' concept (Beven and Freer, 2001). The operator must subjectively define behavioral in terms of the selected likelihood function (e.g. a threshold value of the likelihood function). A Monte Carlo experiment is then conducted to independently sample model parameter space and identify various behavioral parameter sets. The operator must subjectively determine whether a sufficient number of behavioral parameter sets are sampled. In addition, the operator would subjectively determine (typically make an implicit assumption) that behavioral samples from across behavioral parameter space (e.g. higher quality samples) were also identified. These behavioural parameter sets are then subjectively transformed and assigned relative weights based on their likelihood measure such that the weights sum to one. Then, the weighted behavioral parameter sets can be used in an ensemble estimation procedure to estimate prediction quantiles of the quantity of interest (Beven and Freer, 2001). This means that for any time period of interest, estimates generated by using all the behavioral parameter sets are considered in order to quantify uncertainty.

The results of a GLUE analysis are typically presented as GLUE prediction limits (prediction quantiles) around an algorithm estimate of interest. It is important to realize for the purposes of this paper that GLUE prediction limits generated with a pseudo-likelihood function are not equivalent to statistical confidence limits. According to Beven and Freer (2001), the resultant GLUE prediction limits are not direct estimates of the probability of simulating a particular observation. The GLUE method is convenient to apply and, as a multitude of publications and citations attests (more than 250 publications refer to the Beven and Binley (1992) GLUE publication), it has been widely used in research and practice. GLUE has stood the test of time, but has also been subject to cogent criticism, most recently by Mantovan and Todini (2006). In particular, the use of 'informal' likelihood functions and the setting of likelihoods to zero for 'non-behavioural' models has been questioned. However, use of formal likelihood functions may be based on strong and in several cases untenable assumptions about the nature of model structural error. Beven et al. (2006) demonstrate that incautious use of formal likelihoods can, in the presence of model structural error, lead to inaccurate prediction and uncertainty estimates.

Application of the GLUE methodology for radar rainfall uncertainty assessment

The parameters of the algorithm varied in the Monte Carlo realisations are shown in Table 3.9, together with their respective ranges and sampling strategy. The parameter ranges were chosen accordingly with findings from the calibration procedure described above. It is important within GLUE to ensure that there is sufficient sampling of the parameter space so that a representative range of behavioural algorithm run are retained. In this application 10000 parameter sets were selected from the specified ranges. This number of sample realizations was established by checking the stability of the rainfall estimates distributions with increasing the number of simulations. No attempt was made to account for possible covariation between the parameter values in these prior choices. As noted by Beven and Binley (1992), since each parameter set is treated as a set, the conditioning within the GLUE will implicitly account for covariation in the posterior distribution.

TABLE 3.9. Parameter value ranges used for GLUE sampling.

	Minimum Value	Maximum Value	Sampling Strategy
a	100.0	300.0	Uniform
b	1.0	2.0	Uniform
σ_z (dBZ)	0.5	1.2	Uniform
D_z (km)	0.01	0.7	Uniform

Consistently with the calibration framework described above, the likelihood measure is represented by the Nash-Sutcliffe efficiency computed over the raingauge network at the storm accumulation time scale:

$$E = 1 - \frac{\sum_{i=1}^{n} (R_i - GR_i)^2}{\sum_{i=1}^{n} (GR_i - GR_{ave})^2} \qquad (3.12)$$

The coefficient of efficiency is dimensionless and it is easily interpreted. If the algorithm estimates rainfall at the ground with perfection then E=1. If E<0 then the algorithm's estimation accuracy is worse than simply using the average of the raingauge values. The acceptable rejection threshold has been fixed at E=0.5.

Uncertainty limits are derived at any time step and at any grid location by considering the acceptable rainfall estimates obtained by each algorithm run and by ranking these in order of magnitude. Then, using the likelihood weight associated with each run, a distribution function of the estimates may be calculated. From this distribution function various summary values can be calculated, such as weigthed mean estimated rainfall and selected quantiles. Here we used the estimates of the 5th and 95th percentiles of the cumulative likelihood distribution as the uncertainty limits of the estimates. The GLUE approach allows computing uncertainty limits for both cumulated and area-averaged rainfall estimates. In these cases, the radar rainfall estimates by each sample algorithm run are either cumulated or area-averaged and then, using the weights associated to each run, a distribution function of the estimated averaged rainfall is calculated. An hourly rainfall field map obtained from the 50th percentile (median) values and the corresponding 90% uncertainty bounds are shown in Figure 3.14.

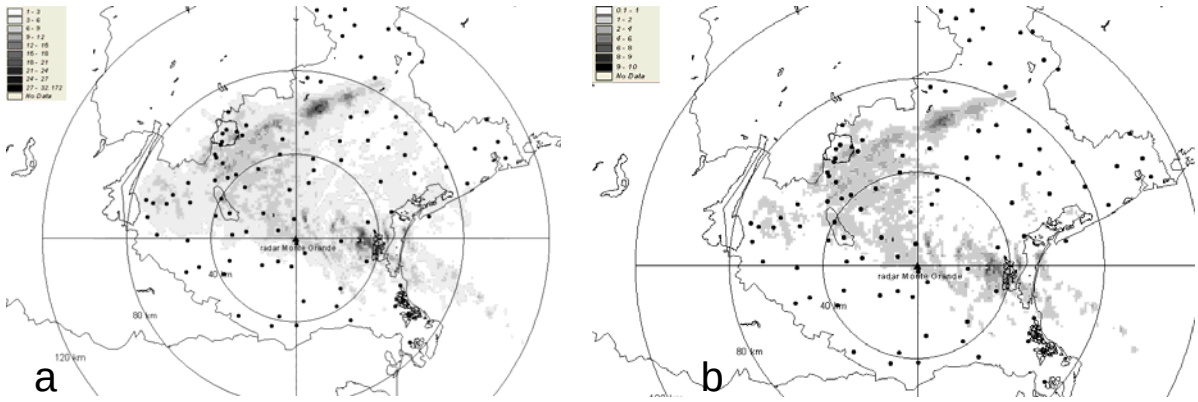


Figure 3.14: Hourly map of (a) radar rainfall estimates and (b) corresponding 90% uncertainty bounds for 09:00 UTC of October 4 1992.

Comparing radar rainfall estimates uncertainty with raingauge-based areal rainfall estimates

Figures 3.15 and 3.16 show hourly comparison of adjusted radar estimates and uncertainty bounds with area-averaged rainfall estimates over the Posina and Alpone basins for the OCT92 and NOV96 storm events, respectively. The Kriging statistical technique was used to estimate areal-rainfall from point measurements over the two basins. We used ordinary block kriging, performed based on a single climatological estimate of the rainfall variogram structure (Borga et al., 2000).

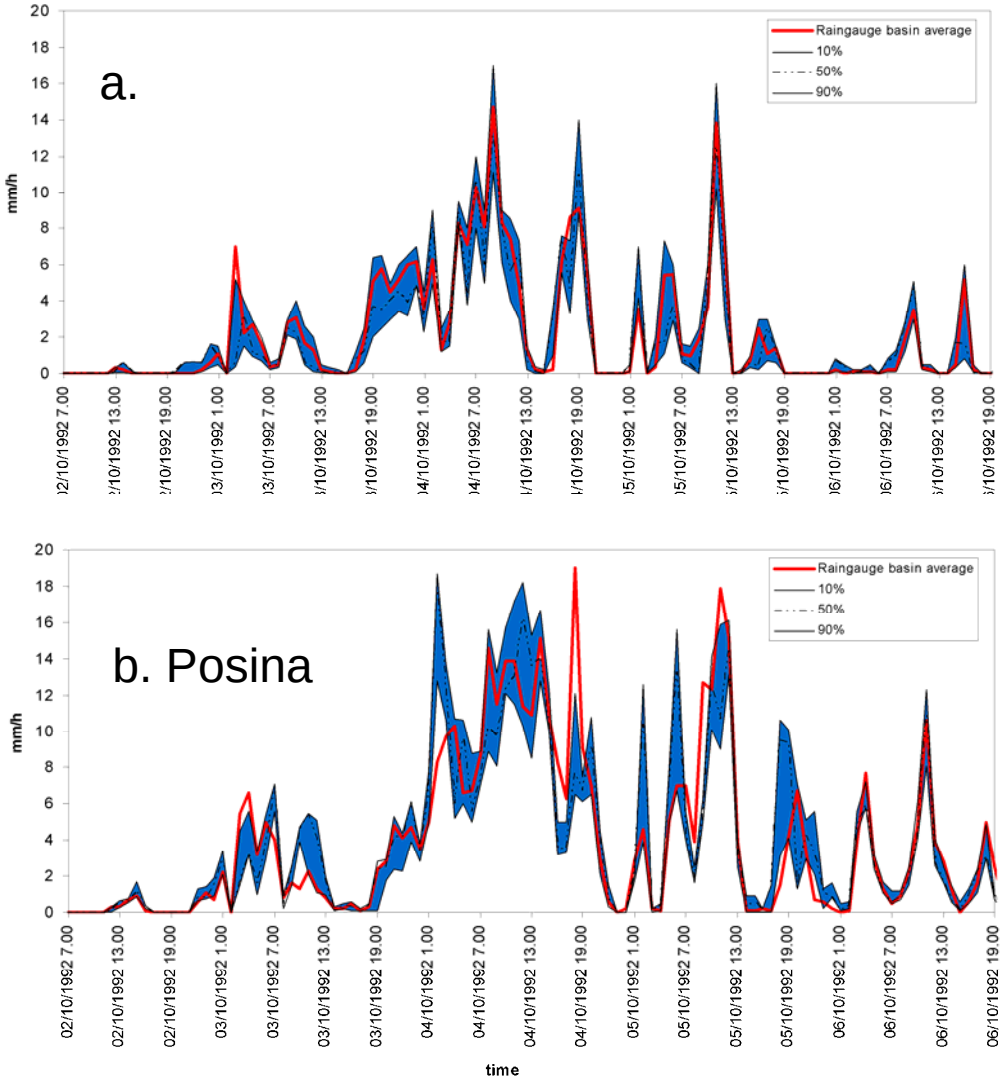


Figure 3.15. Basin-averaged radar rainfall estimation for the OCT92 storm event: 90% uncertainty bounds, median, and reference rainfall for a) Alpone, and b) Posina.

The results show that the radar rainfall estimates reproduce the reference rainfall reasonably well. For the Posina, noticeable over-prediction and under-prediction episodes are shown, which are mainly related to errors in the VPR correction algorithm. The 90% uncertainty bounds brackets the reference rainfall most of the time, particularly for the closer basin (Alpone). For some periods the uncertainty bounds are quite large, indicating that the estimation uncertainty is considerable. Over the more distant basin (Posina), the 90% uncertainty region does not always bracket the reference rainfall, indicating that the algorithm structure may be in need of further improvement. The uncertainty bounds computed

over the Posina are generally larger than those computed over the Alpone, indicating the effect of range on uncertainty in radar rainfall estimation. This effect is particularly important for the Posina during the NOV96 storm event. This event was characterised by both considerable impact of variability in the vertical profile of reflectivity and intermittency in the precipitation field. The adjustment for VPR effect was therefore particularly difficult, due to extrapolation of the profile shape from regions far away under the radar umbrella. The result of such uncertainty is the large uncertainty bounds for the Posina basin.

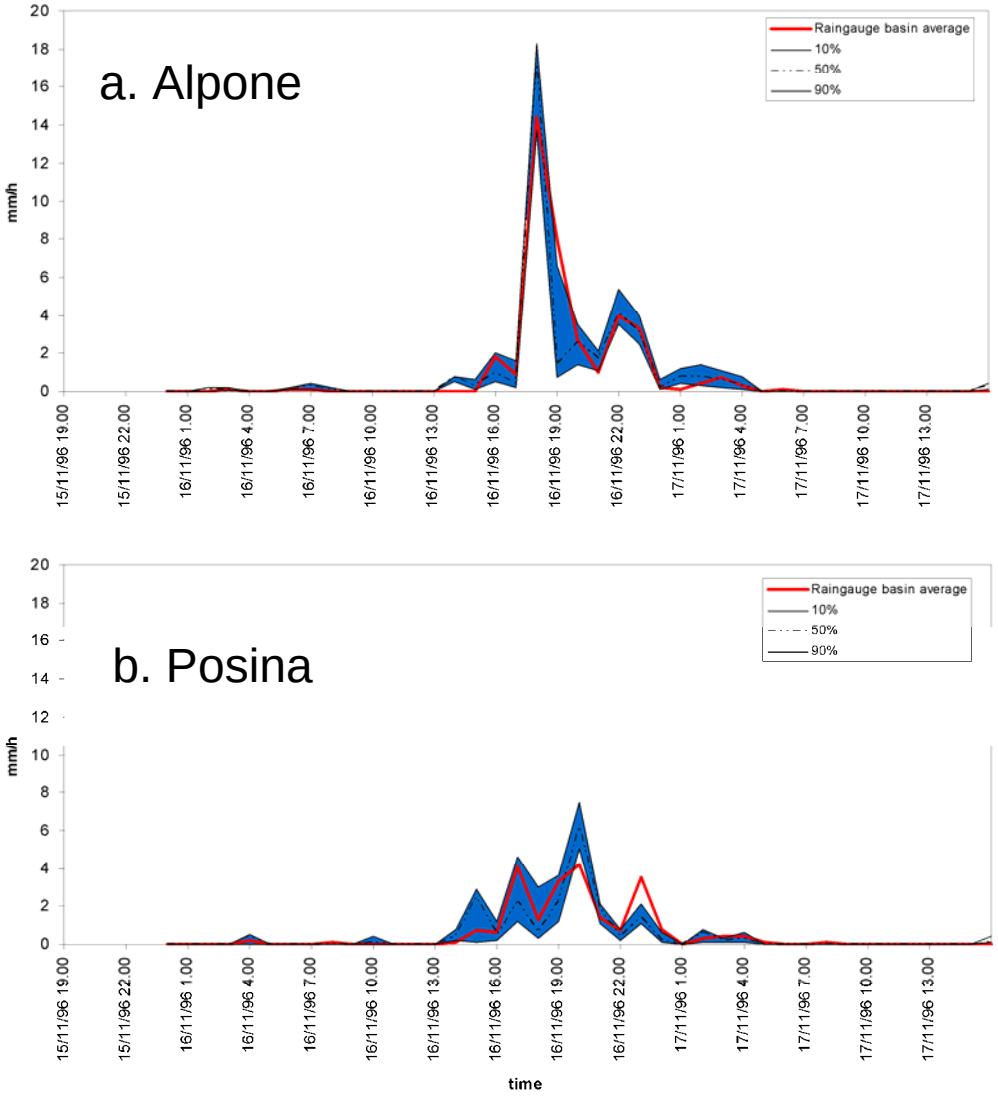


Figure 3.16. Basin-averaged radar rainfall estimation for the NOV96 storm event: 90% uncertainty bounds, median, and reference rainfall for a) Alpone, and b) Posina.

Parameter sensitivity analysis

Our objective here is to evaluate the importance of each algorithm parameter in the estimation of rainfall at the ground. This sensitivity analysis can be carried out by using the GLUE directly as a development of the Generalised Sensitivity Analysis (GSA), employed by Spear and Hornberger (1980). The key idea is to compare the distribution of the parameter values associated with acceptable results (behavioural) with the distribution of parameter values associated with non acceptable results

(non behavioural). If the two distributions are not statistically different, the parameter is unimportant for the estimation problem considered. If the two distributions differ significantly, the parameter is important.

The four algorithm parameter values distributions, obtained from the Monte Carlo simulations, were subjected to a statistical analysis to elucidate sensitivity characteristics. Three sensitivity classes based on the Kolmogorov-Smirnov statistic, dn, were selected: insensitive for dn≤0.1, moderately sensitive for 0.1<dn<0.2, and sensitive for dn ≥0.2. The use of this statistic in conjunction with the GSA has been discussed by Hornberger et al. (1986) and Beven (2001). As noted by these authors, this or any other statistic when used for sensitivity analysis within a Monte Carlo exercise should not be considered as a criterion for hypothesis testing in a traditional sense but rather as a useful index for ranking parameter sensitivity.

The sensitivity analysis was carried out considering three different data conditioning scenarios to evaluate sensitivity at different ranges from the radar antenna. With the first scenarios (Scenario A), all raingauge data up to 120 km from the radar antenna were used to derive behavioural and non-behavioural parameter distributions. With the second scenario (Scenario B), only the stations at a distance less than 40 km from the radar antenna were considered. With the third Scenario, only the stations at a distance comprised between 40 km an 120 km from the radar antenna were considered.
Statistics reported in Table 3.2.7 show that parameters a and b are always sensitive parameters. Results reported for parameter σz shows that this parameter is sensitive for Scenario A and C, but not for Scenario B. This provides evidence that the adjustment for the effects of vertical profile of reflectivity is unimportant at ranges less than 40 km, at least for the events considered here. This is not unexpected, given the structure of the VPR for most of the events under study. Parameter Dz is insensitive under Scenarios A and B, and is moderately sensitive when the algorithm is conditioned with data comprised between 40 and 120km. This finding suggests again that sensitivity to parameters controlling the VPR adjustment procedure increases with the range used to condition the algorithm. It is also interesting to observe that the difference in sensitivity between parameters σz and Dz mirrors earlier results obtained by Andrieu and Creutin (1995).

TABLE 3.10: Results of the sensitivity analysis

	Scenario A Range 0-120 km	Scenario B Range 0-40 km	Scenario C Range 40-120 km
Parameter			
a	†	†	†
b	†	†	†
σ_z	†	∗	†
D_z	∗	∗	+

† indicates sensitive $d_n \geq 0.2$
+ indicates moderately sensitive $0.1 < d_n < 0.2$
∗ indicates insensitive $d_n \leq 0.1$

A further investigation was carried out to investigate sensitivity of the parameter α controlling attenuation correction. This parameter was included into the GLUE procedure; accordingly with earlier investigations (Dinku et al., 2002) a uniform sampling procedure was used on a range comprised between 0.001 and 0.008. The stochastic simulation led to divergence in 15% of the 10000 simulations. In these cases, the iterative correction procedure was stopped. Results from this analysis are reported in Table 3.11 and show that sensitivity is high at ranges close to the radar, while it is negligible at ranges comprised between 40 and 120 km. This last finding is expected, since the attenuation correction algorithm is carried out up to the ranges affected by the bright band, as this is

identified by the VPR correction procedure. This implies that when VPR correction is important, attenuation correction is not.

TABLE 3.11: Results of the sensitivity analysis, including attenuation correction

	Scenario A Range 0-120 km	Scenario B Range 0-40 km	Scenario C Range 40-120 km
Parameter			
a	†	†	†
b	†	†	†
σ_z	†	*	†
D_z	*	*	+
α	+	†	*

† indicates sensitive $d_n \geq 0.2$
+ indicates moderately sensitive $0.1 < d_n < 0.2$
* indicates insensitive $d_n \leq 0.1$

3.2.5 Conclusion

Realistic assessment of parameter uncertainty in complex radar rainfall estimation algorithms has received relatively little attention in the research literature. Because traditional statistical theory based on first-order approximations has typically not been able to cope with the nonlinearity of radar rainfall algorithms, it has not been possible to undertake with any confidence tasks such as evaluating prediction/confidence limits of rainfall estimates, which has several practical implications on the use of radar rainfall estimates in hydrological and numerical weather prediction models. This study considers a Monte-Carlo based approach for assessing parameter uncertainty in a radar rainfall estimation algorithm. The method, known as GLUE, has seen several hydrological applications.

Through a case study it has been recognized that radar rainfall estimation algorithm may suffer from the equifinality problem: this means that relatively good fit is achieved across the parameter ranges, implying that individual parameter values are less important than the parameter set as a whole and that parameter interactions dominate the estimate provided by the algorithm. It has been shown that the uncertainty assessment through the GLUE methodology is practical and relatively simple to implement and can also provide useful information that helps to understand better the strengths and limitations of the radar-rainfall algorithm under investigation. The assessment of radar rainfall estimation uncertainty thus obtained is conditioned on the definition of the likelihood function, input data, algorithm structure and structure of the conditioning process.

It has been shown that radar rainfall estimation uncertainty increases with scan elevation angle and with the range, until a distance from the radar is reached, beyond which radar rainfall detection failures play a more significant role and uncertainty decreases.

Natural extensions of this work include: (a) assessment of the uncertainty reduction made possible with increasing the number of beam elevations, including more observations for VPR identification purposes (for instance, from vertically oriented radar observations) and additional raingauge data for algorithm conditioning; (b) repeating the analysis with different seasons and different rainfall regimes to detect possible seasonal effects on rainfall estimation uncertainty; (c) analysing the sensitivity of the results to space-time averaging of rainfall; (d) examining the effects of different likelihood functions and parameter sampling ranges within the GLUE methodology; (e) evaluating the propagation of radar rainfall uncertainty through rainfall-runoff transformation.

The GLUE method is not limited by the complexity and non-linearity of the model. However, to obtain statistically reliable results, a large number of runs must be made before convergence of the model output uncertainty is obtained, which is the major disadvantage of this approach. It is possible that recently proposed algorithms, such as the Monte Carlo Markov Chain algorithm, may alleviate this problem and allows for a meaningful solution by using only a modest number of Monte Carlo repetitions.

4. References

1. Anagnostou EN., Krajewski WF 1998. Calibration of the WSR-88D precipitation processing system. *Weather forecasting*, **13**, 396-406.

2. Anagnostou EN, Krajewski WF 1999. Real-time rainfall estimation, part I: algorithm formulation. *J Atmos. Ocean Tech.* **16**(2), 189-197.

3. Andrieu H. and J.D. Creutin, 1995: Identification of vertical profiles of reflectivities for hydrological applications using an inverse method. Part I: formulation. *J. Appl. Meteor.*, **34**, 1, 225-239.

4. Andrieu H., G. Delrieu and J.D. Creutin, 1995: Identification of vertical profiles of reflectivities for hydrological applications using an inverse method. Part II: sensitivity analysis and case study. *J. Appl. Meteor.*, **34**, 1, 240-259.

5. Andrieu, H., J. D. Creutin, G. Delrieu, and D. Faure, 1997: Use of a weather radar for the hydrology of a mountainous area. Part I: Radar measurement interpretation. *J. Hydrol.*, 193, 1-25.

6. Bacchi, B., R. Ranzi and M. Borga, 1996: Statistical characterization of spatial patterns of rainfall cells in extratropical cyclones. *J. Geophys. Res.*, **101**(D21), 26,277-26,286.

7. Battan, L.J., 1973: Radar observation of the atmosphere. The University of Chicago Press, 324 pp.

8. Beard, K. (1976), Terminal velocity and shape of cloud and precipitation drops aloft, *J. Atmos. Sci.*, **33**(5), 851-864.

9. Berne, A., G. Delrieu, J.-D. Creutin, and C. Obled (2004), Temporal and spatial resolution of rainfall measurements required for urban hydrology, *J. Hydrol.*, **299**(3-4), 166-179.

10. Beven, K.J.,2001: Rainfall-runoff modelling: the primer. Wiley, 360 pp.

11. Beven KJ, Binley AM 1992. The future of distributed models: model calibration and uncertainty prediction. *Hydrol. Processes*, 6, 279-298.

12. Beven K, Freer J 2001. Equifinality, data assimilation, and uncertainty estimation in mechanistic modelling of complex environmental systems using the GLUE methodology. *J. Hydrol*. 249 (1-4), 11-29.

13. Beven KJ, Smith PJ, Freer J. 2006. On the Bayesian coherence of GLUE and the information content of observations in hydrological modelling. *Journal of Hydrology* (in press).

14. Borga M, Anagnostou EN, Frank E 2000. On the use of real-time radar rainfall estimates for flood prediction in mountainous basins. *J. Geophys. Res.* 105: (D2) 2269-2280.

15. Borga M. Tonelli F, Moore RJ, Andrieu H. 2002. Long term assessment of bias adjustment in radar rainfall estimation. *Water Resour. Res.*, **38**(11), 1226, doi:10.1029/2001WR000555.

16. Ciach G.J, Krajewski WF, Anagnostou EN, Smith J, McCollum JR, and Kruger A., 1997: Radar Rainfall estimation for the ground validation studies of the tropical rainfall measuring mission. *J. Appl. Meteor.*, **38**, 1519-1525.

17. Ciach GJ, Krajewski WF 1999. On the estimation of radar rainfall variance. *Adv. Wat. Resour.*, 22, 6, 585-595.

18. Ciach, G.C. and W.F. Krajewski, 2006: Analuysis and modelling of spatial correlation structure of small-scale rainfall in central Oklahoma. Av. Water Res., 29, 1450-1463.

19. Ciach, G.C., Witold F. Krajewski, Gabriele Villarini, 2007: Product-Error-Driven Uncertainty Model for Probabilistic Quantitative Precipitation Estimation with NEXRAD Data. *J. Hydrometeorol.*, 8(6), 1325-1347.

20. Chapon, B., 2006: Etude des pluies intenses en région Cévennes-Vivarais à l'aide du radar météorologique - Régionalisation des traitements radar et analyse granulométrique des pluies au sol, (Radar observation of intense Mediterranean precipitation: radra data processing regionalization and analysis of drop size distribution at ground). PhD Thesis of the University Joseph Fourier, Grenoble, 189 p.

21. Chapon, B., G. Delrieu, M. Gosset, and B. Boudevillain, 2008: Variability of rain drop size distribution and its effet on the Z-R relationship - A case study for intense Mediterranean precipitation. *Atmospheric Research*, 87, 52-65.

22. Ciach, J. G. and W. F. Krajewski, 1999: Radar-raingauge comparison under observational uncertainties. *J. Appl. Meteor.*, 38, 1519-1525.

23. Creutin, J. D. and C. Obled, 1982: Objective analysis and mapping techniques for rainfall fields: An objective comparison. *Water Resources Research*, **18,** 413-431.

24. Creutin, J. D., G. Delrieu, and T. Lebel, 1988: Rain measurement by raingage-radar combination: A geostatistical approach. *J. Atmos. Oceanic Technol.*, 5, 102-115.

25. Creutin JD, Borga M, Joss J 2000. Hydrometeorology: storms and flash floods. *Mountainous Natural Hazards*, F. Gillet and F. Zanolini Ed., Cemagref Edt., 349-366.

26. Delrieu, G., A. Bellon, and J. D. Creutin, 1988: Estimation de lames d'eau spatiales à l'aide de données de pluviomètres de radar météorologique. *J. Hydrol*., 98, 315-344.

27. Delrieu, G., J. D. Creutin, and I. Saint-Andre, 1991: Mean *K–R* relationships: Practical results for typical weather radar wavelengths. *J. Atmos. Oceanic Technol.,* **8,** 467–476.

28. Delrieu, G., J. D. Creutin, and H. Andrieu, 1995: Simulation of X-band weather radar mountain returns using a digitized terrain model. *J. Atmos. Oceanic Technol*., 12, 1038-1049.

29. Delrieu, G., S. Serrar, E. Guardo, and J.-D. Creutin (1999), Rain measurement in hilly terrain with X-band weather radar systems: accuracy of path-integrated attenuation estimates derived from mountain returns, *J. Atmos. Oceanic Technol.*, **16**(4), 405-415.

30. Delrieu, G., V. Ducrocq, E. Gaume, J. Nicol, O. Payrastre, E. Yates, P.-E. Kirstetter, H. Andrieu, P. A. Ayral, C. Bouvier, J. D. Creutin, M. Livet, A. Anquetin, M. Lang, L. Neppel, C. Obled, J. Parent-du-Chatelet, G. M. Saulnier, A. Walpersdorf, and W. Wobrock, 2005: The catastrophic flash-flood event of 8-9 September 2002 in the Gard region, France: a first case study for the Cévennes-Vivarais Mediterranean Hydro-meteorological Observatory. *J. Hydrometeor.*, **6**, 34-52.

31. Dinku T, Anagnostou EN, Borga M. 2002. Improving Radar-based Estimation of Rainfall Over Complex Terrain. *Journal of Applied Meteorology, 41(12), 1163–1178, 2002.*

32. Duan, Q., V. Gupta, and S. Sorooshian, 1993: Shuffled complex evolution approach for effective global minimization. *J. Optim. Theor. Appl.,* **76,** 501–521.

33. Fabry, F. (1996), On the determination of scale ranges for precipitation fields, *J. Geophys. Res.*, **101**(D8), 12,819-12,826.

5. Fulton RA, Breidenbach JP, Seo DJ, Miller DA 1998. The WSR-88D rainfall algorithm. *Weather and Forecasting*, 13, 377-395.

34. Germann, U. and J. Joss, 2002: Mesobeta profiles to extrapolate radar precipîtation measurements above the Alps to the ground level. *J. Appl. Meteor.*, **41**, 542-557.

6. Germann, U., G. Galli, M. Boscacci, and M. Bolliger, 2006: Radar precipitation measurement in a mountainous region. *Q. J. R. Meteorol. Soc*., **132**, 1669-1692.

7. Germann, U., M. Berenguer, D. Sempere-Torres, and G. Salvadè, 2006: Ensemble radar precipitation estimation - a new topic on the radar horizon. Proceedings, *Fourth ERAD Conference*, Barcelona, Spain, 559-562.

35. Habib, E., J. G. Ciach, and W. F. Krajewski, 2004: A method to filtering out raingauge representativeness errors from the verification distributions of radar and raingauge rainfall. *Advances in Water Resources*, 27, 967-980.

36. Haddad, Z., and D. Rosenfeld (1997), Optimality of empirical *Z-R* relations, *Quart. J. Roy. Meteor. Soc.*, **123**(541), 1283-1293.

8. Hildebrand, P. H., 1978: Iterative correction for attenuation of 5 cm radar in rain. *J. Appl. Meteor.*, **17,** 508–513.

9. Hitschfeld, W., and J. Bordan (1954), Errors inherent in the radar measurement of rainfall at attenuating wavelengths, *J. Meteor.*, **11**(1), 58-67.

10. Hornberger, G. M., B. J. Cosby, and J. N. Galloway, 1986: Modelling the effects of acid deposition: Uncertainty and spatial variability in estimation of long-term sulfate dynamics in a region, Water Resour. Res., 22(8), 1293– 1302.

37. Jacq V., 1994: Inventaire des situations à précipitations diluviennes sur les régions Languedoc-Roussillon, PACA et Corse, période 1958-1994 (Inventory of extreme precipitation events in the Languedoc-Roussillon, Provence Côte d'Azur and Corse regions in the period 1958-1994). *Phénomènes remarquables*, n°3, Météo France, SCEM, 1994, 190 pp.

38. Jameson, A., and A. Kostinski (2001), What is a raindrop size distribution?, *Bull. Amer. Meteor. Soc.*, **82**(6), 1169-1177.

11. Jameson, A. R., and A. B. Kostinski, 2002: Spurious power-law relations among rainfall and radar parameters, Q. J. R. Meteorol. Soc., 128, 2045– 2058, 2002.

39. Joss, J., and A. Waldvogel, 1990: Precipitation measurement and hydrology. *Radar in Meteorology: Battan Memorial and 40th Anniversary Radar Meteorology Conference*, D. Atlas, Ed., Amer. Meteor. Soc., 577-606.

12. Joss J, Lee R 1995. The application of radar-gauge comparisons to operational precipitation profile corrections. *J. Appl. Meteor.* **34**: 2612 – 2630.

40. Kirstetter, P.-E., 2008: Estimation quantitative des précipitations par radar météorologique: inférence de la structure verticale des pluies, modélisation des erreurs radar-pluviomètres (Radar quantitative precipitation estimation: inference of the vertical profile of reflectivity, radar-raingauge error model). PhD thesis of the Universities of Grenoble. To be defended.

41. Kirstetter, P.-E., G. Delrieu, B. Boudevillain, C. Obled, 2008 : Towards an error model for radar quantitative precipitation estimation in the Cévennes-Vivarais region, France. *Advances in Water Resources*, submitted.

42. Kitchen M, Brown R, Davies AG 1994. Real-time correction of weather radar data for the effects of bright band, range and orographic growth in widespread precipitation. *Q. J. R. Meteorol. Soc*., **120**, 1231-1254.

43. Krajewski WF, and Smith JA 2002. Radar hydrology: rainfall estimation. *Adv. Water Resour.*, 25, 1387-1394.

13. Krajewski, W., and Ciach, G., 2004. Towards Operational Probabilistic Quantitative Precipitation Estimation Using Weather Radar. Sixth International Symposium on Hydrological Applications of Weather Radar, Melbourne, 2-4 February.

14. Kuczera, G., and E. Parent (1998), Monte Carlo assessment of parameter uncertainty in conceptual catchment models: the Metropolis algorithm, *Journal of Hydrology*, *211*(1-4), 69-81.

44. Lebel, T., G. Bastin, C. Obled, J.-D. Creutin, 1987: On the accuracy of areal rainfall estimation – a case study. *Water Resources Research*, 23(11), 2133-2134.

45. Mantovan, P., and E. Todini (2006), Hydrological forecasting uncertainty assessment: Incoherence of the GLUE methodology, *Journal of Hydrology*, *130*(1-2), 368-381.

46. Marshall, J., and W. Palmer (1948), The distribution of raindrops with size, *J. Meteor.*, **4**, 186-192.

15. Marzoug, M., and P. Amayenc (1994), A class of single- and dual- frequency algorithms for rain-rate profiling from a spaceborne radar. Part I: principle and tests from numerical simulations, *J. Atmos. Oceanic Technol.*, **11**(6), 1480-1506.

47. Montanari, A. (2005), Large sample behaviors of the generalized likelihood uncertainty estimation (GLUE) in assessing the uncertainty of rainfall-runoff simulations, *Water Resources Research*, *41*(W08406), doi:10.1029/2004WR003826.

16. Morin E., Krajewski W. F., Goodrich D. C., Gao X., and Sorooshian S.: Estimating Rainfall Intensities from Weather Radar Data: The Scale Dependency Problem. *J. Hydrometeorol., 4(5),* 782-797, 2003.

48. Nicol J., G. Delrieu, P. Roquain, 2004: The use of pulse-to-pulse fluctuations for ground clutter elimination in conventional weather radar images for an urban environment. *Unpublished LTHE report*.

49. Pellarin T., G. Delrieu, G.M. Saulnier, H. Andrieu, B. Vignal, J.D. Creutin, 2002: Hydrologic visibility of weather radars operating in mountainous regions : case study for the Ardèche catchment (France). *J. Hydrometeor.,* **3**, 539-555

50. Rinehart, R.E., 1978: On the use of ground return targets for radar reflectivity factor calibration checks. *J. Appl. Meteor.*, **17**, 1342-1350.

51. Rivrain, J.C., 1998: Les épisodes orageux à précipitations extrêmes dans les régions méditerranéennes du sud de la France (Extreme storm-floods in the Mediterranean region of southern France). *Phénomènes remarquables*, n°4, Météo France, SCEM, 1998, 93 p.

52. Sanchez-Diezma, R., I. Zawadzki, and D. Sempere-Torres, 2000: Identification of the bright band through the analysis of volumetric radar data. *J. Geophys. Res.*, 105(D2), 2225-2236.

53. Sempere-Torres, D., J. Porrà, and J.-D. Creutin (1994), A general formulation for raindrop size distribution, *J. Appl. Meteor.*, **33**(12), 1494-1502.

54. Smith, J., and R. DeVeaux (1994), A stochastic model relating rainfall intensity to raindrop processes, *Water Resour. Res.*, **30**(3), 651-664.

55. Smith, J.A. and W.F. Krajewski, 1993: A modelling study of rainfall rate-reflectivity relationships. Water Resour. Res., 29, 2505-2514.

56. Smith JA, Seo DJ, Baeck ML, Hudlow MD 1996. An intercomparison study of NEXRAD precipitation estimates, *Water Resour. Res.*, **32**(7), 2035-2045.

57. Spear, R.C. and G.M. Hornberger, 1980: Eutrophication in Peel Inlet II, identification of critical uncertainties via Generalised Sensitivity Analysis. *Water Research*, 14, 43-49.

17. Steiner M, Houze RA, Yuter SE 1995. Climatological characterization of three-dimensional storm structure from operational radar and rain gauge data. *J. Appl. Meteor.,* **34,** 1978-2007.

58. Steiner, M., R. A., Houze, and S. E. Yuter, 1995: Characterization of three dimensional storm structure from operational radar and rain gauge data. *J. Appl. Meteor.*, **34**, 1978-2007.

59. Tabary, P., 2007: The new French operational radar rainfall product. Part 1: methodology. *Weather and Forecasting*, 22(3), 393-408.

60. Tabary, P., Desplats, J., Do Khac, K., Eideliman, F., Guégen, C., Heinrich, J.C., 2007: The new French operational radar rainfall product. Part 2: validation. *Weather and Forecasting*, 22(3), 409-427.

61. Testud, J., E. LeBouar, E. Obligis, and M. Ali-Mehenni (2000), The rain profiling algorithm applied to polarimetric weather radar, *J. Atmos. Oceanic Technol.*, **17**(3), 332-356.

18. Uijlenhoet R., S. H. van der Wielen, and A. Berne, 2006: Uncertainties in rainfall retrievals from ground-based weather radar: overview, case study, and simulation experiment. Hydrol. Earth Syst. Sci. Discuss., 3, 2385–2436, 2006.

62. Vanmarcke, E. (1983), *Random fields: analysis and synthesis*, 382 pp., MIT Press, Cambridge, Mass.

19. Vignal B., Andrieu H., and J.D. Creutin, 1999: Identification of vertical profiles of reflectivity from voluminal radar data. *J. Appl. Meteor.*, **38**(8), 1214-1228.

63. Vignal B., Galli G., Joss J., and U. Germann, 2000: Three methods to determine profiles of reflectivity from volumetric radar data to correct precipitation estimates. *J. Appl. Meteor.* **39**(10), 1715–1726.

64. Vignal, B., and W.F. Krajewski, 2000 : Large sample evaluation of two methods to correct range dependant error for WSR-88D rainfall estimates. *J. Hydrometeor*. **2,** 490-504.

20. Vrugt, J.A., Gupta, H.V., Bouten, W., Sorooshian, S., 2003. A Shuffled Complex Evolution Metropolis algorithm for optimization and uncertainty assessment of hydrologic parameter estimation. Water Resources Research 39 (8), 1201. doi:10.1029/ 2002WR001642.

65. Waldvogel, A. (1974), The N_0 jump of raindrop spectra, *J. Atmos. Sci.*, **31**(4), 1067-1078.

66. Westrick, K.J., C.F., Mass, and B.A., Colle, 1999: The limitations of the WSR-88D radar network for quantitative precipitation measurement over the coastal Western United States. *Bul. Amer. Meteor. Soc.*, Vol. 80, No. 11, pp. 2289–2298.

67. Wilson, J.W., and E.A. Brandes, 1979: Radar measurement of rainfall – a summary. *Bull. Amer. Meteor.Soc.*, 60, 1048-1058.

68. Yuter, S.E., R.A., Houze, 1997: Measurements of raindrop size distributions over the Pacific warm pool and implications for Z-R relations. *J. Appl. Meteor.*, **36**, 847-867.

69. Zawadzki I. 1984. Factors affecting the precision of radar measurements of rain. *Preprints, 22nd Conference on Radar Meteorology, Zurich, Switzerland*, Am. Meteorol. Soc., Boston, Mass. 251-256.